UiT
THE ARCTIC
UNIVERSITY
OF NORWAY

Faculty of Science and Technology

Department of Physics and Technology

An Investigation of Magnetic Field Disturbances on the Ground and in the Mesosphere

—

Nina Kristine Eriksen

FYS-3931 Master Thesis in Space Physics, June 2019

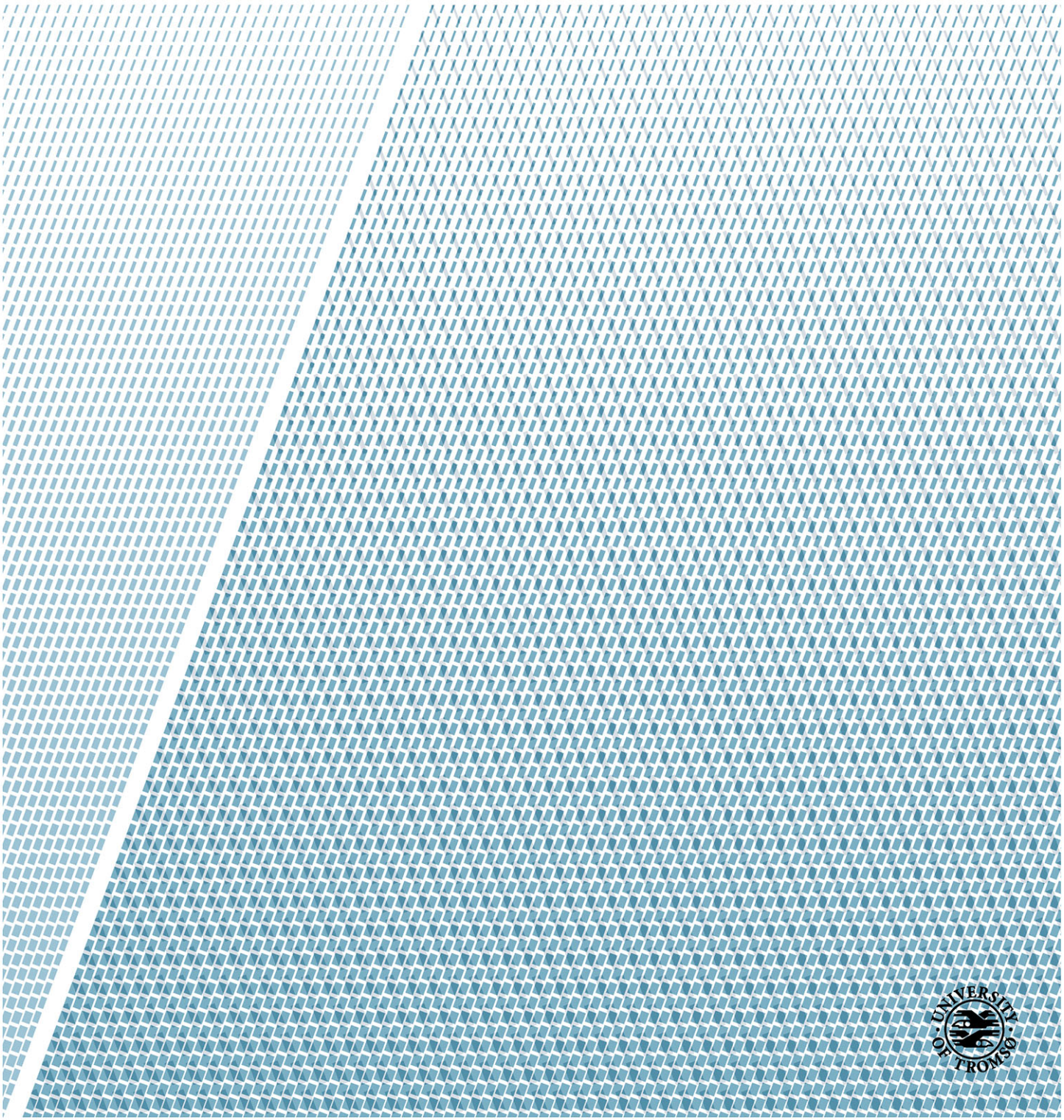

Abstract

Geomagnetic field models can be a useful tool for when and where there are no measurements available, or access is limited, because of a highly spatially uneven magnetometer network around the globe. The same can be said for altitudes above the ground, but below the ionospheric current layer, where there exist no in situ measurements at the point of writing. Modelled geomagnetic disturbances have been compared with ground magnetometer data to assess the model performance from two different models, the Spherical Elementary Currents System model and the Average Magnetic field and Polar current System model. Additionally a study on the change in geomagnetic disturbances with altitude were included as well. A third method called the Simple Line Current Approximation were added in this study. An assessment on the model performances by rocket magnetometer data studied in Burrows et al. (1971) were attempted to compensate for the lack of in situ measurements from the MOM-campaign, March 2019.

It was found that out of the two advanced models considered, the SECS model had the best performance, with a perfect fit to the measured ground magnetic field. The AMPS model performed poorly when modelling time series of geomagnetic field variations under the auroral zone. However, further model assessment in locations more favourable to magnetic disturbances driven by the solar wind is preferred before a final conclusion can be reached, due to the nature of the model. The assessment of model performance by historic rocket measurements was found to be an inadequate method, due to the large influence by the orientation of the ground geomagnetic field on the $\Delta B_{h,model}$ altitude profiles. This meant no conclusion on the accuracy on the model performance for altitudes above 0 km, but below 110 km, could be reached. At locations beneath the auroral zone the ionospheric current system appears too complex to be described by an equivalent current sheet system, or a simple line current, due to the presence of discrete currents in the E-layer. These findings emphasizes the need for a method of measuring the geomagnetic field in the mesosphere.

Acknowledgement

First and foremost, I would like to thank my supervisor Magnar G. Johnsen for all the help and support in the process of completing this thesis. I would like to give an extra thanks for allowing me all the opportunities to learn about the geomagnetic field through conversations, field trips and through TGO. Thanks to my co-supervisor Karl M. Laundal for teaching me about AMPS and the complexity of the model. A special thanks to Chris Hall for being on board with letting me work part time at TGO; it made my interest in the geomagnetic field grow. I would also like to thank Ulf-Peter Hoppe who first introduced me to the MOM-project in 2016, which made this whole thesis possible. It has been hard work, and often very confusing, but always fun!

Last, but not least, I want to thank my office mates Zoe, Torbjørn, Rikke, Henriette and Tinna. Without the moral and emotional support, and the endless fun conversations we have had, this year would have been a lot more stressful and difficult.

Contents

List of Figures

List of Tables

List of Abbreviations

AMPS	Average Magnetic field and Polar current System
FAC	Field Aligned Current
GMA	Geomagnetic Activity index
IGRF	International Geomagnetic Reference Field
IMAGE	International Monitor of Auroral Geomagnetic Effects
IMF	Interplanetary Magnetic Field
MAE	Mean Absolute Error
MLT	Magnetic Local Time
MOM	Mesospheric Optical Magnetometry in the Auroral Zone
QDV	Quiet Day Value
RMSE	Root Mean Square Error
SCHA	Spherical Cap Harmonics Analysis
SECS	Spherical Elementary Current System
SHA	Spherical Harmonics Analysis
SLCA	Simple Line Current Approximation
SVD	Single Value Decomposition
TGO	Tromsø Geophysical Observatory

Introduction and Background 1

1.1 Introduction

The book *De Magnete* (Gilbert, 1958) by the English physicists William Gilbert, first published in 1600s, has been said to represent the beginning of the modern science of geomagnetism. In the 1700s another English scientist named Halley and the British government performed an extensive mapping of the geomagnetic field at sea (Brekke, 2012). This was followed in the mid 1700s by the discovery of the relationship between the movement of the needle in a magnetic compass and auroral activity by Anders Celsius (Celsius, 1740) and Olav P. Hjorter (Hiorter, 1747). Another group that was important for the early development of geomagnetic research was the *Societas Meteorologica Palatina*, or the Mannheim Society. The group was formally established in 1780 in Germany as an effort to coordinate geophysical observations, among those aurora borealis, between different locations. Before this establishment there existed large uncertainties on whether the observations that was noted down were correct or not (Aspaas and Hansen, 2012).

Since then the study of Earth's magnetic field has become an area of research for various topics like: the changes in the geomagnetic field prior to an earthquake (Rikitake, 1968), the use of the geomagnetic field in wildlife migrations (Lohmann et al., 2007), geomagnetically induced currents effect on the power transmission grids and other technological systems (Pirjola, 2000) and, of course, topics in space physics like space weather prediction and ionospheric research. Earth's magnetic field is made up of three components: the internal field which is the main field due to Earth's liquid outer core, a crustal field which depends on the composition of the lithosphere/crust and an external field due to the ionospheric currents system, which changes dependent on its interaction with the magnetosphere (Cowley, 2000).

The ionospheric current system at high latitudes consists of three important currents: the Region 1 and Region 2 field aligned currents (FAC), Pedersen currents closing the FACs and the auroral eastward and westward electrojets. The auroral electrojets are Hall currents. The FACs, often referred to as Birkeland currents, are the result of downward and upward electron flow between the ionosphere and the magnetosphere. In a uniform conducting ionosphere the FACs couples to the Pedersen current which flows parallel to the electric field. The

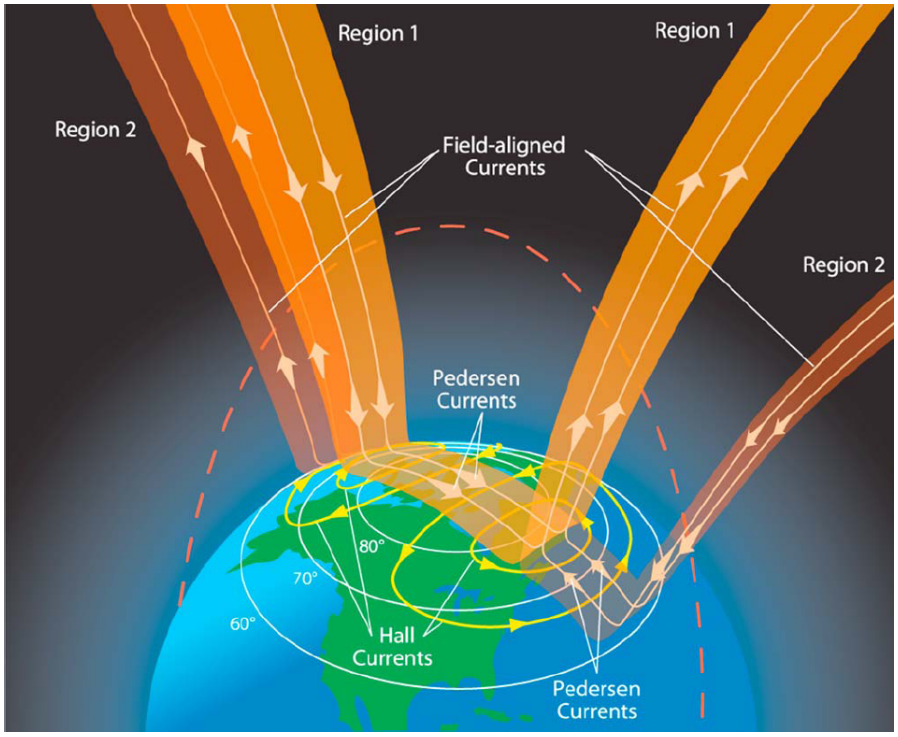

Fig. 1.1.: A schematic of combined FACs and ionospheric current systems. Figure is borrowed from Le et al. (2010).

Hall current, which is the result of a $E \times B$-drift that flows anti-parallel to the plasma convection in the ionosphere, closes completely by themselves (Le et al., 2010). Fig. 1.1 shows a schematic on how FACs flow into the ionosphere from the magnetosphere. Not depicted in Fig. 1.1 is the substorm current wedge, which is another important current giving rise to strong geomagnetic perturbations at high latitudes (Cowley, 2000). There exists other currents, of less importance to this thesis, in the ionosphere and magnetosphere that influences perturbations in the external geomagnetic field, among those are the magnetospheric ring current, magnetopause currents and cross-tail currents.

The Earth's magnetic field is measured in space by both rockets and satellites, and on the ground by an extensive network of around 177[1] magnetic observatories and several hundreds magnetometer stations around the globe. Even though this network provides us with a large amount of continuous measurements of the geomagnetic field there can still be limits in regards to spatial resolutions, and temporal resolutions of the measurements depending on the type of magnetometer used. Rockets are limited by their short time of flight and only fly through the area of interest once or twice. Satellites, which covers a large area, are limited by their short temporal resolution at each position. Satellites typically measure

[1] IAGA recognized observatories, `https://www.bgs.ac.uk/iaga/vobs/home.html` (Accessed: May 4, 2019)

at altitudes above 300 km making it difficult to directly use the measurements to decide on geomagnetic variations below the horizontal current layer in the lower ionosphere.

The network of ground magnetometer stations is big, but also highly uneven spatially with a high density of stations on land and often in more industrialized countries. This brings us over to the topic of this thesis which is the assessment and comparison of different geomagnetic field models that estimates external field variations. Geomagnetic field models are useful in general for estimating the field in an area where there might be a lack of measurements, or the access to the measurements is limited. For the internal geomagnetic field one of the most common models are the International Geomagnetic Reference Field model (Thébault et al., 2015) which provides reasonable results for most locations. The crustal field does not change much due to its origin and can be determined by a magnetic survey for an area, like the ones done for Svalbard (Lytskjold, 1991) and Scandinavia including Finland (Eleman, 1969). Combining models of the internal and crustal fields provides an accurate description of the geomagnetic field, except during magnetic disturbances from the external field.

The external field is a bit trickier to model due its dependency on solar-terrestrial interactions which changes frequently. Additionally there exists phenomena like substorms, geomagnetic storms and impulses that are difficult to predict with high certainty at this point. This thesis investigates the accuracy of the Average Magnetic field and Polar current System (AMPS) model (Laundal et al., 2018) and the Spherical Elementary Current System (SECS) model (Amm and Viljanen, 1999) by comparing the model outputs to magnetometer data taken by the variometer at Andenes, Norway located at geographical latitude 69.30 $^\circ$ N and longitude 16.04° E. Ten days have been chosen for the comparison, where some of the days were considered quiet days, i.e. there were not a lot of large geomagnetic perturbations caused by ionospheric currents, and some more disturbed days to include a broader range of magnetic disturbances.

An analysis on the altitude dependency of the magnetic variations estimated by the models will also be performed. For this analysis the magnetic variations will be modelled between the ground and the mesosphere at an altitude of 90 km. During this step we will look at the total field variations instead of the variations in the different spatial directions. The reason for this is to be able to compare the model outputs with the future results of Mesospheric Optical Magnetometery in the Auroral Zone, which is discussed in Section 1.3.

The model comparison will also include a simple line current approximation (SLCA) to find the magnetic field variations at 90 km due to an infinite long line current. With this approximation we wish to assess whether the SLCA can be used

as a simple tool for geomagnetic field variations estimated below the ionosphere, or if there is need for a more advance model, like the ones mentioned above.

1.2 The Different Models

This section gives a short introduction to the geomagnetic field variation models that will be considered in this thesis.

Average Magnetic Field and Polar Current System

The Average Magnetic field and Polar current System (AMPS) model is an empirical model which decomposes the perturbed magnetic field into a poloidal field, due to horizontal currents, and a toroidal field due to magnetic field aligned currents (Laundal et al., 2016). The toroidal and poloidal magnetic potential are both given as spherical harmonics expansions, where the relevant coefficients are derived from magnetic field data from the CHAMP satellite (Reigber et al., 2002) and the Swarm constellation (Friis-Christensen et al., 2006) and limited according to solar wind parameters. Since the AMPS model uses a large selection of data to estimate parameters for the mathematical structure it is understood that phenomena like substorms, geomagnetic storms and impulses might be averaged out, and the resulting perturbed field might not include these disturbances. However, by looking at the goodness of fit of the modelled output a conclusion on the model performance can be attempted.

Spherical Elementary Current System

The Spherical Elementary Current System (SECS) model (Amm, 1997 and Amm and Viljanen, 1999) is the second model that will be analyzed. It is based on an elementary current system consisting of a divergence free elementary current, curl free elementary current and field aligned currents. The general principle of the model is that elementary current base vectors can be placed on a grid covering part of a sphere. A divergence free current density is given by $\mathbf{J_{df,el}}(\vec{r}') = \frac{I_{0,df}}{4\pi R_I}\cot(\theta'/2)\hat{\phi}'$, where $I_{0,df}$ is a scaling factor. There is also an equivalent current density, with a respective scaling factor for a curl free current density. These two densities functions make up an elementary current set. However, for studies below the ionosphere only the divergence free current density is relevant (Fukushima, 1971). The scaling factors are found with the use of a n_{obs} number of magnetometer data inputs from a set number of stations to produce a n_{el} number of elementary currents.

Simple Line Current Approximation

The last method that will be applied in this thesis is the Simple Line Current Approximation (SLCA). The SLCA is based on a geometric problem for an infinite

long current located at 110 km altitude, which induces a surrounding magnetic field. The current location and direction is based on ground based magnetic field measurements from one station. The field at 90 km directly above the magnetometer can then be estimated by solving the geometric problem, as well as using the magnetic field-current relation for the infinite long line current $B = \frac{2\pi i}{\mu_0 r}$, where r is the radius away from the current to a magnetic field line of interest. This method will be compared to the more advanced models like AMPS and SECS.

1.3 Mesospheric Optical Magnetometry

The validation of any of the model outputs might be possible if the Mesospheric Optical Magnetometry (MOM) in the Auroral Zone-project[2] get good results. The project's goal is to measure the geomagnetic field at an altitude of 80-90 km by the use of a sodium-LIDAR located at Andenes (Serrano, 2017). The FASOR[3]-laser source causes spontaneous emission from the natural occurring sodium layer in the mesosphere, and the backscatter from this emission can be measured at ground. The total geomagnetic field can be derived from the backscatter frequency using $2\pi f_L = \gamma B$, where γ is a gyromagnetic constant (Kane et al., 2018). f_L is the Larmor-frequency, which is the frequency that would allow for the most backscatter. The sodium-LIDAR is thus essentially an optical sodium precession magnetometer (Hrvoic and Newitt, 2011). The MOM-project will not be discussed thoroughly in this paper as the sodium-LIDAR is still not operational at the point of writing. If the sodium-LIDAR succeed in measuring the magnetic field over Andenes during the fall/winter of 2019/2020, it will be possible to compare the three methods discussed in this paper with actual in situ measurements, as a subject for future work.

Measuring the geomagnetic field for these altitudes using a sodium-LIDAR has already been accomplished by Kane et al. (2018) and Bustos et al. (2018) previously. Thus providing the method for the MOM-project. However, Kane et al. (2018) and Bustos et al. (2018) measurements are not useful for the comparison of magnetic field variations under the auroral oval, therefore the MOM-project aims to make such measurements. The experiments in Kane et al. (2018) and Bustos et al. (2018) were made at middle latitudes, 32.42 °N and 28.76°N respectively. The lack of strong external magnetic field variations at these latitudes might be the reason for the weak results in terms of measurements of the geomagnetic field variations, even if the the optimal angle between the geomagnetic field and the LIDAR beam is 90°, and these latitudes are thus favourable.

[2] `https://site.uit.no/mom/` (accessed: May 29, 2019)
[3] Frequency Addition Source of coherent Optical Radiation

1.4 Rocket Borne Magnetometry

As the mesospheric magnetic field is fairly unexplored in terms of measurements it was of interest to check what has previously been measured by rockets. Apparently, from what has been discovered during the work on this thesis the first rocket that measured the geomagnetic field was launched in 1948 at White Sands, New Mexico at 32.40°N and 106.38°W. The rocket was launched to test the feasibility of measuring the Earth's magnetic field using an airborne magnetometer (Maple et al., 1950). The first rockets to measure the magnetic field for the purpose of research was launched in 1949 from the seaplane tender USS *Norton Sound* outside of the coast of Peru. These were the rockets Aerobee A-10 and A-11 launched at 10.80°S and 89.23°W on March 17 and at 11.10°S and 88.44°W on March 22 1949, respectively (Singer et al., 1951). The main purpose of the former was to obtain cosmic-ray data but it also measured the magnetic field, however, the latter rocket's main objective was to obtain magnetic field measurements. With the data from the Aerobee A-10 and A-11 Singer et al. (1951) experimentally established the existence of a current system responsible for diurnal variation of the geomagnetic field in the E-region of the ionosphere. In the following 20 years several magnetic field measurements were carried out by rockets, some of which are described in Burrows and Hall (1965), Potter (1970) and, Burrows and Sastry (1976). An attempted, complete, list of literature studying the rocket measurements of the geomagnetic field that was discovered during the work on this thesis can be found in Appendix C. Note, if several papers discuss the same set of rocket measurements only one has been included in the list, since it is the rocket measurements themselves that is of interest to this thesis.

One particular paper that is of interest for this thesis is Burrows et al. (1971). The paper discussed the results from the airborne magnetometers on two Nike-Tomahawk rockets launched in 1966 from Fort Churchill, Canada (58.73°N, -93.82°W) along with ground magnetometer data. They concluded that their measurements supported the theory that the auroral electrojets currents mainly consists of Hall currents. Figure 5 and Figure 3 in Burrows et al. (1971) will be used further on in our analysis. Figure 5 will be compared with the estimated altitude variations of the magnetic field for a certain point in time from one of our days. The day will be chosen to have fairly similar magnetic variations as to that of the magnetogram in Figure 3 in the paper. By comparing the magnetic field measurements in Figure 5 with the selected point in time, getting an insight on how accurate the model performances is for the magnetic field variation altitude profile might be achieved.

1.5 Thesis Layout

In **Chapter 2** the underlying theories for the different models and how they are built up are described. **Chapter 3** explain the methodology for how the different models have been used so that they can be compared to one another, including the height variation comparisons of the total field perturbations. This will be done for both the 24 hours period for each day, and additionally for a point in time for one day that will be compared with the results of Burrows et al. (1971). In **Chapter 4** the results of a selected number of days will be presented, and the rest of the remaining results can be found in **Appendix A**. A discussion about the results presented in the previous chapter will be given in **Chapter 5**. **Chapter 6** concludes this thesis and also discuss future work on this topic.

Theory

2

The theoretical framework of the models are presented in this chapter. The Average Magnetic field and Polar current System model and the Spherical Elementary Current System model are considered advanced models, and the Simple Line Current Approximation is included as a simple method to estimate magnetic field disturbances above ground.

2.1 Average Magnetic Field and Polar Current System

Model Structure

The Average Magnetic field and Polar current System (AMPS) is an empirical model that uses solar-terrestrial parameters as input values to model the ionospheric magnetic field. Spherical harmonics coefficients are derived from vector magnetic field data by low Earth orbit magnetic field measurements (Laundal et al., 2018). The satellite data is collected from the Swarm constellation (Friis-Christensen et al., 2006), from September 2013 to September 2015, and the CHAMP satellite (Reigber et al., 2002), from August 2000 to September 2010.

AMPS uses a geodetic Earth model with semi-major axis radius of $R_{major} = 6902\,\text{km}$ and semi-minor axis radius of $R_{minor} = 6615\,\text{km}$. The model is based on an approach where we only consider the geomagnetic field perturbations from the external field. The perturbations can be considered to consists of two parts, due to Gauß's Law of magnetism $\nabla \cdot B = 0$, one toroidal part $\Delta B_{tor} = \mathbf{r} \times \nabla T$ and one poloidal part $\Delta B_{pol} = -\nabla V$. This gives the total perturbation field $\Delta B = \Delta B_{pol} + \Delta B_{tor} = -\nabla V + \mathbf{r} \times \nabla T$. The field aligned current (FAC) density, $\mathbf{J}_{\parallel}$, does not vanish with increasing altitude and you cannot derive the total geomagnetic field, $B = B_{main} + B_{crust} + B_{external}$, from a single Laplacian potential. This is opposed to the Earth's main field which may be derived using a function of spherical harmonics expansion, like that of the IGRF-model described in Thébault et al. (2015). The above approach therefore takes into account the contribution from the FACs which couples to horizontal currents in the ionosphere at one end and in the magnetosphere to plasma sheet currents, magnetopause currents or ring currents at the other end.

The satellite samples of the perturbed field is collected in a low Earth orbit, around 400-500 km. The orbit of the CHAMP satellite started at $\approx 450\,\text{km}$, but

as it fell down it burned up at around 130 km in September 2010. The SWARM constellation orbits at around $400 - 500\,\text{km}$. This means that the orbit-shell where the data was collected is still very thin compared to the the radius of the hollow sphere enclosed by this shell, which is why ΔB_{pol} can be approximated as a Laplacian field $\Delta B_{pol} = -\nabla V$. The current associated with this field are mainly horizontal currents with a maximum in the E-layer and weaker horizontal currents above this height. They are therefore inside the region where the satellite data is collected (Laundal et al., 2016). This means we can write the poloidal scalar potential as:

$$V(\theta_{qd}, \phi, h_{ref}) = \sum_{n,m} \left(\frac{R_E}{R_E + h_{ref}} \right)^{n+1} P_n^m(\theta_{qd}) \left[g_n^m \cos(m\phi) + h_n^m \sin(m\phi) \right] \quad (2.1)$$

where θ_{qd} is the quasi-dipole colatitude (Richmond, 1995) and h_{ref} is the reference height above a geoidal Earth. P_n^m is the Schmidt semi-normalized Legendre functions of degree m and order n and g_n^m, h_n^m are coefficients estimated from the magnetic measurements.

From Laundal et al. (2018) and references therein, we have that the spherical harmonics coefficients g_n^m are expanded as:

$$\begin{aligned} g_n^m =& g_{n,1}^m + g_{n,2}^m \sin(\theta_c) + g_{n,3}^m \cos(\theta_c) + g_{n,4}^m \epsilon + g_{n,5}^m \epsilon \sin(\theta_c) + g_{n,6}^m \epsilon \cos(\theta_c) + \\ & g_{n,7}^m \beta + g_{n,8}^m \beta \sin(\theta_c) + g_{n,9}^m \beta \cos(\theta_c) + g_{n,10}^m \beta\epsilon + g_{n,11}^m \beta\epsilon \sin(\theta_c) + \\ & g_{n,12}^m \beta\epsilon \cos(\theta_c) + g_{n,13}^m \tau + g_{n,14}^m \tau \sin(\theta_c) + g_{n,15}^m \tau \cos(\theta_c) + g_{n,16}^m \beta\tau + \\ & g_{n,17}^m \beta\tau \sin(\theta_c) + g_{n,18}^m \beta\tau \cos(\theta_c) + g_{n,19}^m F_{10.7} \end{aligned} \quad (2.2)$$

where $\theta_c = \arctan 2(B_y, B_z)$ is the Interplanetary Magnetic Field (IMF) clock angle, calculated from the IMF B_y and B_z components. The clock angle gives an indication of possible sub-solar reconnection between the IMF and geomagnetic field. $\epsilon = 10^{-3} |v_{sw}|^{4/3} \sqrt{B_y^2 + B_z^2}^{2/3} \sin^{8/3}(\theta_c/2)$ is a coupling function between the solar wind and the magnetosphere (Newell et al., 2007). It gives an estimate of the electromagnetic energy transported into the magnetosphere from the solar wind. β is the tilt of the Earth's dipole magnetic field with respect to the sun, and v_{sw} is the solar wind velocity in GSE(GSM) x-direction. $F_{10.7}$ is the 10.7 cm solar radio flux index, and lastly $\tau = 10^{-3} |v_{sw}|^{4/3} \sqrt{B_y^2 + B_z^2}^{2/3} \cos^{8/3}(\theta_c/2)$ is defined as a new variable in Laundal et al. (2018) to describe energy input from a lobe region reconnection, which happens when the IMF is northward as opposed to sub-solar reconnection for a southward IMF. h_n^m, and as will be used further down ψ_n^m and η_n^m, are expanded in the same fashion as g_n^m.

Organizing the data in a magnetic apex coordinate system (Richmond, 1995), with a magnetic latitude λ_m and longitude ϕ, the toroidal field $\Delta B_{tor} = \mathbf{r} \times \nabla T$ can be represented as a scalar potential, T. The potential can be written as a spherical harmonics expansion (Laundal et al., 2016):

$$T(\theta_m, \phi) = \sum_{n,m} P_n^m(\theta_m) \left[\psi_n^m \cos(m\phi) + \eta_n^m \sin(m\phi)\right] \tag{2.3}$$

where θ_m is the magnetic colatitude. The toroidal potential is associated with primarily Birkeland currents, i.e. magnetic field aligned currents. The magnetic apex coordinate system is discussed in detail in Richmond (1995).

Coordinate System of AMPS and the Transformation into Geographical ENU Coordinates

The AMPS model substitute the magnetic longitude with magnetic local time (MLT), ϕ_{MLT} due to the fact that the currents in the system is highly dependent on the position of the sun. With the use of ϕ_{MLT}, Eq. (2.1) and Eq. (2.3) the model calculates the perturbation for a height h in a local magnetic quasi-dipole coordinate system defined by an eastward component ΔB_e, a northward component ΔB_n and an upward component ΔB_u, given by:

$$\Delta B_e = \frac{-d_{1,n}}{\cos(\lambda_m)} \frac{\delta T(\lambda_m)}{\delta \phi_{MLT}} + \frac{d_{2,n}}{\sin(I_m)} \frac{\delta T}{\delta \lambda_m} - \frac{f_{2,n}}{R_E + h} \frac{1}{\cos(\lambda_{qd})} \frac{\delta V}{\delta \phi_{MLT}} + \frac{f_{1,n}}{R_E + h} \frac{\delta V}{\delta \lambda_{qd}} \tag{2.4}$$

$$\Delta B_n = \frac{d_{1,e}}{\cos(\lambda_{qd})} \frac{\delta T}{\delta \phi_{MLT}} - \frac{d_{2,e}}{\sin(I_m)} \frac{\delta T}{\delta \lambda_m} + \frac{f_{2,e}}{R_E + h} \frac{1}{\cos(\lambda_{qd})} \frac{\delta V}{\delta \phi_{MLT}} - \frac{f_{1,e}}{R_E + h} \frac{\delta V}{\delta \lambda_{qd}} \tag{2.5}$$

$$\Delta B_u = -\sqrt{F} \frac{\delta V}{\delta h} \tag{2.6}$$

$f_{1,e/n}$ and $f_{2,e/n}$ are horizontal base vectors in the quasi-dipole coordinate system containing an eastward and a magnetic poleward component each. See Figure 2 in Laundal and Gjerloev (2014) for a graphical representation of $\mathbf{f_1}$ and $\mathbf{f_2}$. $d_{1,e/n}$ and $d_{2,e/n}$ are apex base vectors above ground, which decrease with altitude and are normal to contour lines of apex longitude ϕ_A and latitude λ_A, respectively. $\mathbf{d_1}$ and $\mathbf{d_2}$ are potential dependent, and can be found by the method described in Richmond (1995).

F is given by:

$$F = \mathbf{f_1} \times \mathbf{f_2} \cdot \hat{\mathbf{k}} = f_{1,e} f_{2,n} - f_{1,n} f_{2,e} \tag{2.7}$$

and is the upward component of $\mathbf{f_1} \times \mathbf{f_2}$. The upward unit vector $\hat{\mathbf{k}}$ is described by Eq. (3.7) in section 3, along with the two horizontal unit vectors. The magnetic apex inclination is given by:

$$\sin(I_m) = \frac{2\sin(\lambda_m)}{\sqrt{4 - 3\cos^2(\lambda_m)}} \tag{2.8}$$

Since the output is given in quasi-dipole coordinates, it has to be converted into local magnetic geocentric coordinates $\Delta E_{AMPS}, \Delta N_{AMPS}$ and ΔU_{AMPS}. This is done using Eq. (8.8) for the horizontal components in Richmond (1995), which is given by:

$$\Delta E_{AMPS} = \hat{\mathbf{e}} \cdot \mathbf{f_2} \times \hat{\mathbf{k}} \Delta B_e + \hat{\mathbf{e}} \cdot \hat{\mathbf{k}} \times \mathbf{f_1} \Delta B_n \tag{2.9}$$

$$\Delta N_{AMPS} = \hat{\mathbf{n}} \cdot \mathbf{f_2} \times \hat{\mathbf{k}} \Delta B_e + \hat{\mathbf{n}} \cdot \hat{\mathbf{k}} \times \mathbf{f_1} \Delta B_n \tag{2.10}$$

where $\hat{\mathbf{e}}, \hat{\mathbf{n}}$ are unit vectors, described Eq. (3.7), pointing in the geographical east and north direction respectively.

The vertical component is converted from quasi-dipole to ENU geocentric coordinates using Eq. (8.9) in Richmond (1995):

$$\Delta U_{AMPS} = \sqrt{F} \Delta B_u \tag{2.11}$$

Ground and Mesospheric Magnetic Field Perturbations

Since this paper investigate magnetic field perturbation under 110 km altitude, i.e. in the mesosphere and below, the geomagnetic field for these altitudes are calculated using the approach described in Laundal and Reistad (2018). The current densities at h_{ref} are calculated from

$$\nabla \times \Delta B / \mu_0 = \mathbf{J} = \mathbf{J_{df}} + \mathbf{J_{cf}} \tag{2.12}$$

where μ_0 is the permeability of free space, and $\mathbf{J_{df}}$ and $\mathbf{J_{cf}}$ are the divergence free and curl free current densities respectively.

Since we are interested in ground perturbations at high latitudes and below the ionospheric currents, we assume Fukushima's theorem hold (Fukushima, 1971). It tells us that we can only measure perturbations induced by the divergence free current at ground level, since the curl free current couples with the field aligned currents in the ionosphere. The curl free current and its calculations will not be discussed further in this section, but can be looked up in Laundal and Reistad (2018) for further interest.

The divergence free current density at h_{ref} is given by:

$$\mathbf{J_{df}} = \hat{\mathbf{k}} \times \nabla\Psi \tag{2.13}$$

Ψ is a current function that can be derived, since the current densities can be considered contained to a surface (Haines and Torta, 1994). At h_{ref} it is given by:

$$\begin{aligned}\mathbf{\Psi}(\theta,\phi) = -\frac{R_E}{\mu_0}\sum_{n,m}\frac{2n+1}{n}\left(\frac{R_E}{R_E+h_{ref}}\right)^{n+1} P_n^m(\theta) \\ \cdot\left[g_n^m\cos(m\phi) + h_n^m\sin(m\phi)\right]\end{aligned} \tag{2.14}$$

All variables are the same as described in Eq. (2.1), and the subscript for the quasi-dipole coordinate system and ϕ_{mlt} has been omitted for simplicity. The magnetic field perturbations for $R_E < r < h_{ref}$ is given as $\Delta B = -\nabla V_{ground}$ and the potential can be described as:

$$\begin{aligned}V_{ground} = R_E\sum_{n,m}P_n^m(\theta)\Bigg[\left(a_{n,e}^m\left(\frac{r}{R_E}\right)^n + a_{n,i}^m\left(\frac{R_E}{r}\right)^{n+1}\right)\cos(m\phi) \\ + \left(b_{n,e}^m\left(\frac{r}{R_E}\right)^n + b_{n,i}^m\left(\frac{R_E}{r}\right)^{n+1}\right)\sin(m\phi)\Bigg]\end{aligned} \tag{2.15}$$

where the subscript e, i is for external and internal magnetic field contribution, respectively. In AMPS the internal magnetic field contribution is assumed zero, thus Eq. (2.15) becomes:

$$V_{ground} = R_E\sum_{n,m}\left(\frac{r}{R_E}\right)^n P_n^m(\theta)\left[a_{n,e}^m\cos(m\phi) + b_{n,e}^m\sin(m\phi)\right] \tag{2.16}$$

For each component in the eastward, northward and upward direction, $-\nabla V_{ground}$ is given by:

$$\Delta B_e = \frac{1}{r\cos(\lambda)}\frac{\delta V_{ground}}{\delta\phi}, \quad \Delta B_n = -\frac{1}{r}\frac{\delta V_{ground}}{\delta\theta}, \quad \Delta B_u = \frac{\delta V_{ground}}{\delta r} \tag{2.17}$$

Here $\sin\theta = \cos\lambda$ is used. Solving the above equation gives:

$$\Delta B_e = \frac{R_E}{r\cos\lambda}\sum_{n,m}\left(\frac{r}{R_E}\right)^n P_n^m(\theta)m\left[a_{n,e}^m\sin(m\phi) - b_{n,e}^m\cos(m\phi)\right] \tag{2.18}$$

$$\Delta B_n = -\frac{R_E}{r}\sum_{n,m}\left(\frac{r}{R_E}\right)^n \frac{dP_n^m(\theta)}{d\theta}\left[a_{n,e}^m\cos(m\phi) + b_{n,e}^m\sin(m\phi)\right] \tag{2.19}$$

$$\Delta B_u = \frac{R_E}{r}\sum_{n,m}n\left(\frac{r}{R_E}\right)^n P_n^m(\theta)\left[a_{n,e}^m\cos(m\phi) + b_{n,e}^m\sin(m\phi)\right] \tag{2.20}$$

In Laundal and Reistad (2018) assumptions are made that the equivalent current function, i.e. the scalar field $\mathbf{\Psi}$, is going to be the same whether it is evaluated in the ionosphere $r = R_E + h_{ref}$ or at ground $r = R_E$. For $r = R_E + h_{ref}$ the divergence free current $\mathbf{J}'_{\mathbf{df}} = \hat{\mathbf{r}} \times \nabla \mathbf{\Psi}'$, and the current function is given as:

$$\mathbf{\Psi}'(\theta, \phi) = -\frac{R_E}{\mu_0} \sum_{n,m} \frac{2n+1}{n+1} \left(\frac{R_E + h_{ref}}{R_E} \right)^n P_n^m(\theta)[a_{n,e}^m \cos(m\phi) + b_{n,e}^m \sin(m\phi)] \tag{2.21}$$

Eq. (2.14) can be used to find the relationship between the coefficients in space, g_n^m, h_n^m, with the ones on ground $a_{n,e}^m$ and $b_{n,e}^m$. This is done by setting :

$$\mathbf{\Psi}' = \mathbf{\Psi}$$

which gives the relations:

$$a_{n,e}^m = \frac{n+1}{n} \left(\frac{R_E}{R_E + h} \right)^{2n+1} g_n^m \tag{2.22}$$

$$b_{n,e}^m = \frac{n+1}{n} \left(\frac{R_E}{R_E + h} \right)^{2n+1} h_n^m \tag{2.23}$$

By using Eq. (2.18), Eq. (2.19), Eq. (2.20) and the above coefficient relations the magnetic ground perturbations at $r = R_E$ are given as:

$$\Delta B_e = -\frac{1}{\cos \lambda_m} \sum_{n,m} \left(\frac{R_E}{R_E + h_{ref}} \right)^{2n+1} \frac{n+1}{n} P_n^m(\theta) m \cdot [g_n^m \sin(m\phi) - h_n^m \cos(m\phi)] \tag{2.24}$$

$$\Delta B_n = -\sum_{n,m} \left(\frac{R_E}{R_E + h_{ref}} \right)^{2n+1} \frac{n+1}{n} \frac{dP_n^m(\theta)}{d\theta} \cdot [g_n^m \cos(m\phi) + h_n^m \sin(m\phi)] \tag{2.25}$$

$$\Delta B_u = \sum_{n,m} \left(\frac{R_E}{R_E + h_{ref}} \right)^{2n+1} (n+1) P_n^m(\theta)[g_n^m \cos(m\phi) + h_n^m \sin(m\phi)] \tag{2.26}$$

Since Eq. (2.24), Eq. (2.25) and Eq. (2.26) are evaluated at ground they need to be adjusted when looking at heights below $r = R_E + h_{ref}$. Multiplying the horizontal components ΔB_e and ΔB_n with $r^n R_E^{-n}$ and the upward component ΔB_u by $r^{n-1} R_E^{n-1}$ ensures that r remains a free parameter. These multiplications allows the magnetic field perturbations to be found below the ionosphere, which in the AMPS model is set at a default height of 110 km. If this value is increased the corresponding ground perturbations will decrease.

2.2 Simple Line Current Approximation

For the Simple Line Current Approximation (SLCA) we consider an infinite long line current at an altitude of 110 km, see Fig. 2.1. To get an estimate of the perturbed magnetic field at 90 km we the geometric configuration is solved. The

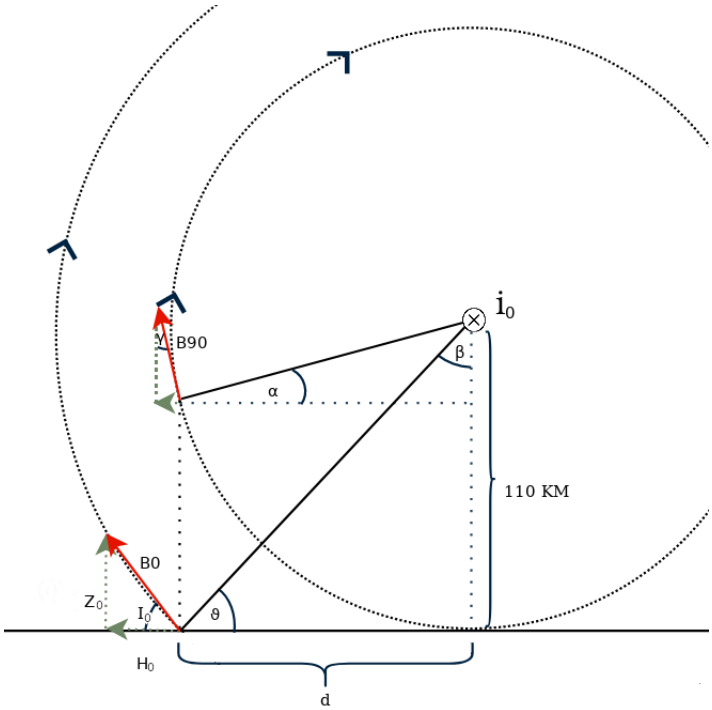

Fig. 2.1.: Simple line current approximation for the magnetic field due to a line current located at 110 km above ground.

coordinate system is defined in the same fashion as the geographic local X, Y and Z coordinate system used in magnetometry. Z is positive downwards, X positive to the geographic north, and Y positive towards east.

Using geometry, $\sum$ angles in a triangle $= 180°$ and Pythagoras the following set of equations are relevant for the major triangle:

$$\theta = 90° - I_0 \tag{2.27}$$

$$d = \frac{110\,\text{km}}{\tan\theta} \tag{2.28}$$

$$r_0 = \sqrt{d^2 + (110\,\text{km})^2} \tag{2.29}$$

and for the minor:

$$\alpha = \arctan\frac{20\,\text{km}}{d} \tag{2.30}$$

$$r_{90} = \sqrt{d^2 + (20\,\text{km})^2} \tag{2.31}$$

The total magnetic field perturbation on the ground is found using:

$$H_0 = \sqrt{\Delta X^2 + \Delta Y^2} \tag{2.32}$$

$$D_0 = \arctan \frac{\Delta Y}{\Delta X} \tag{2.33}$$

$$I_0 = \arctan \frac{\Delta Z}{H_0} \tag{2.34}$$

and thus:

$$B_0 = \frac{\Delta Z}{\sin I_0} \tag{2.35}$$

where ΔX, ΔY and ΔZ is the perturbed magnetic field components. The total magnetic field perturbation at 90 km is then given as:

$$B_0 = \frac{\mu_0 i_0}{2\pi r_0}$$

$$\Rightarrow i_0 = \frac{2\pi r_0 B_0}{\mu_0}$$

giving

$$B_{90} = \frac{\mu_0 i_0}{2\pi r_{90}} = \frac{\mu_0}{2\pi r_{90}} \frac{2\pi r_0 B_0}{\mu_0}$$

$$B_{90} = \frac{r_0}{r_{90}} B_0 \tag{2.36}$$

We find the angle ΔI_{90} using $\sum$ angles in a triangle $= 180°$, and are therefore able to find the components related to the triangle given by $\mathbf{B_{90}}$, $\mathbf{\Delta Z_{90}}$ and $\mathbf{\Delta H_{90}}$. We end up with the following set of equations describing the magnetic field components at 90 km:

$$\Delta I_{90} = 90° - \alpha \tag{2.37}$$

$$\Delta H_{90} = B_{90} \cos I_{90} \tag{2.38}$$

$$\Delta X_{90} = H_{90} \cos D_{90} \tag{2.39}$$

$$\Delta Y_{90} = H_{90} \sin D_{90} \tag{2.40}$$

$$\Delta Z_{90} = B_{90} \sin I_{90} \tag{2.41}$$

where

$$\Delta D_{90} = \arctan \frac{\Delta Y}{\Delta X}$$

here it is assumed that $\Delta D_{90} = D_0$. Where D_0 is the angle between the perturbed horizontal field $H_0 = \sqrt{\Delta X^2 + \Delta Y^2}$ and its X-component.

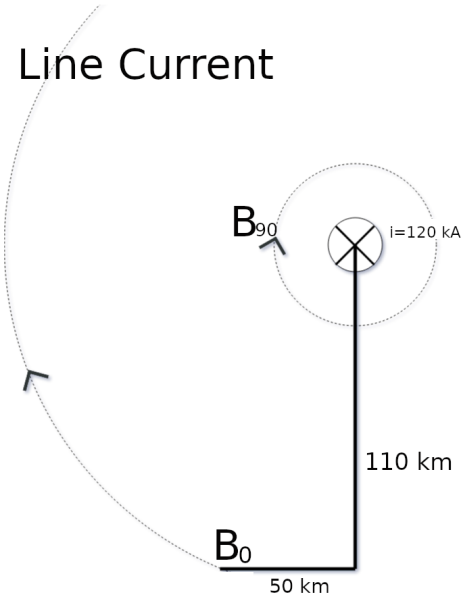

Fig. 2.2.: Magnetic field from a 120 kA line current.

Fig. 2.2 illustrates an example of measuring the magnetic field 50 km away from an infinite large line current located at an altitude of 110 km with $i_0 = 120\,\text{kA}$. The line current gives the magnetic field at 0 km and 90 km to be:

$$B_0 = \frac{\mu_0}{2\pi} \frac{120\,\text{kA}}{\sqrt{(50\,\text{km})^2 + (110\,\text{km})^2}} = 200\,\text{nT}$$

$$B_{90} = \frac{\mu_0}{2\pi} \frac{120\,\text{kA}}{\sqrt{(20\,\text{km})^2 + (110\,\text{km})^2}} = 446\,\text{nT}$$

2.3 Spherical Elementary Current System

Elementary Currents and the Magnetic Field

The Spherical Elementary Current System (SECS) model described in Amm (1997) and Amm and Viljanen (1999) uses basis functions to describe an ionospheric current system. The current system consist of a curl free and a divergence free basis function, which are called elementary current systems. This equivalent current system, with the addition of a FAC coupling with the curl free function, can be expanded into any ionospheric current system without making assumptions on the ionospheric conductivities and electric fields. Fig. 2.3 shows the system on a sphere, where the curl free system couples to FACs that are assumed to flow radially.

The elementary current system produces two sets of magnetic fields. One magnetic field is poloidal and only present in the area above the elementary

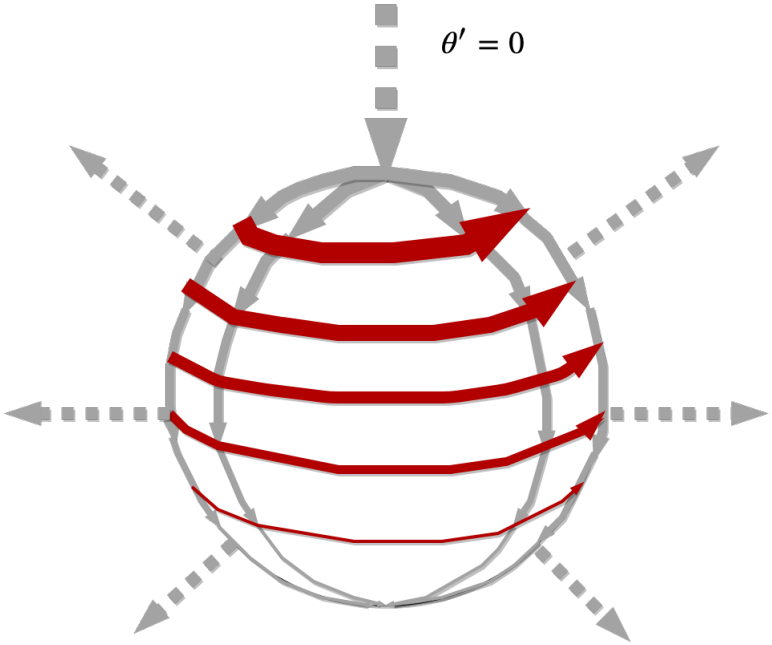

Fig. 2.3.: Spherical Elementary Current System adapted from Fig. 1 in Amm and Viljanen (1999). The grey current system is the curl free elementary system, including the FACs that they couple with in the ionosphere. The red current system is the divergence free current system.

current systems, i.e. in and above the ionosphere. This field is induced by the curl free currents and FACs system. The other magnetic field is toroidal and induced by the divergence free basis function.

For a sphere with a source current given by the position vector $\vec{r}'$ the divergence free and curl free basis functions are given by:

$$\mathbf{J}_{\mathbf{df,el}}(\vec{r}') = \frac{I_{0,df}}{4\pi R_I} \cot(\theta'/2)\hat{\phi}' \tag{2.42}$$

and

$$\mathbf{J}_{\mathbf{cf,el}}(\vec{r}') = \frac{I_{0,cf}}{4\pi R_I} \cot(\theta'/2)\hat{\theta}' \tag{2.43}$$

where $\hat{\phi}'$ and $\hat{\theta}'$, with the addition of $\hat{\mathbf{r}}'$, are unit vectors for the spherical coordinate system. The superscript $'$ are there to distinguish the spherical coordinate system from a geographical spherical system of the relevant equivalent current system. The "poles" in the system is where θ' is equal to zero, and for this area a FAC with magnitude $I_{0,cf}$ flows radially into the magnetosphere. The ionosphere is assumed to be an infinitely thin layer above the Earth's surface located at a height $R_I = 110\,\text{km}$.

The magnetic field perturbations at a height $\vec{r} < \vec{r}'$ due to the divergence free elementary system is found by the vector potential $\mathbf{A}(\vec{r})$ that correspond to $\mathbf{J_{df,el}}(\vec{r})$. The potential is given by:

$$\mathbf{A}(\vec{r}) = \frac{\mu_0 I_0}{16\pi^2 R_I} \int d^3r' \delta(r' - R_I) \frac{\cot(\theta'/2)}{|\vec{r} - \vec{r}'|} \hat{\phi}' \tag{2.44}$$

The potential can be rewritten by the use of spherical harmonics expansion and derivation of the associated Legendre polynomials to:

$$\mathbf{A}(r, \theta') = \frac{\mu_0 I_{0,df} R_I}{4\pi r \sin(\theta')} \left[\sqrt{1 - \frac{2r\cos(\theta')}{R_I} + \left(\frac{r}{R_I}\right)^2} + \frac{r\cos(\theta')}{R_I} - 1 \right] \hat{\phi}' \tag{2.45}$$

For a detailed description on how to get from Eq. (2.44) to Eq. (2.45) the reader is referred to Appendix A in Amm and Viljanen (1999).

The magnetic field associated with this vector field is found by taking the curl of **A**. Since the potential is purely in the azimuth direction, what is left is:

$$\begin{aligned} \nabla \times \mathbf{A}(r, \theta') = & \frac{1}{r\sin(\theta')} \frac{\delta}{\delta\theta} (\mathbf{A}(r, \theta')\sin(\theta'))\hat{\mathbf{r}}' \\ & - \frac{1}{r} \frac{\delta}{\delta r} (r\mathbf{A}(r, \theta'))\hat{\theta}' \end{aligned} \tag{2.46}$$

Solving Eq. (2.46) gives:

$$B_{r'}(r, \theta') = \frac{\mu_0 I_0}{4\pi r} \left(\frac{1}{\sqrt{1 - \frac{2r\cos(\theta')}{R_I} + \left(\frac{r}{R_I}\right)^2}} - 1 \right) \tag{2.47}$$

$$B_{\theta'}(r, \theta') = -\frac{\mu_0 I_0}{4\pi r \sin(\theta')} \left(\frac{\frac{r}{R_I} - \cos(\theta')}{\sqrt{1 - \frac{2r\cos(\theta')}{R_I} + \left(\frac{r}{R_I}\right)^2}} + \cos(\theta') \right) \tag{2.48}$$

Inverse Matrix Calculation Technique

The SECS model uses an inverse matrix transformation technique to calculate the scaling factors using magnetometer data from n number of stations. This allow the use of the measured disturbances of the geomagnetic field at the ground with magnetometers. These can be expanded into disturbances of the elementary current system (Amm and Viljanen, 1999).

The scaling factors I_0 from Eq. (2.47) and (2.48) comes from the divergence-free current system, since these are the currents responsible for the disturbances on the ground. They are given by:

$$\bar{I_0} = \begin{bmatrix} I_{0,df,1} \\ I_{0,df,2} \\ I_{0,df,3} \\ I_{0,df,4} \\ \vdots \\ I_{0,df,n_{el}} \end{bmatrix} \tag{2.49}$$

where n_{el} is the number of elementary current systems.

The measurements from the magnetometers are stored in the Z-vector, which is given by:

$$\bar{Z} = \begin{bmatrix} Z_{1,\theta} \\ Z_{1,\phi} \\ Z_{2,\theta} \\ Z_{2,\phi} \\ \vdots \\ Z_{n_{obs},\theta} \\ Z_{n_{obs},\phi} \end{bmatrix} \tag{2.50}$$

The scaling factors are solved with the matrix equation:

$$\bar{T}\bar{I_0} = \bar{Z} \quad \Rightarrow \quad \bar{I_0} = \bar{T}^{-1}\bar{Z} \tag{2.51}$$

With the $\bar{T}$ matrix being given as:

$$\bar{T} = \begin{bmatrix} T_{11,\theta} & T_{12,\theta} & \dots & T_{1n_{el},\theta} \\ T_{11,\phi} & T_{12,\phi} & \dots & T_{1n_{el},\phi} \\ T_{21,\theta} & T_{22,\theta} & \dots & T_{2n_{el},\theta} \\ T_{21,\phi} & T_{22,\phi} & \dots & T_{2n_{el},\phi} \\ \vdots & & & \vdots \\ T_{n_{obs}1,\theta} & T_{n_{obs}2,\theta} & \dots & T_{n_{obs}n_{el},\theta} \\ T_{n_{obs}1,\phi} & T_{n_{obs}2,\phi} & \dots & T_{n_{obs}n_{el},\phi} \end{bmatrix} \tag{2.52}$$

The $\bar{T}$ matrix decides the magnetic effect from an elementary current system with $I_0 = 1\,\text{A}$. Where the $\bar{T}$-components $T_{k,l,\{\substack{\theta'\\\phi}\}}$ are the colatitudinal and azimuth

component of the ground magnetic effect, in the same coordinate system as the magnetometer measurements, i.e. the same coordinate system as the $\bar{Z}$-vector.

Single Value Decomposition

Due to the bad conditioning of the T-matrix that comes when $n_{obs} << n_{el}$, which is typically the case, the SECS model apply a technique called Single Value Decomposition (SVD). The $\bar{T}$ matrix is decomposed into:

$$\bar{T} = \bar{U}\bar{\Sigma}\bar{V}^T \tag{2.53}$$

Where $\bar{U}$ and $\bar{V}^T$ are orthogonal matrices, and $\bar{\Sigma}$ is a diagonal matrix with the conditions that its diagonal elements σ_{mm} should be $\sigma_{mm} \leq \epsilon \cdot \max \sigma_{mm}$. The values of ϵ is normally between 0.01 and 0.1. By using this technique the badly conditioned parts of $\bar{T}$ can eliminated. The ϵ-parameter will be referred to as the SVD-parameter from here on out to distinguish it from the unrelated coupling function ϵ described in the AMPS background theory.

The optimal SVD-parameter is dependent on the geographical configurations of the magnetometer set up and thus it is only needed to calculate the optimal SVD-parameter once for the set up that is chosen (Weygand et al., 2011). This will be described in more detail in Section 3.5.

Method

3

The first section in this chapter is a description on which data were used as model inputs, and where this data came from. In the remaining sections the methodology for the different models are presented.

3.1 About the Data

The magnetometer data were obtained by triaxial fluxgate magnetometers at the locations listed in Tab. 3.1, during the period April 2015 to February 2018. The data has been downloaded from the website for Tromsø Geophysical Observatory (2018)[1] (TGO), and the data from Kevo, Kiruna and Kilpisjärvi has been taken from International Monitor for Auroral Geomagnetic Effects (2019)[2]. The magnetometer data files were given with a 1-min time resolution for all the geomagnetic components. Note that only data from Andenes was used in the comparison, however most stations provided data for the SECS model as inputs. Kiruna, Jäkvik and Kilpisjärvi were used only to determine the best Single Value Decomposition parameter that will be discussed in section 3.5.

Station	**Geo. Latitude** [° **N**]	**Geo. Longitude** [° **E**]
Andenes	69.30	16.04
Jan Mayen	70.90	-8.70
Bjørnøya	74.50	19.00
Nordkapp	71.09	25.29
Sørøya	70.54	22.22
Tromsø	69.66	18.94
Dønna	66.11	12.50
Kevo	69.76	27.01
Kiruna[a]	67.84	20.42
Jäkvik[a]	66.40	16.98
Kilpisjärvi[a]	69.06	20.77

Tab. 3.1.: List of magnetometer stations used in thesis.

The magnetograms for the days of interest were chosen based on their Geomagnetic Activity index (GMA) given for the station in Tromsø. The GMA can be found at TGO's website, and it describes the highest mean deviation of the

[1] http://geo.phys.uit.no/ (accessed: May 28, 2019)
[2] http://space.fmi.fi/image/www/index.php?page=home (accessed: May 28, 2019)
[a] Not used as SECS model input.

horizontal component from the daily mean value. For the interest of comparing magnetograms with the AMPS and SECS models, there was a need to include some days which had a higher magnetic activity and some days with a lower activity magnetic level. This is important so that a more accurate sample set of the geomagnetic field were used, since Andenes is located underneath the auroral zone. We limit ourselves to a time period of 24 hours lasting from 12:00 UT to 12:00 UT the next day, since the largest magnetic disturbances occur on the night side. This means that when selecting the days we tried to include some days where typical auroral zone activity, like substorms, could be seen.

The AMPS model input is the IMF B_y and B_z GSM-component, the solar wind velocity v_{sw}, in GSE x-direction (or equivalent x-direction in GSM-coordinates), the tilt of the Earth's dipole magnetic field with respect to the Sun, and the 10.7 cm solar radio flux index $F_{10.7}$. B_y, B_z and v_{sw} were taken from Omniweb (2018)[3] with 1-min time resolution, and the $F_{10.7}$ flux was taken from Space Weather Canada (2018)[4]. The flux is given for three times a day, generally at 18:00, 20:00 and 22:00 UT, and sometimes at 17:00, 21:00 and 23:00 UT. For the AMPS input the $F_{10.7}$-value at 18:00 (17:00) UT was chosen for the relevant days. The solar radio flux comes in three variants: the observed, adjusted and URSI Series D value. The observed $F_{10.7}$ was used, since this is the one Space Weather Canada[5] recommend for studying terrestrial phenomena.

The dipole tilt angle was calculated using the *dipole*-python module found at `https://github.com/klaundal/dipole` (accessed: May 29, 2019). The input data used in the AMPS model are included as plots in Appendix B.

Date	**GMA index [nT]**	**day 1, day 2: $F_{10.7}$ [sfu]**
Feb 13-14 2018	9	76.6, 74.5
Mar 26-27 2017	68	75.7, 83.4
Apr 22-23 2017	158	82.8, 83.6
Dec 16-17 2017	29	71.8, 71.5
Dec 22-23 2017	11	76.1, 76.6
Jan 27-28 2016	7	116.4, 111.3
Apr 26-27 2015	13	119.9, 109.3
May 13-14 2015	80	164.7, 148.5
Jun 21-22 2015	25	133.0, 130.1
Nov 20-21 2015	10	110.5, 122.4

Tab. 3.2.: Days chosen for comparison between models and measurements.

[3] https://omniweb.gsfc.nasa.gov/ (accessed: May 29, 2019)
[4] https://spaceweather.gc.ca/solarflux/sx-en.php (accessed: May 29, 2019)
[5] The different types of fluxes are described in the *About the Solar Flux Data* section in Space Weather Canada (2018)

Tab. 3.2 shows the 10 days that were chosen to compare with model outputs. The GMA index is taken 12:00 UT on day two, for instance Feb 14 2018 12:00 UT, since it represent the geomagnetic activity level for the past 24 hours. The $F_{10.7}$ value is given for both the first and the second day. The first value is used when the AMPS models the external field on the first day, for instance Feb 13 2018. After midnight the second value is the model input. From this point forward *one day* is considered to be the 24 hour period going from 12:00 UT to 12:00 UT.

3.2 Execution: Magnetogram Data File

Quiet Level Adjustments and Equations

The magnetometer data files gives the total geomagnetic field changes for Horizontal (H), Declination (D), Inclination (I), Vertical (Z)-components as well as a total geomagnetic field measurement (F). To be able to compare the data files with the AMPS model, and the SECS model, we need to only consider the perturbed magnetic field, i.e. the quiet day values (QDV) is subtracted from each components. The SECS model uses the perturbed geomagnetic field as input, so the QDV is subtracted from the data for all magnetic data that is fed into the model. TGO automatically calculate the QDV using a least-square-root approximation for each component a:

$$\sum_i \sqrt{|a_i - a_q|} = min \tag{3.1}$$

where a_i is a data point for a $10 \cdot 24$ hour day period. The sum is several times calculated for a a_q lowest possible quiet day value to a highest possible quiet day value to find a final minimum, which is then the quiet day value for the component in question. This process is discussed in Edvardsen et al. (2013).

The quiet day values for the X, Y and Z-component for the relevant days in this comparison was found with a python script written by Magnar G. Johnsen at TGO which follows the same approach as described above, only instead of using 10 days prior to the day in question it uses 5 days prior and 5 days after to calculate the values.

The set of geographical Cartesian components used in the comparison is then given by:

$$\Delta X_0 = H \cos D - X_{QDV} \tag{3.2}$$

$$\Delta Y_0 = H \sin D - Y_{QDV} \tag{3.3}$$

$$\Delta Z_0 = Z - Z_{QDV} \tag{3.4}$$

where X, Y, Z is the local northward, eastward and downward components respectively.

Adjusting for Contribution from the Induced Ground Geomagnetic Field

The components were multiplied with $B_{int,factor}$ to correct for the ground induced internal currents in the Earth's crust and mantle. The value was chosen based on the results of Tanskanen et al. (2001), who found that during substorm onset the geomagnetic field perturbations at ground could have contributions from ground induced current as large as 40% of what is measured. However, on average this value would be around 10-20% for magnetometers on land, and around 20-25% for magnetometers surrounded by water. Since Andenes is an island bordering the sea, the higher values were therefore considered when deciding $B_{int,factor}$, which was multiplied with the data right before plotting. Since in reality the internal field factor changes based on how disturbed the geomagnetic field is, multiplying it with only a single number is not ideal, and thus $B_{int,factor}$ was chosen to change in correlation to how large the perturbation in the X and Y-component was. The multiplication factor chosen for different perturbation amplitudes is shown in Tab. 3.3.

$\lvert\Delta X \text{ or } \Delta Y\rvert$ [nT]	$B_{int,factor}$
<10	0.85
10-20	0.80
20-30	0.75
30-100	0.70
>100	0.60

Tab. 3.3.: Percentage of external geomagnetic field contributions during different disturbance levels.

The multiplication factor is calculated for each of the horizontal components, but the vertical component has been left as is. There are two reasons for this. The first is that the vertical component is not discussed in Tanskanen et al. (2001) and therefore there is no indication of how large part of the vertical measured field is due to the induced currents. The second reason is that if we imagine an oppositely orientated line current going out of the paper under the ground in Fig. 2.1, we see that at our point of measuring the vertical component would be reduced due to the line current in the ground, instead of enhanced like in the horizontal component.

$B_{int,factor}$ is highly simplified since in reality the internal contributions to the measured field depends on the ground conductivity, the frequency of the

measured external signal and the distance to the current, among other things. These consideration are discussed thoroughly in Tanskanen et al. (2001), but will not be discussed further for this comparison.

3.3 Execution: AMPS

The AMPS output for the geomagnetic field perturbation was modelled using the function *get_B_ground* with input altitudes 0 km and 90 km, and with input data from OMNIweb for the relevant days. The *get_B_ground*-function output is the east, north and upward magnetic field perturbations in quasi-dipole coordinate systems, and the function uses the equations described in section 2.1. Eq. (2.9), Eq. (2.10) and Eq. (2.11) were used to convert back to a local geocentric ENU system, where the upward component is multiplied by -1 before plotting. The equations requires the unit vectors $\hat{\mathbf{e}}$, $\hat{\mathbf{n}}$ and $\hat{\mathbf{k}}$, which is simply:

$$\hat{\mathbf{e}} = [1, 0, 0] \tag{3.5}$$

$$\hat{\mathbf{n}} = [0, 1, 0] \tag{3.6}$$

$$\hat{\mathbf{k}} = [0, 0, 1] \tag{3.7}$$

The unit vectors can be found using the right hand rule, and only include 1's and 0's since both $\mathbf{f_1}, \mathbf{f_2}$ and ΔB_e, ΔB_n and ΔB_u are given in local east, north and upwards coordinates.

Before the 1-min OMNI data was used in *get_B_ground* it went through a 20-min window moving averaging process to account for the time shift from the bow shock to the magnetosphere. Another option is to simply time shift the data itself, however this may cause errors due to all simplification that has to be done to get a time-value. A flat time delay given by $t = L/v_{sw}$ is the simplest method. However, here a necessary mean value for both the distance to be shifted L, and the solar wind velocity is necessary, and therefore t would not be representative for the entire 24 hour day. The OMNI data itself has already been time shifted from the L1 Lagrangian point to the Earth's bow shock by the method described on the OMNI website[6].

3.4 Execution: SLCA

For the simple line current approximation the internal induced geomagnetic field was considered to contribute nothing to the measurements ($B_{int,factor} = 1$) for all the components, since the contribution is assumed to decreases with increasing

[6] `https://omniweb.gsfc.nasa.gov/html/ow_data.html` (accessed: May 28, 2019)

height and will be small. The SLCA calculation followed the approach described in Section 2.2 for the magnetometer data as well as for the AMPS 0 km model output. When AMPS SLCA was executed ΔX, ΔY and ΔZ is simply replaced with ΔN_{AMPS}, ΔE_{AMPS} and $-\Delta U_{AMPS}$ respectively, and calculations are performed in the same fashion as for SLCA Magnetogram. The SLCA AMPS input is the results of Eq. (2.9), Eq. (2.10) and Eq. (2.11).

3.5 Execution: SECS

The Spherical Elementary Current System model was available with an open source python library called *USGS Geomagnetism Program - Interpolated Magnetic Perturbations (Geomag-IMP)*. The script used in this comparison has been adapted from the *make_imp_secs.py*-file by Magnar G. Johnsen, and run with the support of the function file SECS.py. Both files can be found at `https://github.com/usgs/geomag-imp` (accessed: May 29, 2019).

To estimate the geomagnetic field perturbations at Andenes with the SECS model we used magnetometer data from 8 stations surrounding Andenes as input data: Dønna (DON), Andenes (AND), Tromsø (TRO), Sørøya (SOR), Nordkapp (NOR), Bjørnøya (BJN), Jan Mayen (JAN), and Kevo (KEV), see Tab. 3.1. Fig. 3.1 shows the entire magnetometer network that are a part of the International Monitor for Auroral Geomagnetic Effects (IMAGE) [7]. This map includes all stations used in the model, except for Jan Mayen which is an island located west in the Norwegian sea (geographical latitude $= 70.9$ °N, geographical longitude $= -8.70$ °E). The stations were chosen based on their data coverage and their position relative to Andenes. The number of stations were initially chosen for simplicity and to save time. A large amount of stations might improve the performance for the entire prediction grid, but would be outside the scope of this thesis since we are only interested in the model outputs at Andenes.

Initially, the model was run with Røst and Masi (MAS), but due to lack of data for some of the days these stations had to be switched out with Dønna and Kevo respectively. Jan Mayen also lacked data for some days close to February 14 2015 making it impossible to calculate the QDV with the method described in section 3.2. Due to the uniqueness of the position of Jan Mayen relative to Andenes, it was decided to change the date, rather than the station. The original date February 13-14 2015 was changed to the June 21-22 2015, which was found to be of similar geomagnetic activity. There are also a few hours of data missing from Nordkapp on May 13 2015 which results in a lack of model output for those hours.

[7] http://space.fmi.fi/image/www/index.php?page=home (accessed: May 29, 2019)

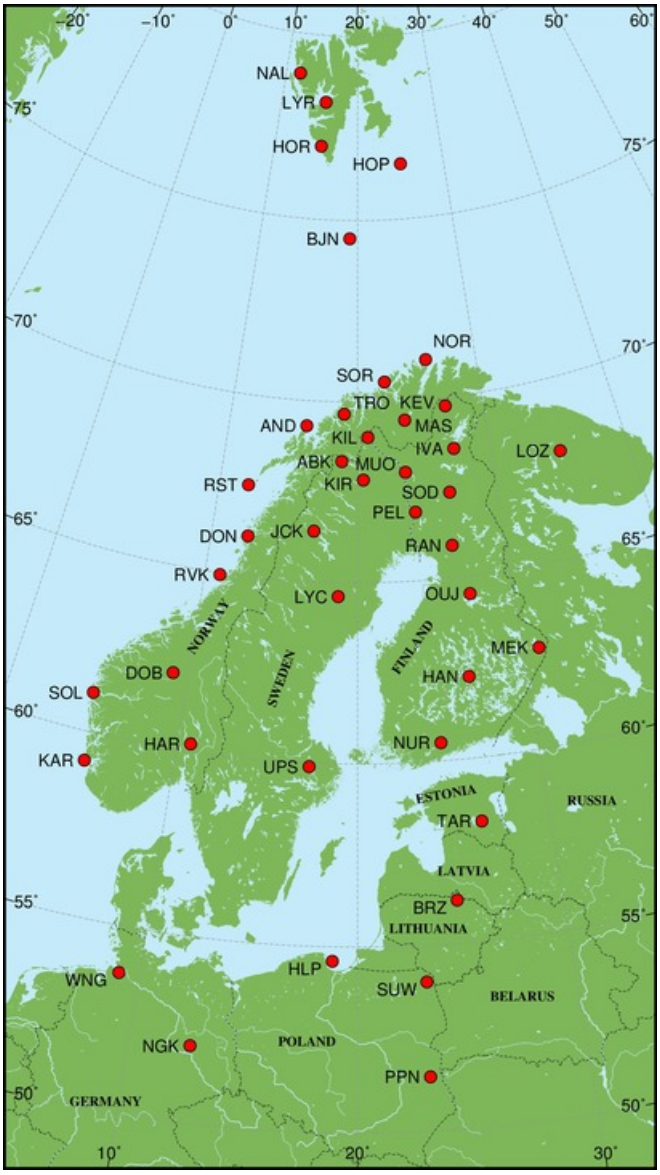

Fig. 3.1.: IMAGE magnetometer network. Picture borrowed from International Monitor for Auroral Geomagnetic Effects, 2019.

The model parameters are summarized in Tab. 3.4. The SECS grid was set so that it covered all the stations used in the comparison. The prediction grids was chosen to be made up of all stations that were used as model inputs in addition to three extra stations: Kiruna, Jäkvik and Kilpisjärvi. These stations were used when deciding which SVD-parameter that gave the best fit.

The SVD-parameter used in the SECS model have been chosen to be the parameter that gives the best fit for *all* stations used in the prediction grid, rather than having different values for each day and only at Andenes. To find the best parameter the model outputs at ground level were compared with the magnetometer data for stations that were not used as model inputs: Kiruna,

Variable	
Earth radius [km]	$R_E = 6371$
Height of ionosphere [km]	$H_i = 110$
Prediction height [km]	$H_p = 0$ and $H_p = 90$
SECS latitude [°N]	60 to 80
SECS longitude [°E]	-12 to 35
Prediction grid	Lat and Lon from Tab. 3.1
SVD-parameter	0.021

Tab. 3.4.: SECS model variables.

Jäkvik and Kilpisjärvi. The prediction grid consists of the latitudes and longitudes for the magnetometer stations listed in Tab. 3.1. We let the SVD-parameter vary from 0 to 0.1 for 30 values, and then calculated both the Root Mean Square Error (RMSE) as well as the Mean Absolute Error (MAE) for each component for one station:

$$RMSE = \sqrt{\frac{\sum_i^N (X_i - X_{SECS,i})^2}{N}} \tag{3.8}$$

$$MAE = \frac{\sum_i^N |X_i - X_{SECS,i}|}{N} \tag{3.9}$$

where i is a minute during the day and N is the total number of minutes. The RMSE and MAE was calculated for the Y and Z-components in the same fashion. The total RMSE and total MAE were found by adding all components for all the three stations together.

Fig. 3.2 shows the Total RMSE and Total MAE as a function of SVD-parameter, for both a set of magnetometer data input containing Jan Mayen (e.g. Total RMSE) and without (e.g. Total RMSE JAN). Both the total RMSE and total MAE were calculated with and without Jan Mayen as model input. This was done to check if the distance to the other stations and Jan Mayen would be too large to have a positive contribution to the model output or not. Fig. 3.2 shows that the distance does affect the performance of the model depending on which SVD-parameter that is used. We decided to use the lowest Total RMSE (both with and without Jan Mayen) since RMSE weights large deviations from the measurements more, as opposed to MAE where all the deviations are weighted equally. This means that the SVD-parameter that gave the lowest Total RMSE happened to be $SVD_{parameter} = 0.021$ where Jan Mayen was included as model input.

Another method of choosing the best SVD-parameter is described in (Weygand et al., 2011), where they looked at the total integrated difference between the modelled scaling factor I_0 and the derived scaling factor from the magnetome-

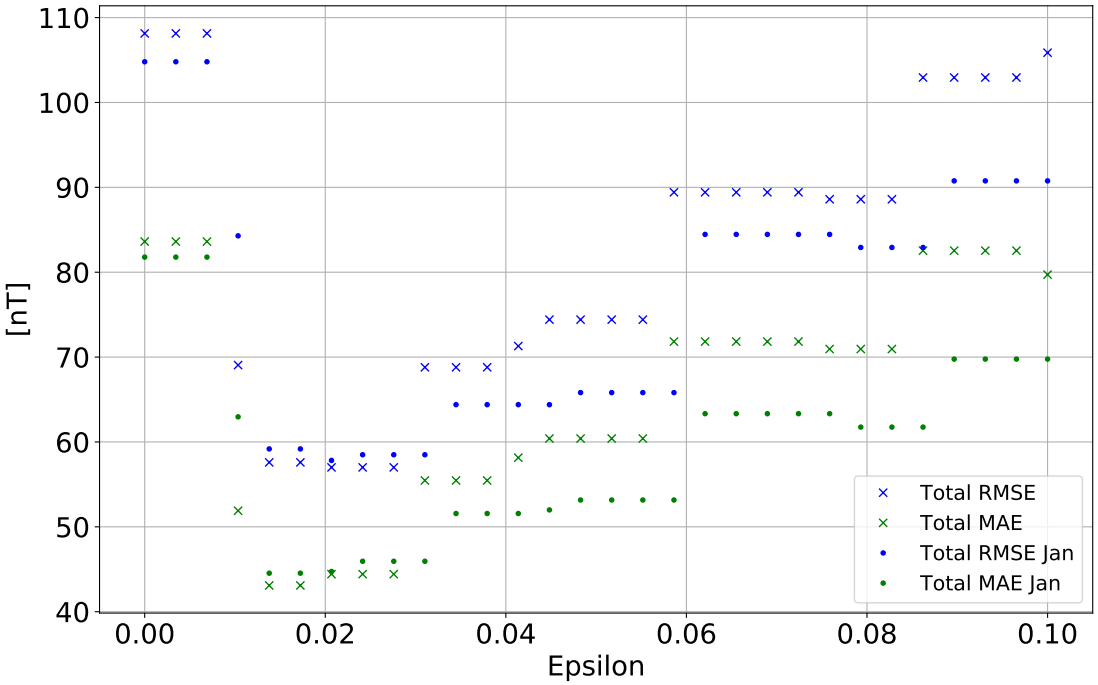

Fig. 3.2.: Total RMSE and total MAE between SECS model outputs and measured data from Kiruna, Jäkvik and Kilpisjärvi. Total RMSE and Total MAE indicates the error with JAN included as model input. Total RMSE JAN and Total MAE JAN is errors when JAN is not included.

ter data. This method was not used as their method of deriving the scaling factors would be out of the scope of this thesis.

3.6 Altitude Dependency of the Geomagnetic Field Perturbations

Finding how the magnetic field perturbations varies over different altitudes, allows the model outputs to be compared with results from the MOM-project in the future. The Sodium-LIDAR is only able to measure the scalar total geomagnetic field and thus only the total magnetic field perturbations needs to be considered when looking at altitude variations. We decided to look at how the perturbations changed from ground level to 110 km. The models looped over the different heights, h, and the following equations were used to get the total field at those heights:

$$X_{h,model} = \Delta X_{h,model} + X_{h,IGRF}$$
$$Y_{h,model} = \Delta Y_{h,model} + Y_{h,IGRF}$$
$$Z_{h,model} = \Delta Z_{h,model} + Z_{h,IGRF}$$

The total magnetic field is found with $B_{h,model} = \sqrt{X^2_{h,model} + Y^2_{h,model} + Z^2_{h,model}}$. The total magnetic field perturbations are found with:

$$\Delta B_{h,model} = B_{h,model} - B_{h,IGRF} \tag{3.10}$$

The subscript IGRF indicates the international geomagnetic reference field values for relevant day at the location of Andenes for the different heights. The IGRF values where given with the python module *igrf12* found at `https://github.com/scivision/igrf12` (accessed: May 29, 2019). The IGRF model inputs are decimal year, height and geographic latitude and longitude.

3.7 Correlation Analysis

We performed a simple correlation analysis to quantify the goodness of the fit between the model outputs and the measured data. The correlation factor was given by:

$$c = \frac{cov(x, y)}{\sqrt{s^2_x \cdot s^2_y}} \tag{3.11}$$

where $cov(x, y) = \frac{\sum(x-\bar{x})(y-\bar{y})}{n-1}$ is the co-variance between x and y and s^2_x and s^2_y is the sample variance for x and y respectively. Here x and y are arbitrary input parameters, and n is the sample length for the parameters.

The correlation analysis was done in the ground comparison, $c_{0,AMPS}$, between the magnetogram data adjusted for internal field contribution and the AMPS model output. The correlation between the SECS model output and the magnetogram data was named $c_{0,SECS}$. At 90 km the correlation analysis, $c_{90,AMPS}$, was done for the AMPS SLCA output and the AMPS model output. We also performed a correlation analysis between the SLCA magnetogram output and the SECS model output for 90km, $c_{90,SECS}$. The output of the analysis c_0 and c_{90} for both models are found in Tab. 4.1 and Tab. 4.2 in section 4.

Results from Selected Days

4

In this chapter we present the resulting plots from three out of the ten days used in this thesis. The rest of the results can be found in Appendix A. The days chosen are April 22-23 2017, November 20-21 2015 and June 21-22 2015. The first day has been chosen as an example of a day where AMPS has a fairly good fit with the adjusted magnetometer data and June 21-22 2015 has been selected as an example of a poor fit to the measurements. November 20-21 2015 has been chosen because the AMPS model output seem to produce a small substorm, which can also be seen in the magnetometer data.

4.1 Results from Correlation Analysis

Tab. 4.1 and Tab. 4.2 shows the results from the correlation analysis performed on the different graphs on the ground and in space. $c_{0,AMPS}$ is the correlation factor between the measured ground magnetic field that has been adjusted to remove contributions from induced ground currents and the *get_B_ground*-function output. $c_{0,SECS}$ is the correlation factor between the measurements and the SECS modelled ground perturbations. For 90 km we perform a correlation analysis, given as $c_{90,AMPS}$, between the *get_B_ground*-function and the SLCA AMPS outputs. The correlation between SLCA Magnetogram data and the SECS model output is given as $c_{90,SECS}$.

	$c_{0,AMPS}$			$c_{0,SECS}$		
Date	**X**	**Y**	**Z**	**X**	**Y**	**Z**
13-14 Feb 2018	0.54	0.53	-0.18	1	1	0.996
26-27 Mar 2017	0.77	0.77	0.58	1	1	1
22-23 Apr 2017	0.81	0.43	-0.02	1	1	0.999
16-17 Dec 2017	0.57	0.69	0.45	1	1	0.999
22-23 Dec 2017	0.59	0.72	0.64	1	1	0.999
27-28 Jan 2016	0.37	0.36	0.44	1	1	0.999
26-27 Apr 2015	0.58	0.83	-0.01	1	1	0.989
13-14 May 2015	0.48	0.81	0.15	1	1	0.999
21-22 Jun 2015	0.60	0.73	-0.49	0.999	1	0.997
20-21 Nov 2015	0.58	0.79	0.39	1	1	0.999

Tab. 4.1.: Results from the correlation analysis on ground.

A general note in regards to the correlation analysis is that the factors c_0 and c_{90} simply describe how well the two graphs increase and decrease in accord with

	$c_{90,\mathrm{AMPS}}$			$c_{90,\mathrm{SECS}}$		
Date	**X**	**Y**	**Z**	**X**	**Y**	**Z**
13-14 Feb 2018	0.89	0.67	0.66	0.53	0.65	0.77
26-27 Mar 2017	0.79	0.81	0.75	0.73	0.66	0.77
22-23 Apr 2017	0.89	0.82	0.91	0.72	0.56	0.74
16-17 Dec 2017	0.91	0.85	0.58	0.79	0.61	0.72
22-23 Dec 2017	0.79	0.66	0.72	0.67	0.60	0.74
27-28 Jan 2016	0.87	0.65	0.69	0.53	0.60	0.85
26-27 Apr 2015	0.64	0.76	0.71	0.78	0.84	0.62
13-14 May 2015	0.86	0.63	0.80	0.65	0.49	0.76
21-22 Jun 2015	0.89	0.62	0.52	0.63	0.55	0.70
20-21 Nov 2015	0.97	0.88	0.67	0.77	0.77	0.68

Tab. 4.2.: Results from the correlation analysis at 90 km.

each other. Therefore, information about the magnitude of the increase/decrease of the spikes is lost in this factor, and can therefore not be used on its own to decide the goodness of fit.

4.2 Results at 0 km

Fig. 4.1, Fig. 4.2 and Fig. 4.3 shows the results from the comparison on the ground between the measurements and the model outputs. Here it can be seen that the SECS model performs better than the *get_B_ground*-function from the AMPS model. The fit between the SECS model output and the measured data are considered almost perfect, where the Y-component in Fig. 4.3 is considered to be the component with the worst fit, based on visual inspection. This is considered true for all components in all the ten days. The correlation analysis indicates that the Z-component in Fig. A.6 (See Appendix A) has the worst fit, however $c_{0,SECS}$ is still 0.989 and can be considered close to perfect.

It can be seen from the relatively poor fit to the adjusted magnetometer data that the *get_B_ground*-function does not perform in an optimal way. This is also true for the rest of the days that are shown in Appendix A. In Fig. 4.1 it can be seen immediately that this is a very disturbed day. It is in fact a geomagnetic storm occurring from the 22^{th} to the 26^{th} of April 2017[1], and the X-component correlation factor between AMPS and the measurements are the highest of all the $c_{0,AMPS}$ factors. It is $c_{0,AMPS,x} = 0.81$ and can be considered a good correlation. The day with the best *overall* correlation factor on ground level between AMPS and the adjusted measurements are March 26-27 2017 (see Fig. A.2 in Appendix A), where both the X and Y component from AMPS do reproduce the disturbances

[1]We used the geomagnetic index found at TGO for this period to check this. `http://flux.phys.uit.no/AscActIx/` (accessed: May 29, 2019)

happening between 02:00 UT to 07:00 UT, despite the amplitudes in the AMPS outputs being lower than the measurements.

In Fig. 4.2 both the X and the Y-component from the AMPS model has a shape that appears very similar to the adjusted measurements. This figure shows what can resemble a small substorm between 00:00 and 04:00 UT, while the rest of the day has low magnetic activity. In fact the GMA index was only 10 for this day, see Tab. 3.2. The AMPS model outputs for the X and Y component are similar to the adjusted measurements. If only considering the shapes of the model outputs the X and Y component has the best goodness of fit. However, there is a time delay between the peak of the modelled depression and the small substorm. The reason for the time delay will be discussed in section 5. The Y-component has the best correlation factor between the three components, but if there was no time delay between the two peaks in the X-component we believe the X-component would have the highest correlation factor. It might even have the highest off all $c_{0,AMPS}$ factors. The Z-component has no correlation between the AMPS output and the measurements, see Tab. 4.1. In Fig. 4.2 it can be seen that the AMPS *get_B_ground*-function Z-component has a poor fit to the measurements.

The last day, June 21-22 2015, given in Fig. 4.3 is an example of a day where the AMPS model produces a poor fit. AMPS produces some of the disturbances during this day, especially the ones at 05:00-08:00 UT in the X-component, but in Tab. 4.1 the Z-component has a fairly high negative correlation with the measured data. It is the same code that has been run for all days, and therefore the negative correlation is not a case of forgetting to multiply ΔB_u with -1 before plotting. The reason behind this negative correlation will be discussed in section 5. There are also cases of disturbances from the model and the measurements being oppositely directed in the horizontal components. It can be seen in the beginning in the X-component from 12:00 UT to 14:00 UT. In the Y-component the small disturbance occurring right after 00:00 UT.

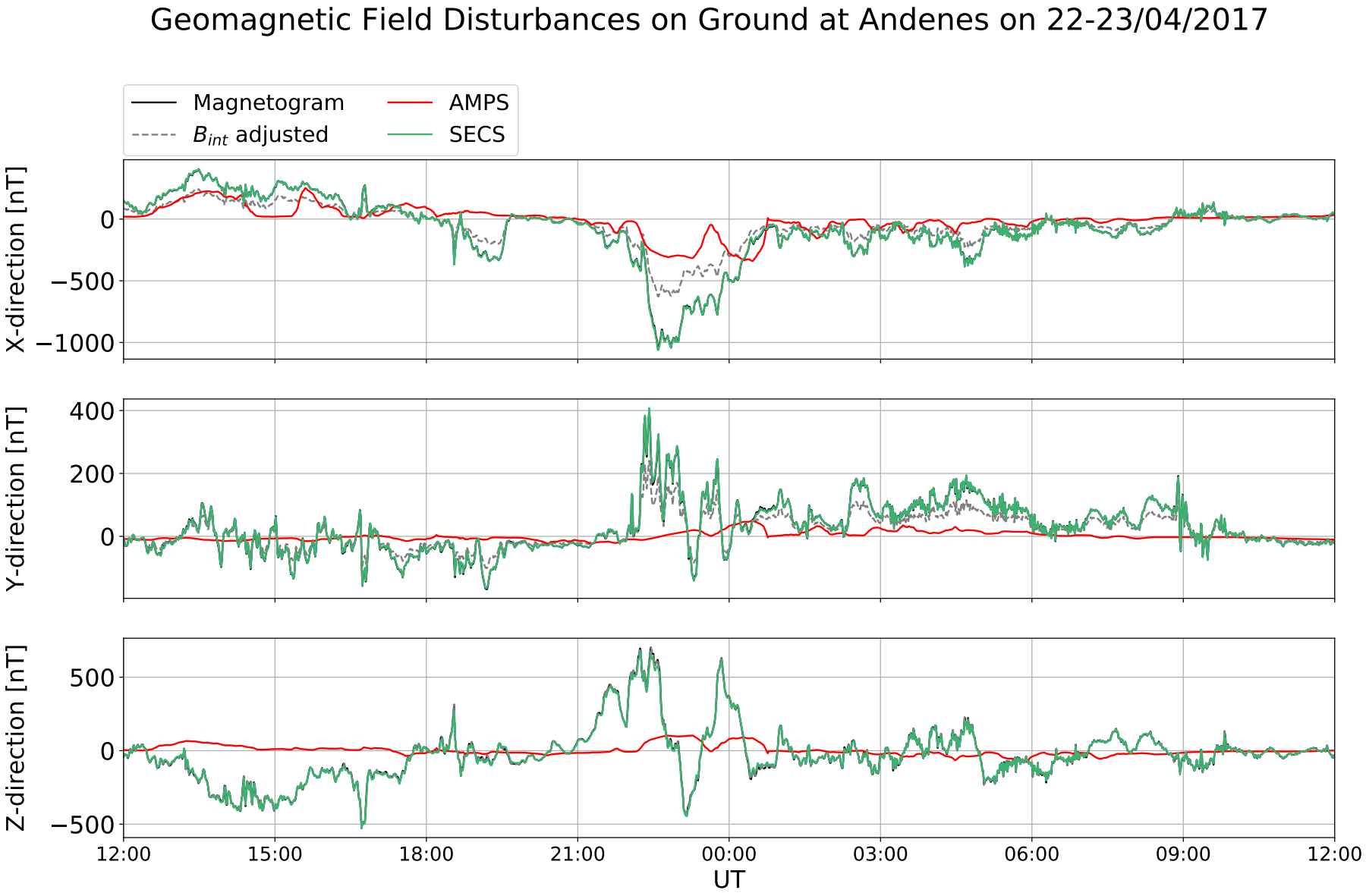

Fig. 4.1.: Measured and modelled ground magnetic perturbations for 0 km at Andenes for April 22-23 2017.

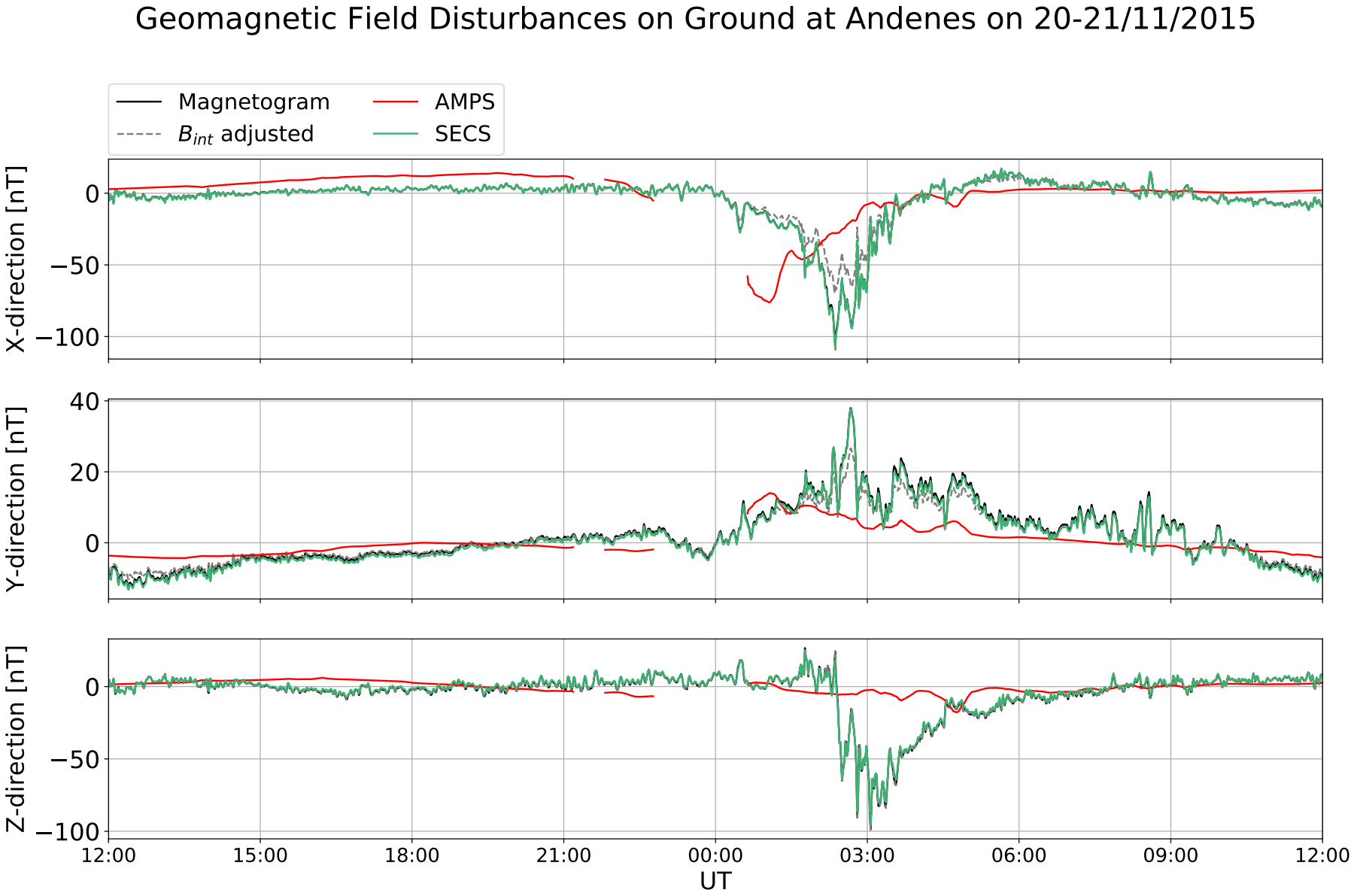

Fig. 4.2.: Measured and modelled ground magnetic perturbations for 0 km at Andenes on November 20-21 2015.

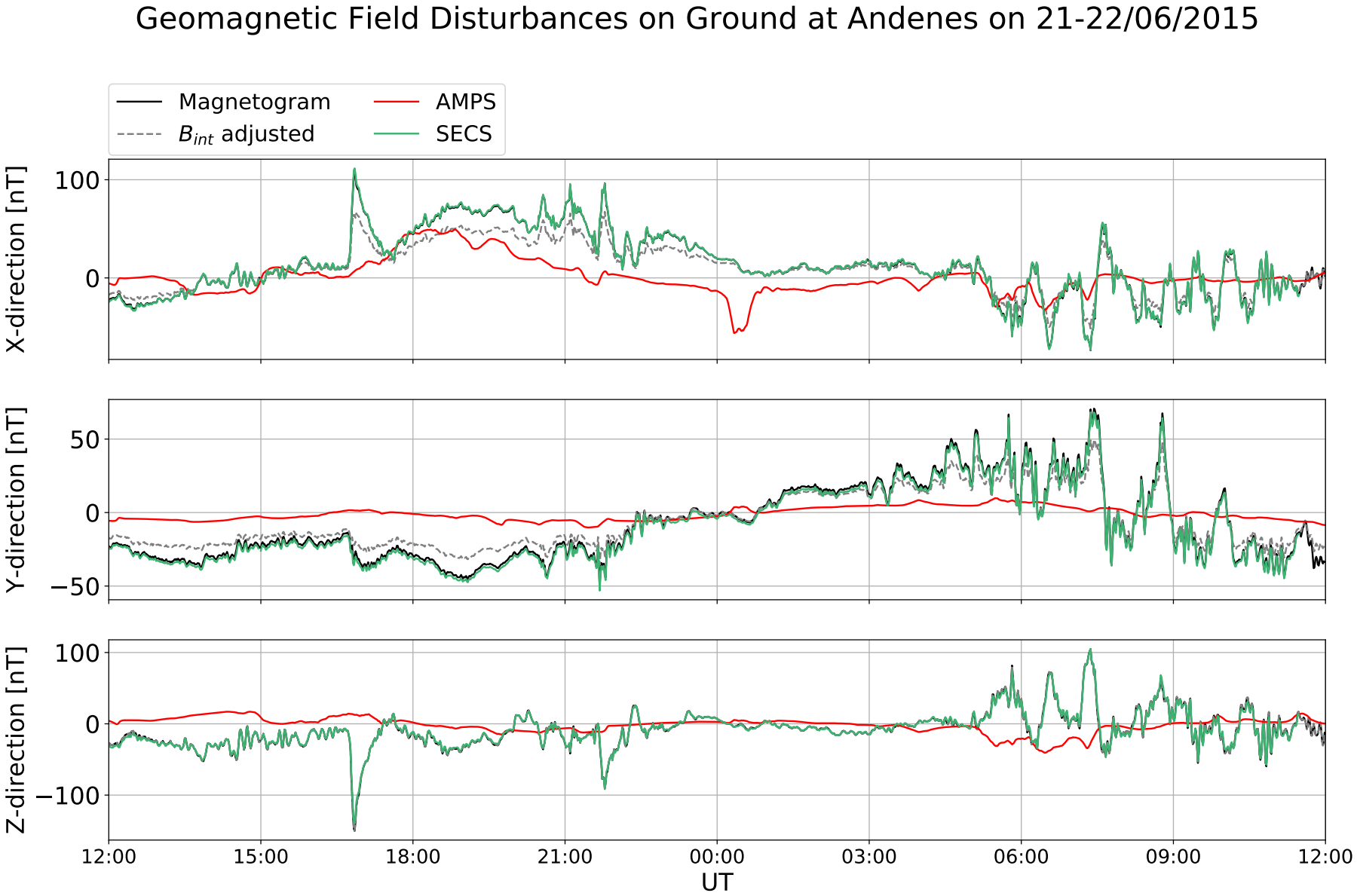

Fig. 4.3.: Measured and modelled ground magnetic perturbations for 0 km at Andenes on June 21-22 2015.

4.3 Results from 90 km and Model Outputs with Varying Altitudes

In this section the results from the simple line current approximation as well as the two advanced models is included, and they are all plotted together. Therefore, there are some perturbations that have been highly amplified, due to the nature of a magnetic field induced from a line current. We generally consider the very large spikes from the SLCA Magnetogram output to be too large, and for the purpose of comparing the different model outputs the y-limits have been adjusted when considered necessary in the figures containing the model outputs at 90 km. For the figures where the y-limits have been adjusted it is noted in the caption. This is also true for the 90 km figures in Appendix A.

For the 90 km altitude comparison between the models the AMPS and SLCA AMPS outputs have been plotted in the column on the left and the SLCA Magnetogram and SECS in the column on the right. The outputs have been grouped together dependent on how similar they are, and they were split into two groups so that the disturbances from AMPS could be seen better. Since the models have the same y-axis, sometimes AMPS outputs appear completely flat even if it is not the case. This is especially true for the Y-component.

Fig. 4.5, Fig. 4.8 and Fig. 4.11 shows the total field magnetic variations at 0 km and at 90 km. Here it can be seen that none of the model outputs change drastically with height, yet there are some changes in the amplitudes of the different perturbations. These altitudes variations are most clear in Fig. 4.6, Fig. 4.9 and Fig. 4.12 for the SLCA AMPS and AMPS section of the figure. The figures shows the model outputs for altitudes from 0 km to 110 km. However, in Fig. 4.8 at 03:00 UT it can be seen that the SECS model produced an increased perturbation for 90 km compared to 0 km. This altitude variation can also be seen in Fig. 4.9, indicating that all three models produces changes in the magnetic field perturbations at different heights.

It can also be seen that the poor fit of the AMPS Z-component in Fig. 4.2 transfer to the AMPS total magnetic field perturbations in Fig. 4.8. Fig. 4.7 shows that SLCA AMPS Z-component has stronger perturbations than AMPS Z-component. This is the reason why SLCA AMPS total magnetic field perturbations in Fig. 4.8 has a more similar shape to the SECS model output. In both Fig. 4.11 and Fig. 4.5 a visual negative correlation is seen between the SECS model output and SLCA AMPS output, and also for the AMPS outputs.

Tab. 4.2 shows that $c_{90,AMPS}$ are all quite high, which is expected since the ground output from AMPS is the input in SLCA AMPS. More surprisingly is that the table shows there is a fairly good correlation between the SECS model output

and SLCA Magnetogram outputs. The Fig. 4.4, Fig. 4.7 and Fig. 4.10 below also support this visually.

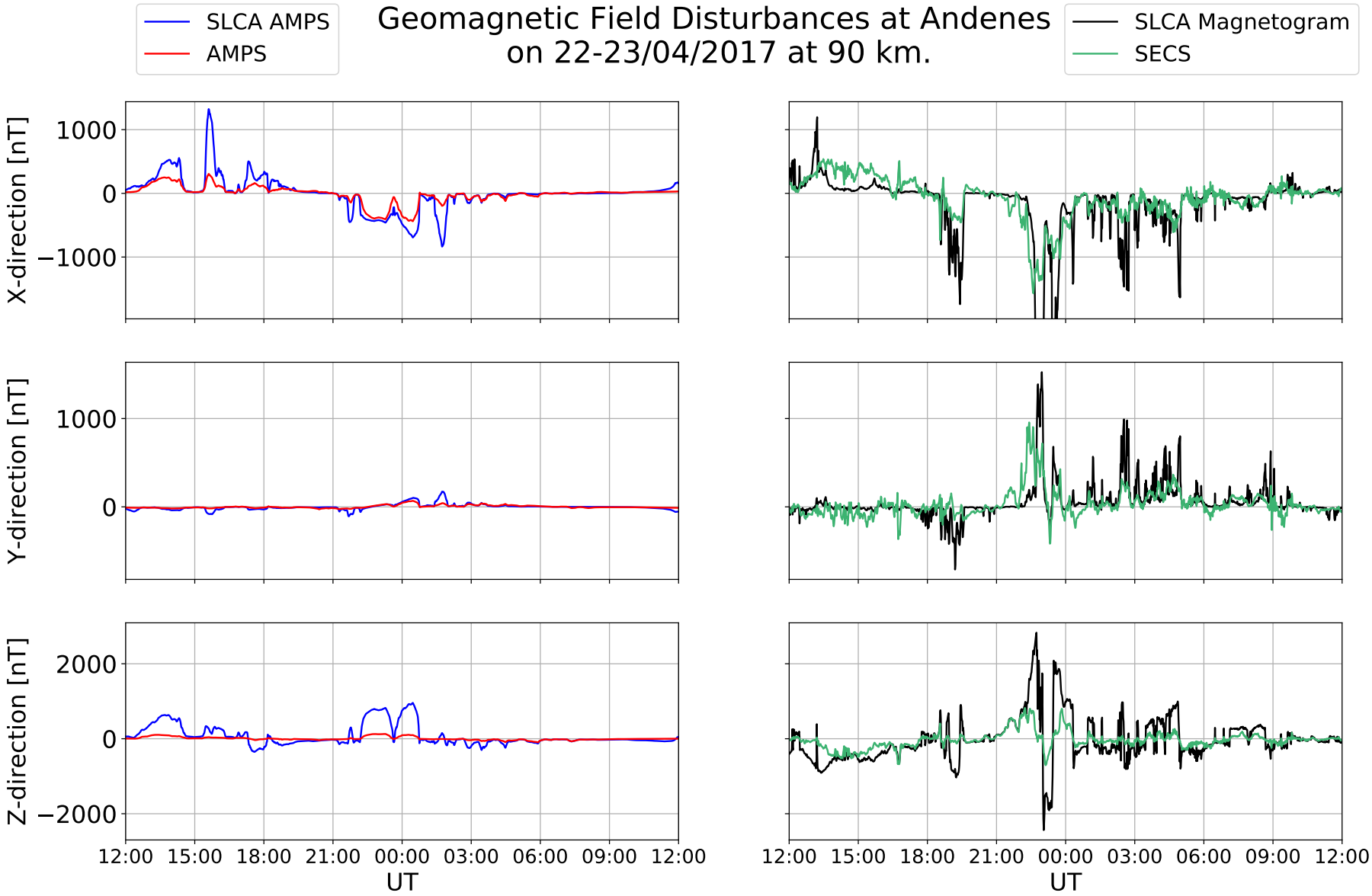

Fig. 4.4.: Modelled magnetic field at 90 km altitude over Andenes on April 22-23 2017. The y-limits in this figure has been adjusted.

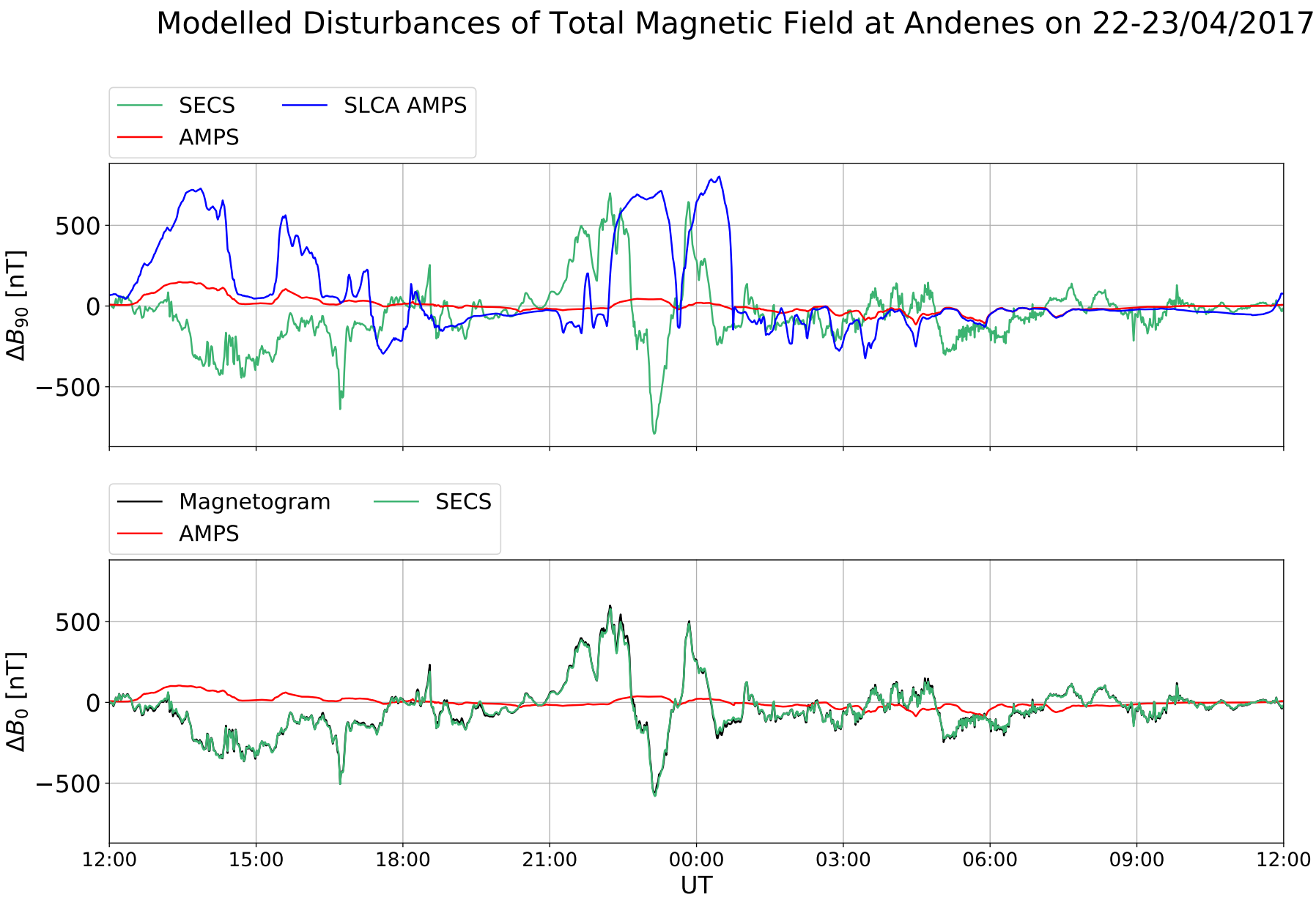

Fig. 4.5.: Total magnetic field perturbations for 0 km and 90 km at Andenes on April 22-23 2017

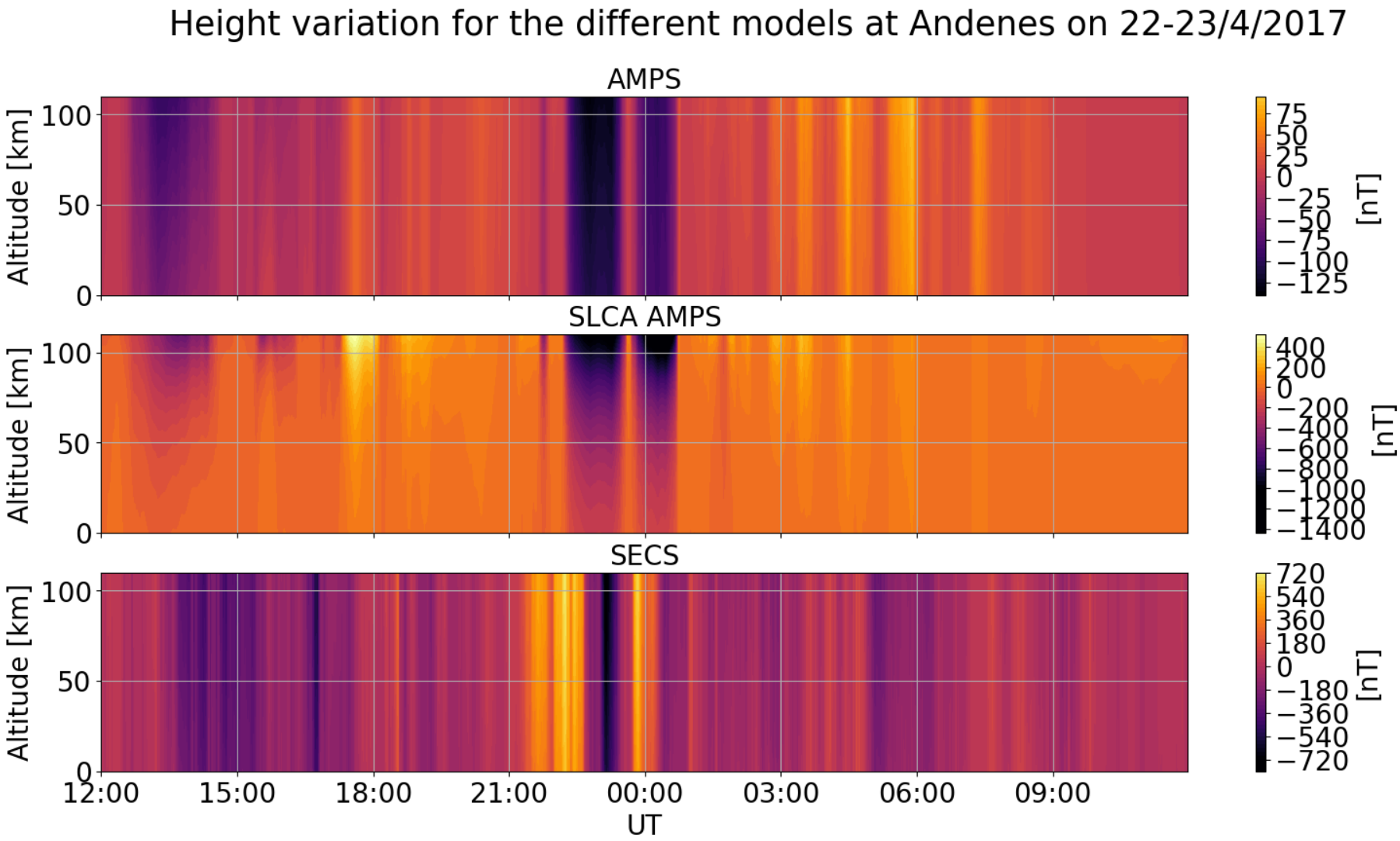

Fig. 4.6.: Altitude variation in total magnetic field perturbations from 0 to 110 km using AMPS, SLCA and SECS outputs over Andenes on April 22-23 2017.

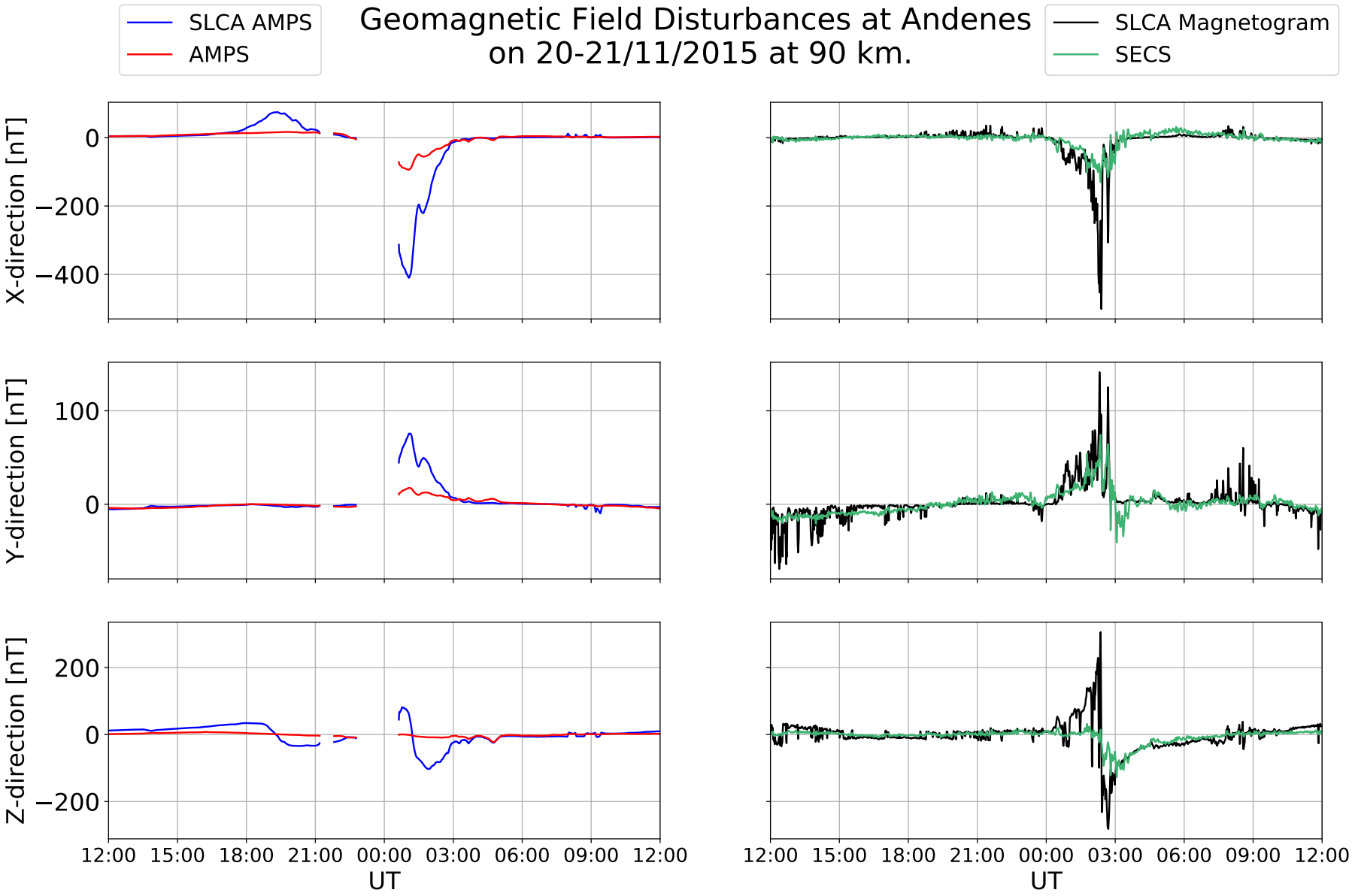

Fig. 4.7.: Modelled magnetic field at 90 km altitude over Andenes on November 20-21 2015.

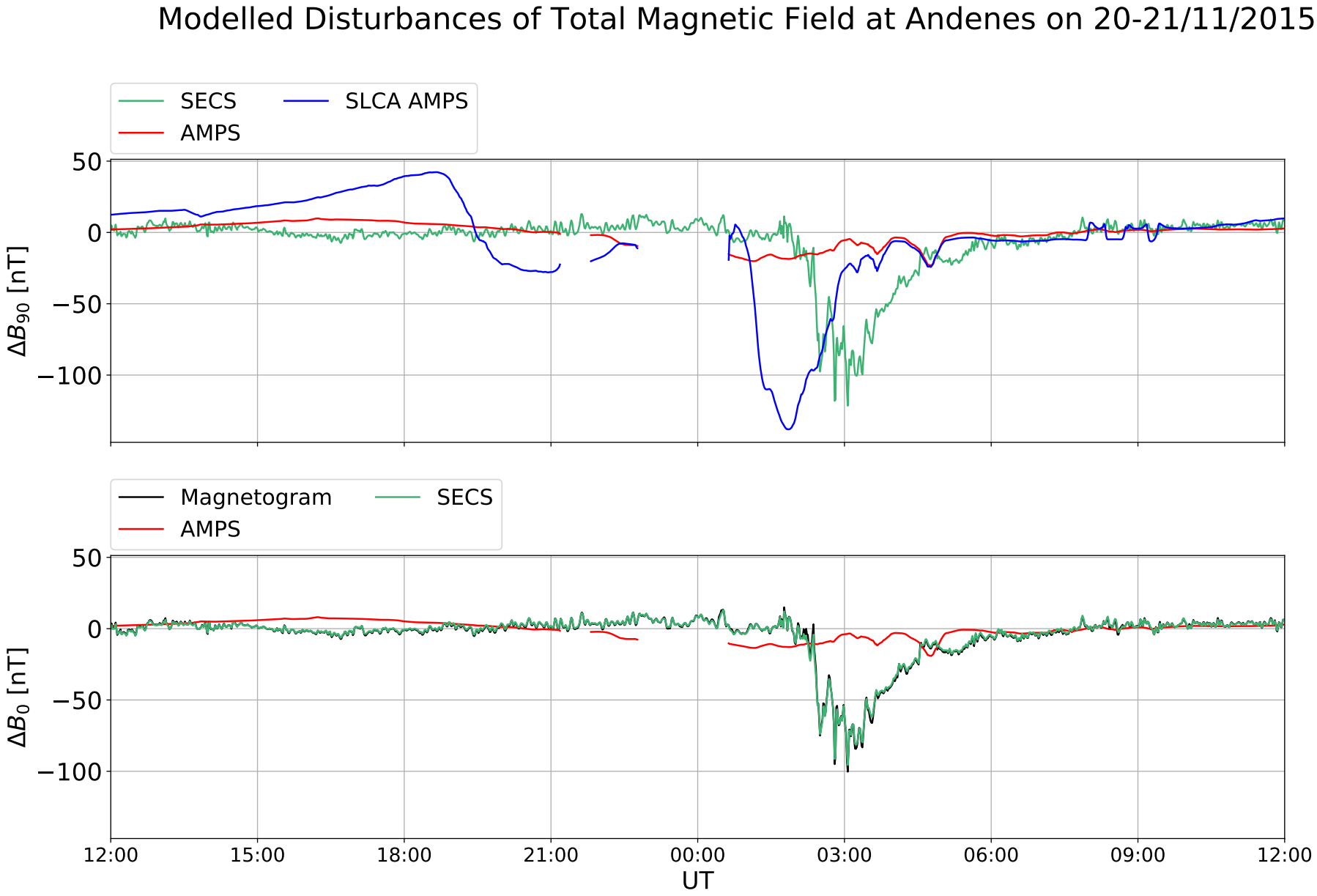

Fig. 4.8.: Total magnetic field perturbations for 0 km and 90 km at Andenes on November 20-21 2015.

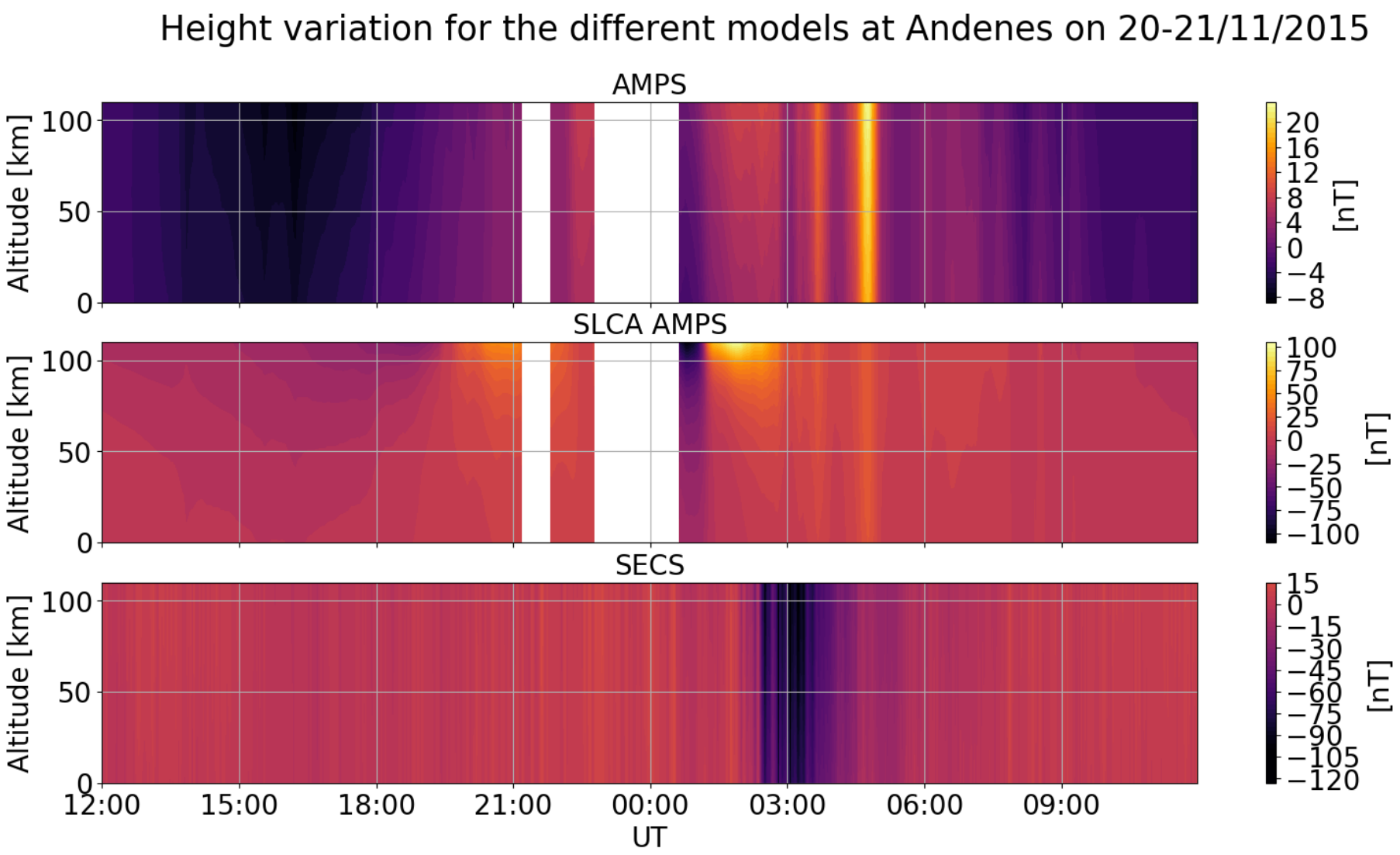

Fig. 4.9.: Altitude variation in total magnetic field perturbations from 0 to 90 km using AMPS, SLCA and SECS outputs over Andenes on 20-21 November 2015

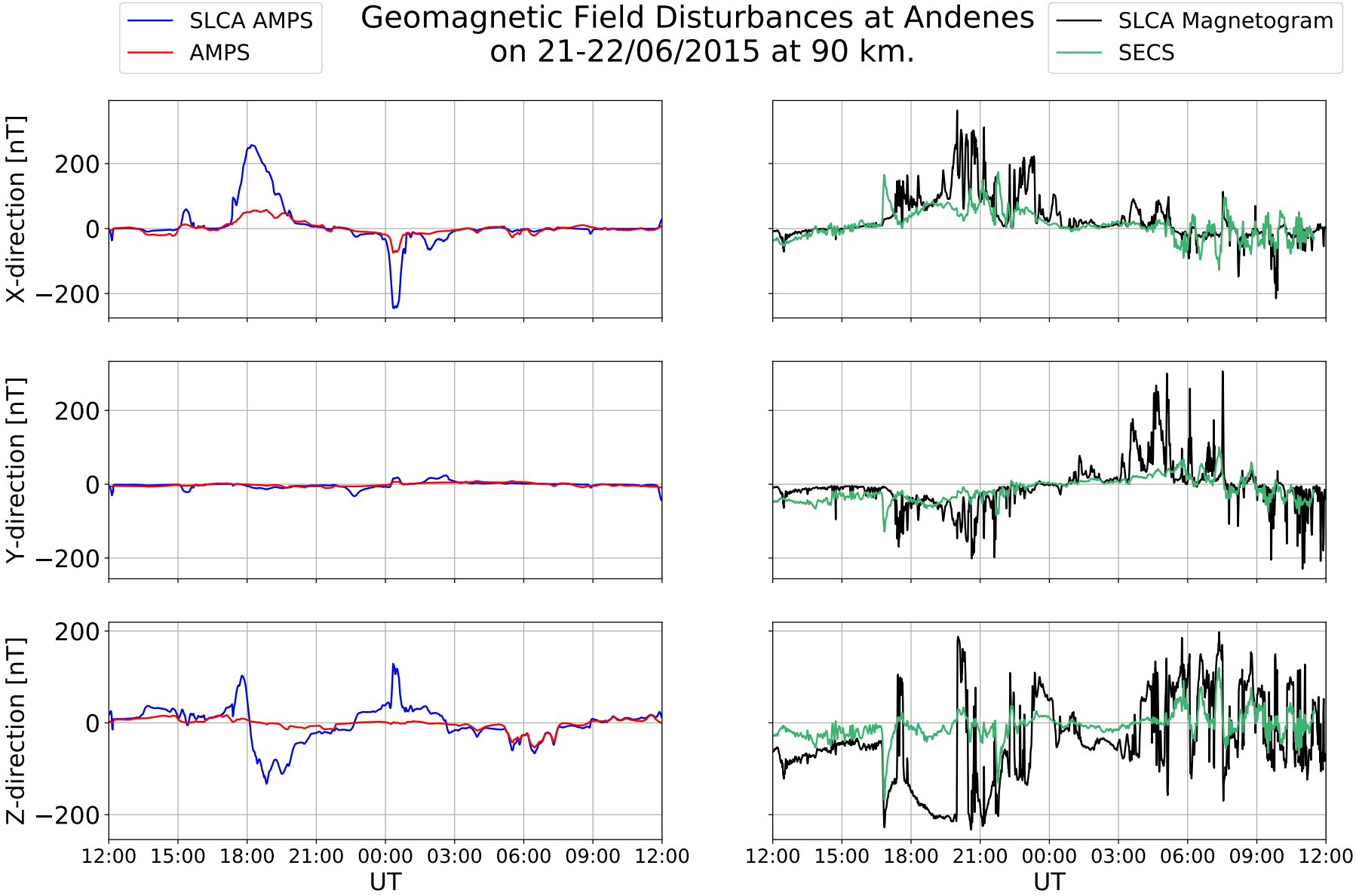

Fig. 4.10.: Modelled magnetic field at 90 km altitude over Andenes on 21-22 June 2015

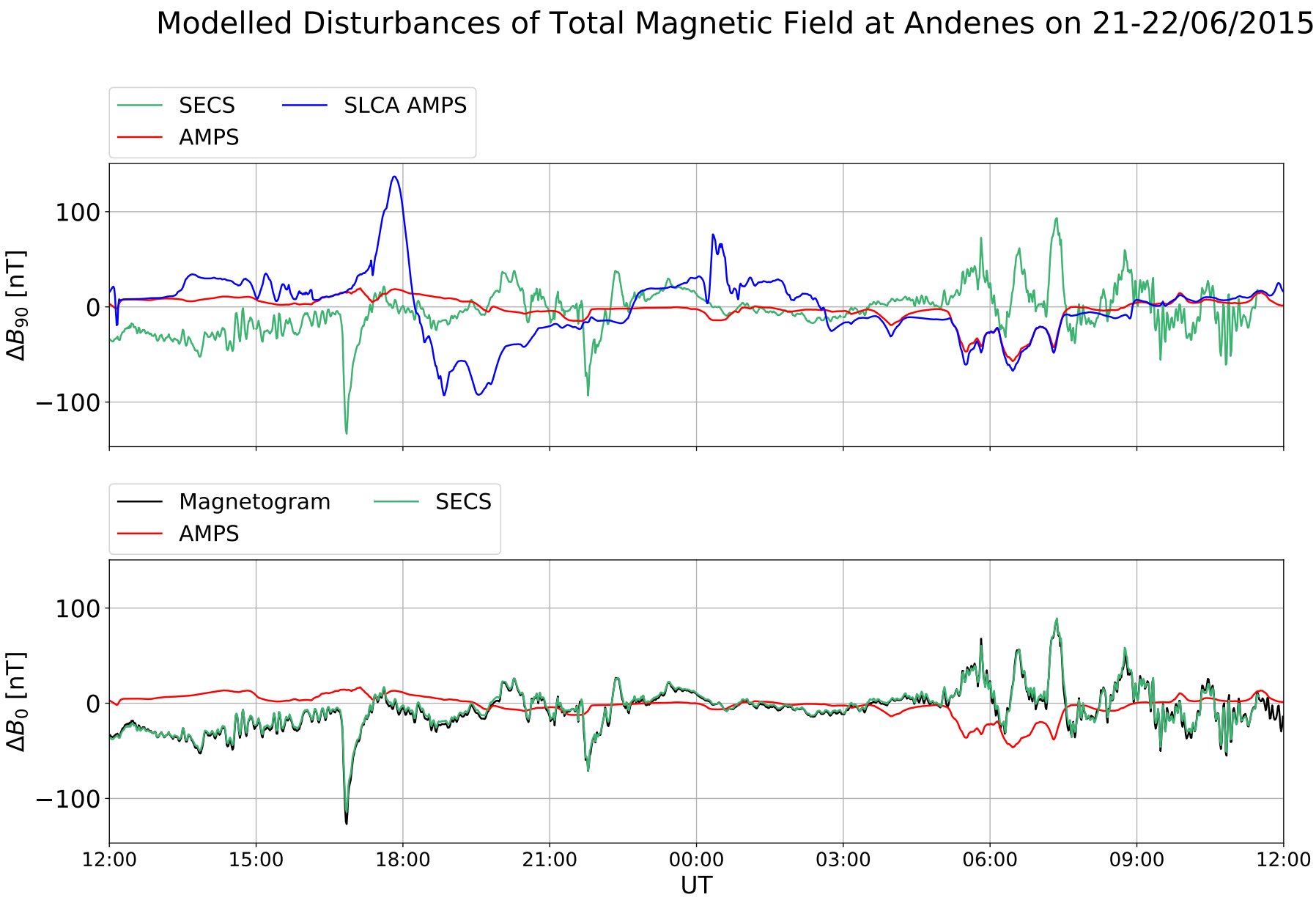

Fig. 4.11.: Total magnetic field perturbations for 0 km and 90 km at Andenes on June 21-22 2015.

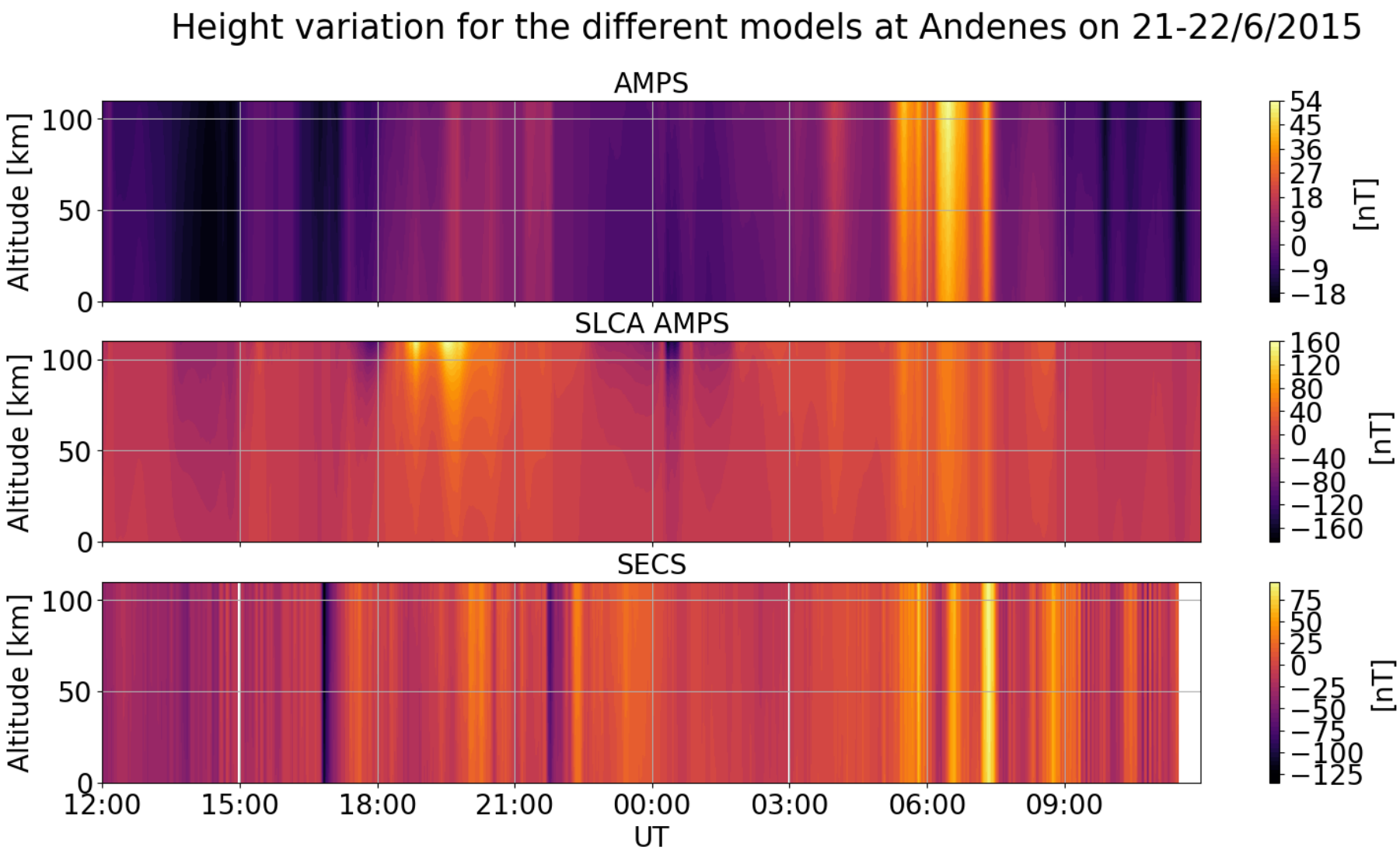

Fig. 4.12.: Altitude variation in total magnetic field perturbations from 0 to 90 km using AMPS, SLCA and SECS outputs over Andenes on 21-22 June 2015.

Discussion

5

5.1 Modelled Magnetic Field Disturbances Compared to Measurements

Initial inspection of the goodness of fit for the two models shows it is clear that the SECS model performs close to a perfect job at reproducing the measured data for all the days, this is supported by the method used to find the best SVD-parameter as well. Here the total RMSE for $SVD_{parameter} = 0.021$ was only 57 nT when comparing the SECS-model output with the magnetometer data from the stations Kiruna, Jäkvik and Kilpisjärvi for June 21-22 2015. The strong performance of the SECS model is supported by the results from Pulkkinen et al. (2003a) and Weygand et al. (2011).

Due to the strong result of the SECS model it is found quite easily that the model work quite well for this type of comparison. Here we looked at time series of geomagnetic field perturbations for a single station, which is part of a fairly dens magnetometer ground station network. It is understood the the model performance may not be as strong at other locations with a sparser surrounding station network. This statement is supported in Fig. 3.2, which was used to find the best SVD-parameter for the stations used in the model. In the process of finding the best SVD-parameter a set of stations including Jan Mayen were considered. A set not including Jan Mayen were also considered, since the station is very far away from the other stations. In the figure it can be seen that including Jan Mayen or not will influence the performance of the model, depending on which SVD-parameter is chosen. This suggest that spatial distribution of the measurements used in the SECS model influences the model performance. Investigation of the spatial resolution in relation to the density of magnetometer stations could be a topic for future work.

The SECS model does not take into account the contribution from geomagnetical induced currents in the ground, and it can be seen that the output lines up perfectly with the non-adjusted magnetometer data. However, in Pulkkinen et al. (2003b) they apply a method where they introduce a layer of spherical elementary currents below the surface to account for the induced geomagnetic field. By applying this technique it would be possible to directly compare the SECS model with the AMPS model, since the AMPS model neglect the internal induced field in its calculations.

In this thesis the outputs from the AMPS *get_B_ground*-function is compared to the adjusted magnetometer data, and there should, in theory, be a good match between the two graphs for all the components. However, as already mentioned in section 4, this is not the case. The reasons for the mismatch is the main focus of the following discussion for the ground comparison.

One potential reason for the bad fit can be that AMPS neglects the internal induced field contributions in the ground potential in Eq. (2.15). This means that the associated divergence free current function in Eq. (2.21) also have no contribution from induced currents and this, of course, affects the model output. The current function on the ground is used when finding the relation between the ground coefficients $a^m_{n,e}$, $b^m_{n,e}$ and the coefficient above the ionospheric current sheet h^m_n, g^m_n described in section 2.1, and can therefore lead to another relationship between the two sets of coefficients.

The method described in section 2.1 for finding the relation between the two sets of spherical harmonics coefficient might be too simple, and may lead to an erroneous result. The AMPS model uses the Spherical Harmonics Analysis (SHA) approach and considers a full sphere for its current system. This means it can use satellite magnetic field data to derive the coefficients. A Spherical Cap Harmonics Analysis (SCHA) (Haines, 1985) uses only a part of the sphere given by an angle β and with this approach magnetometer data can be used to find the relevant ground coefficients. If a large enough area with a dens magnetometer network is considered, the SHA and SCHA approach could potentially be compared for a smaller area within the original area. The entire area cannot be used, because it is important to take into account the boundary conditions of the SCHA. This approach might be able to confirm the relation (Eq. (2.22) and Eq. (2.23)) between ground and space spherical harmonics coefficient for the SHA.

The main reason for the deviation between the adjusted magnetometer data and the AMPS *get_B_ground*-function is considered to be that AMPS does not incorporate perturbations which are related to night side magnetotail phenomena, like substorms. This was already expected due to the nature of the model. Fig. 4.2 is a good example that AMPS seem to model effects that are directly driven by the solar energy input (Rostoker et al., 1988), as opposed to where energy will be loaded into the magnetosphere for a time before the energy is unloaded into the ionosphere. In this particular figure there is a couple of hours of time delay between the depression peak in the AMPS graph to when the substorm occurs in the ground measurements. A possibility is that energy has been gathering in the magnetotail for some time before a reconnection occurs, and thus a time delay is seen from when the solar wind hits the magnetosphere until the small substorm occurs. The early increase in the X and Z-component in Fig. A.1 could also be

due to AMPS only producing solar wind directly driven disturbances. Of course another potential reason for the earlier onset of the substorm in Fig. 4.2 might be due to the large gap of OMNI data used as input into the *get_B_ground*-function occurring after 21:00 UT (see Fig B.10, Appendix B).

In general the AMPS model produces ground perturbations with lower amplitudes than that of the adjusted magnetometer data, with the exception of Fig. A.5 where a larger disturbance going on between 21:00 and 00:00 UT can be seen. This might be a situation where the equivalent currents in the model are positioned at other latitudes than what the ionospheric horizontal current system is. The auroral electrojets positions, as well as their width, will affect the intensity of the ground perturbations, which is also true for the distance between the magnetometer station and the center of the electrojets (Kamide and Brekke, 1975).

An example of the importance of the placement of the equivalent current system in model can be seen in Fig. 4.3. Tab. 4.1 shows that the AMPS model Z-component is correlated with a factor of $c_{0,AMPS} = -0.49$ with the measured Z-component, and the reason for this negative correlation is believed to be that the AMPS place the electrojets on the wrong side of the magnetometer. Thus the perturbations might still be solar wind driven and can be modelled by AMPS, but the perturbation will have an incorrect orientation in the Z-component from the measurements at Andenes. This is probably the reason why in Fig. 4.3 negatively correlated disturbances in the Z-component can be seen outside the time period 18:00-04:00 UT, while inside this period there are almost no disturbances modelled by AMPS.

Lastly, in Weigel et al. (2002) they conclude that no single coupling function between the solar wind and ground magnetometer data could be given for all geographical locations. They found that the solar wind velocity was highly coupled to the time derivative of the north magnetic field component at high latitudes, i.e. polar cap stations, while the IMF B_z component had on average little influence on the prediction efficiency. For stations located under the auroral zone, like Andenes, they found a strong coupling between the time derivative of the northward geomagnetic component and the IMF B_z component when the stations was located in the sector after local midnight. In the day side sector solar wind velocity had the strongest influence on the prediction efficiency for stations at auroral latitudes. It is not directly clear to whether or not AMPS includes this effect, but by looking at the solar wind input data in Appendix B there appears to be no apparent evidence of this. There is a possibility this effect could be included in the model since AMPS uses the clock angle on its own when calculating the spherical harmonics coefficients in section 2.1. However, the effect is not taken

into account when AMPS uses Newell's coupling function ϵ (Newell et al., 2007), since ϵ is both a function of solar wind velocity and IMF B_z and B_y components.

From the arguments given in this section it is believed that the poor correlation between AMPS and ground based measurements should be further studied. The AMPS model was limited by the time period of the days and the location in this study, therefore the AMPS model might perform well for other spatial and temporal configurations.

5.2 Altitude Variations in the Modelled Magnetic Field

Due to the lack of in situ measurements of the geomagnetic field at altitudes below the lower ionosphere it is impossible to say whether or not any of the models provides an accurate description of the geomagnetic field variations at these altitudes. It is tempting to say that the SECS model perform well at these altitudes, because of its good performance on the ground. However, part of what is measured by ground magnetometers are geomagnetic contributions from induced ground currents, and the SECS model considered in this thesis does not separate these contributions from measurements. This results in that the altitude variations produced by the SECS model includes the ground currents contribution on all heights, while they in reality should decrease with height. It was assumed in section 3.2 that the contributions from the induced ground currents will decrease with height, therefore the results from the SECS model are limited by this assumption. The method of removing the contributions from geomagnetically induced currents in the ground described in section 3.2 were considered to be inadequate due to the large topographical differences for the locations of the magnetometer stations.

The AMPS model performed poorly in the comparison on the ground, and therefore indicates that it might not be a useful model for geomagnetic field perturbations at 90 km. However, the AMPS model actually use space measurements to derive the spherical harmonics coefficients, granted the measurements are from altitudes above 300 km. Nevertheless, the use of space measurements makes it seem reasonable that AMPS should be able to model the magnetic field perturbations at 90 km altitude. In the discussion about the ground comparison it was concluded that looking at the night side disturbances under the auroral oval would put the AMPS model at a disadvantage. This was because AMPS does not consider influences from magnetotail phenomena when modelling magnetic disturbances on ground, which is also true for higher altitudes.

Since the AMPS model is limited in that it does not take into account magnetotail phenomena and only model directly driven perturbations it cannot be expected that the model would perform well for disturbances around magnetic midnight. However, disturbances occurring around dusk and dawn are often directly driven by the solar wind driving the eastward and westward electrojets, i.e. through plasma convection, and AMPS should in theory be able to reproduce these disturbances. The AMPS model outputs from the ground comparison in Fig. A.2 and Fig. 4.2 support this theory, however in other results like Fig. A.3 and Fig. A.5 this cannot be seen. Since there is not a uniform support of this in the ground comparison, it is unreasonable to claim that the AMPS model performs accurate during dusk and dawn at higher altitudes from the results in this thesis.

However, as can be seen in Fig. 4.5, Fig. 4.8 and Fig. 4.11 the modelled magnetic disturbances at 90 km from SECS and AMPS appears to mainly be a scaled version of the ground disturbances, i.e. the amplitudes of the disturbances have just been increased. This is not true for the SLCA AMPS output as we see in the figures, where the Z-component have a much higher variability at 90 km compared to the AMPS 90 km output, which can be seen in Fig. 4.4, Fig. 4.7 and Fig. 4.10. This means that perhaps the simple line current approximation might be more suitable for situations where you have a strong discrete current, for instance a substorm current (Akasofu, 2013), than the advanced AMPS model. If a strong discrete current were to occur in the E-layer the advanced SECS model would transform this discrete current into a part of the current sheet in the model. If the discrete current were strong enough to be measured by satellites as well, the AMPS model would indirectly transform these currents into current sheets through the spherical harmonics coefficient. This would result in little change in all the components in the geomagnetic field, and the field would be close to constant for all heights below the sheet due to the nature of a current sheet. The SLCA method however would allow for a larger change in the components of the geomagnetic field for different height, especially since the direction and size of the line current would be determined from the ground measurements.

A surprising result is that in Fig. 4.5 SLCA AMPS appears correlated with the SECS model at 90 km for the time period 21:00 to 02:30 UT, but negatively correlated outside of this period. There are periods of negative correlation in Fig. 4.11 as well. It is believed that ΔZ_{SLCA} generally appears with larger variations with increasing altitudes, and therefore its importance will be larger when looking at $\Delta B_{tot,SLCA,90}$ than what the ΔZ_{AMPS} have on $\Delta B_{tot,AMPS,90}$, simply because the ambient field is close to vertical. Comparing the Z-component from AMPS 90 km in Fig. 4.10 with the Z-component from AMPS 0 km in Fig. 4.3 it can be seen that the two outputs are almost identical. Since generally a stronger

disturbances is seen in the measured Z-component than in $\Delta Z_{AMPS,0}$ it makes us question whether Eq. (2.26) and its scaling factor $r^{n-1}R_E^{n-1}$ is the best method, i.e. the current sheet approach, for calculating $\Delta Z_{AMPS,h}$ at different altitudes.

Baumjohann (1982) discussed the behaviour of currents associated with auroral electrojets and discrete aurora, like auroral arcs, break-up aurora, westward traveling surges and eastward traveling omega bands, which are present during magnetically active periods. Assuming that the strength and temporal resolution for some of these currents, like currents associated with discrete auroral arcs and eastward traveling omega bands, might not produce magnetic disturbances that are strong enough to be measured at ground, it can also be assumed that some of these disturbances does not appear in the magnetic measurements from satellites at higher altitudes. However, if the currents are strong enough to appear in ground measurements and satellite measurements, both the advanced models would transform the discrete currents into current sheets. Therefore, it is believed that none of the models are able to reproduce contributions from these types of small-scale currents at altitudes closer to 110 km, where equivalent horizontal current lie in all the models. These types of currents might move in a different direction than the background current due to a gradient in the conductivity related to the precipitating electrons (Russell et al., 2016), therefore it is also likely that these types of currents can produce amplified or decreased magnetic variations at 90 km that would differ from what is seen in the related ground magnetic disturbances.

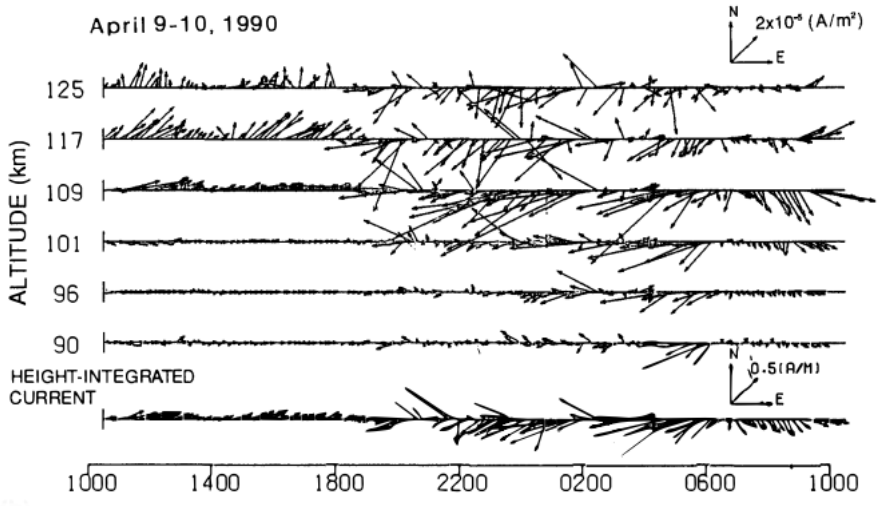

Fig. 5.1.: Current density vectors in A/m^2 observed at six different heights in the E-region by EISCAT Tromsø on April 9-10 1990. The X-axis is time in magnetic local time. Figure borrowed from Sato et al. (1994).

Fig. 5.1 is from Sato et al. (1994) where they studied the altitude profiles of ionospheric currents and conductivities using EISCAT data from 1990. From the figure it can be assumed that geomagnetic field variations at 90 km will be influenced more by the altitude of the ionospheric currents and the sizes of the currents, than what the geomagnetic variations on the ground would be. The figure also support the argument that there might be small-scale currents going in different direction than the large-scale currents which produces magnetic disturbances at 90 km and these might not be strong enough to be measured on the ground. Particularly, if considering the time period between 18:00 MLT and 02:00 MLT, there are several currents moving in different directions at the different heights, which is believed to influence the magnetic perturbations more at 90 km than at 0 km.

From the arguments on how proximity to the current influence magnetic field perturbations and discrete currents effect on magnetic field perturbations, it seems unlikely that the magnetic perturbations at 90 km would appear as a simple scaling of the ground magnetic perturbations. Especially for periods with large geomagnetic activity, for instance as can be seen Fig. 4.5, this appears unlikely. However, for less active periods, like what can be seen Fig. A.20, it is more reasonable to assume that the geomagnetic field variations would be more constant, like it could be expected from a magnetic field due to an infinitely large sheet current.

Rocket Borne Magnetometer Measurement Comparison

In the following section the results from an airborne magnetometer discussed in Burrows et al. (1971) is compared with the model results of $\Delta B_{h,model}$ for different altitudes. This is done as an attempt to verify any of the model outputs despite the lack of in situ measurements from the MOM-campaign March 2019. Burrows et al. (1971) discussed the results from the airborne magnetometers on two Nike-Tomahawk along with ground magnetometer data. In addition to the magnetic observations they used optical observation of aurora borealis occurring during the flight as well. Figure 6 in Burrows et al. (1971) is "... an attempt to represent, in a single two-dimensional diagram, the complicated space and time variations of both the auroral morphology... and the rocket magnetometer data...". This figure support the argument in the previous section that geomagnetic field variations are influence by discrete auroral arc currents at E-layer altitudes.
Fig. 5.2 b) shows the ground magnetograms for Fort Churchill on March 23, 1966, which is considered a disturbed magnetic day. A rocket was launched at a time close to the minimum of the negative bay the ΔX-component. Fort Churchill is located at geographic latitude 58.76 °N and longitude 265.91 °E, and the launch

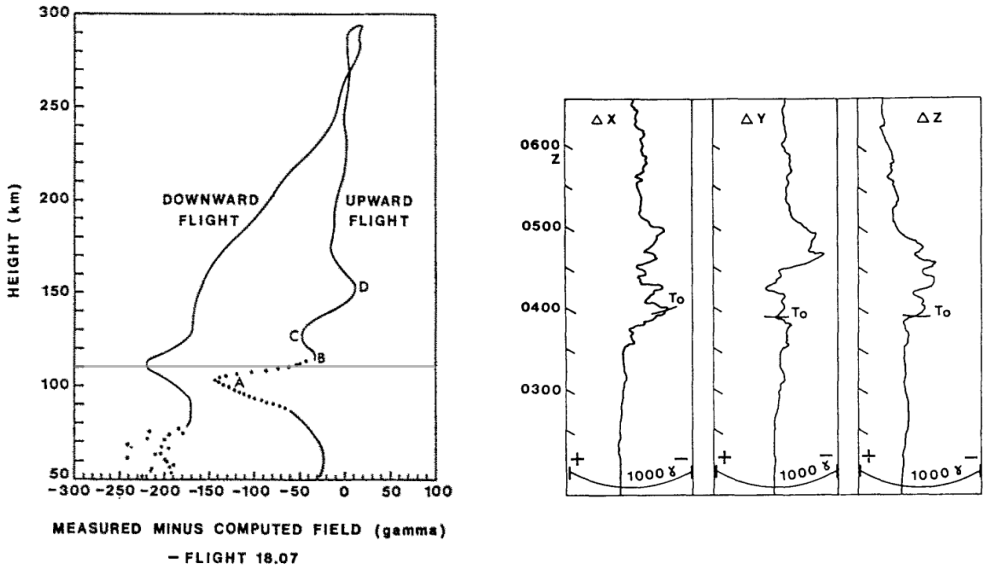

(a) (b)

Fig. 5.2.: a) Variation of total magnetic field with height after subtraction of reference field (Flight 18.07). b) Fort Churchill ground magnetograms (Flight 18.07). Figures borrowed from Burrows et al. (1971).

took place at 04:06:53 UT. This corresponds to 21:07:42 MLT at geomagnetic latitude 70.12 °N. From what can be seen in the magnetogram in Fig. 5.2 b) and the geomagnetic position of the Fort Churchill, the rocket is assumed to be under the westward electrojet during the flight.

To be able to compare the height profile of the geomagnetic total field disturbances with the measurements from the rocket launch, seen in Fig. 5.2 a) under the grey line, we set some criteria on the orientation of the magnetic field based on what could be seen in Fig. 5.2 b) at T_0. Note that Fig. 5.2 a) only show altitudes above 50 km and that the downward flight and upward flight are different. This analysis focuses on the upward flight since that is marked on the magnetogram in Fig. 5.2 b).

During the process it was discovered that the orientation of the magnetic field components had a major impact on the resulting height profiles given by the models. It was therefore decided to present three different points in time instead of a single point. The first point in time was chosen to show a ΔB_{model} height profile with similar shape to what could be seen in Fig. 5.2 a). The second was chosen to show a completely different shape from the previous and the last point in time is taken to be a random sample. It was decided that $\Delta X_0 < -100\,\text{nT}$, ΔY_0 had to be within the range of $\pm 10\,\text{nT}$ and ΔZ_0 needs to be decreasing and negative. These criteria eliminated several of the days used in this comparison

and at the end three points in time for three different dates were chosen: April 22 2017 19:02 UT, April 23 2017 00:23 UT and December 17 2017 02:23 UT.

In Fig.5.3 and Fig. 5.4 it can be seen that both points in time have very different height profiles despite the two points being only hours apart. The first point is from April 22 2017 and the second April 23 2017. This indicates that the orientation of the field on the ground has a large influence on the shape of the profile. At least when using geomagnetic field models to calculate the height profiles. This is true for all the different models, despite AMPS having the same shape in Fig. 5.3 and Fig. 5.4.

In Burrows et al. (1971) two rockets were launched on March 23 1966 and on April 14 1966. The last rocket only provided measurements between 90 to 280 km on the upwards flight. The two height profiles for the total geomagnetic field variation for the two days, Figure 5 and Figure 9 in the paper, shows different profiles. In Burrows et al. (1971) they concluded that the discrepancy between the two figures are most likely due to choosing an incorrect baseline for April 14 1966. However, since the height profiles from the three models for three different points in time all show different orientations, we think that the discrepancy seen in Burrows et al. (1971) are due to differences in the orientation of the geomagnetic field for the launch time, see Figure 3 and Figure 7 in Burrows et al. (1971).

The above discussion indicates that using historic rocket measurements as a technique to verify any of the model outputs should not be done underneath the auroral zone, despite the SECS altitude profile in Fig. 5.3 is of similar shape to what can be seen in Fig. 5.2 a). Whether or not the advanced models give an accurate description on the height profile for ΔB_{model} cannot be concluded from the work done in this thesis. However, when looking at all the altitude profiles in Fig. 5.3, Fig. 5.4 and Fig. 5.5 it seems safe to assume that caution is needed when using any of the advanced models to model geomagnetic disturbances close to the model's equivalent current height. It is especially the relatively weak change, seen in the advanced models, in the field at heights from 90 km to 110 km that is of concern. In Fig. 5.2 a) the rocket most likely penetrated the westward electrojet on the upward flight, judging from both the magnetogram and from the large negative change in measured field. This argument indicates that Fig. 5.3 which is taken at a time where the Andenes magnetometer station would be underneath the westward electrojet, but there is less than a 10 nT difference in the modelled field from 80 km to 110 km in the advanced models. This concern is supported in Figure 5 in Cahill et al. (1980) where a rocket measured the magnetic field as it went through the eastward electrojet. The figure shows a similar large, but positive, change in the measured field as in Burrows et al. (1971).

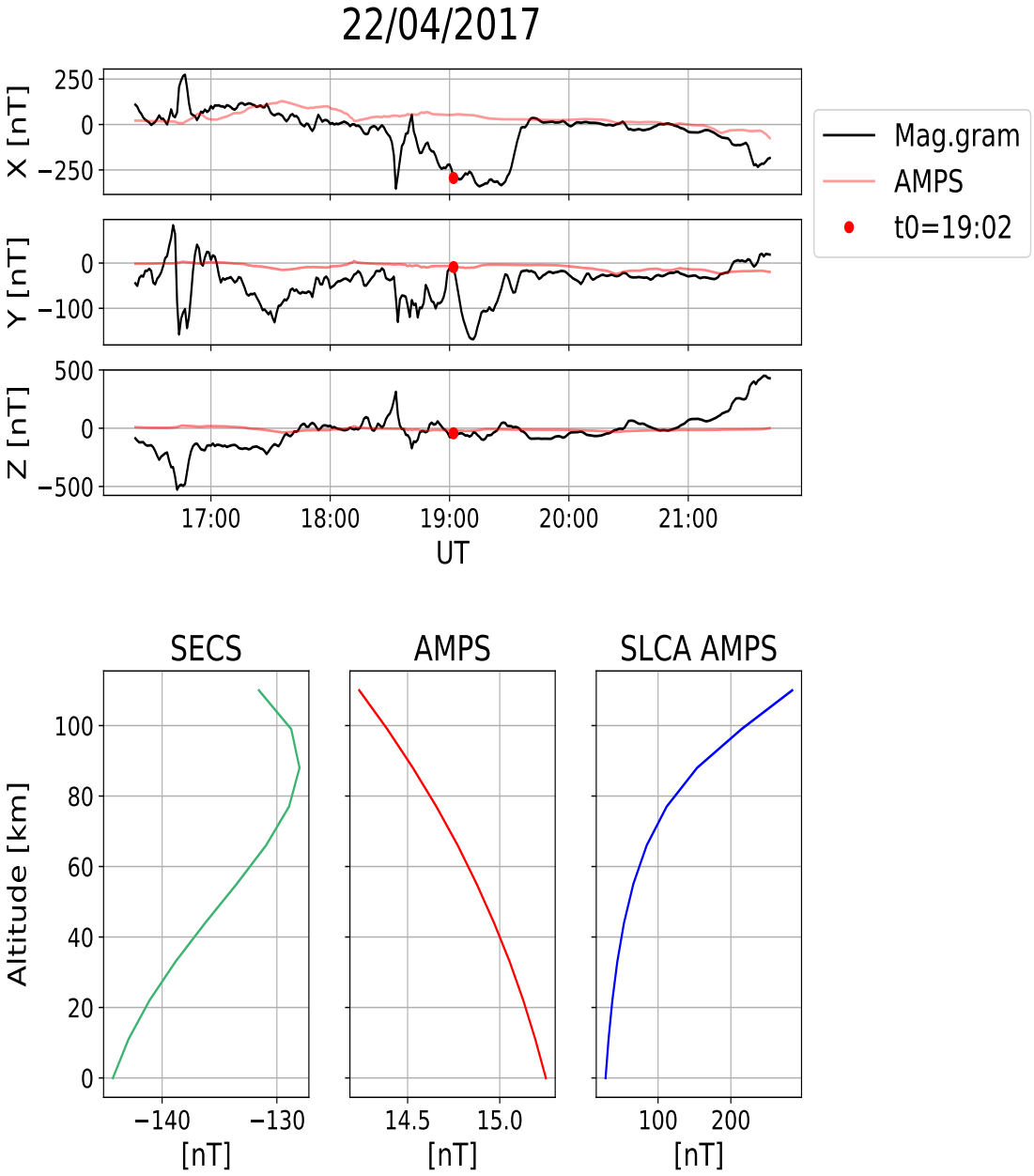

Fig. 5.3.: Total geomagnetic field perturbation height profiles plotted for 19:02 UT on April 22 2017. The full time resolution for that day can be seen in Fig. 4.6.

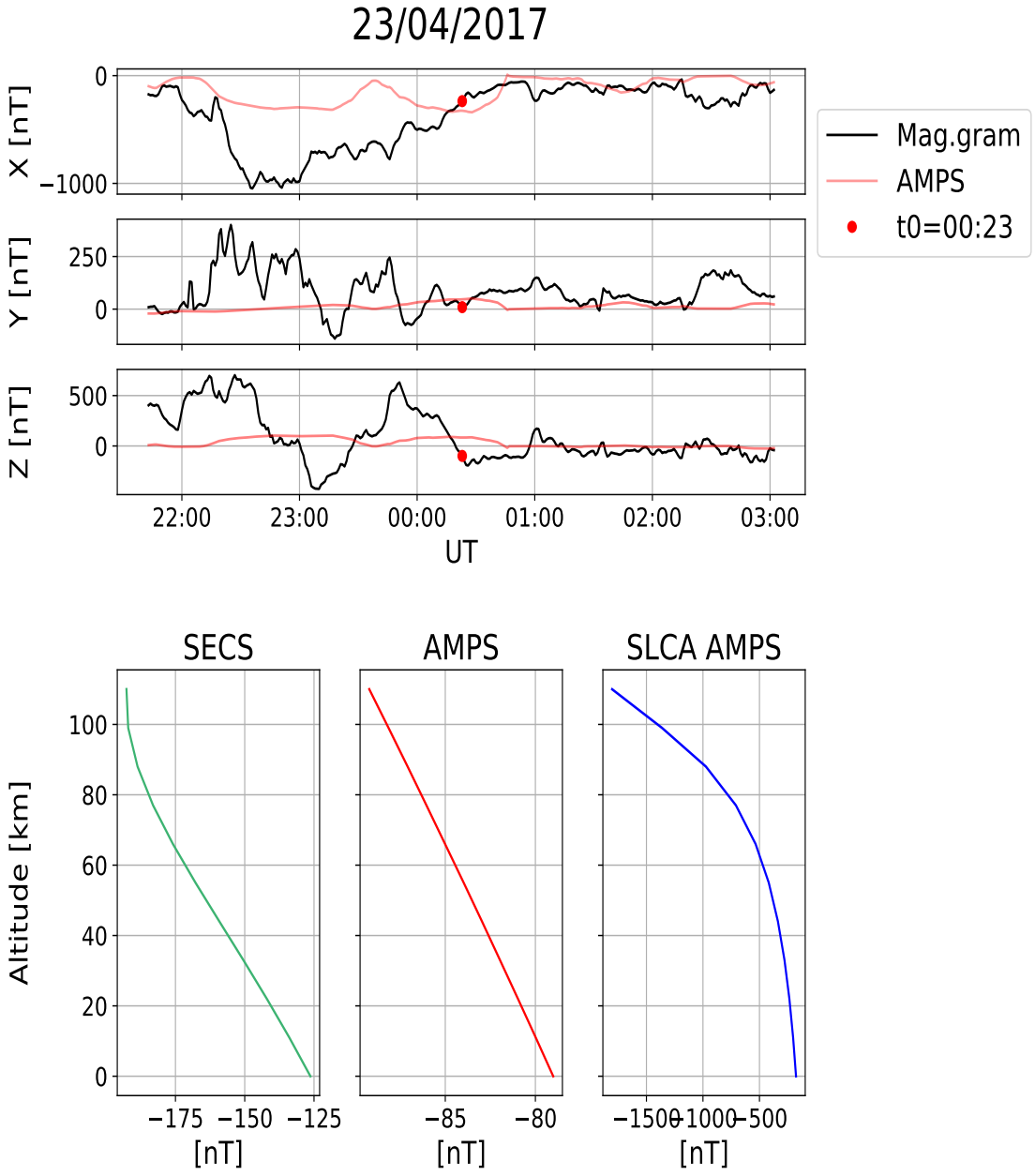

Fig. 5.4.: Total geomagnetic field perturbation height profiles plotted for 00:23 UT on April 23 2017. The full time resolution for that day can be seen in Fig. 4.6.

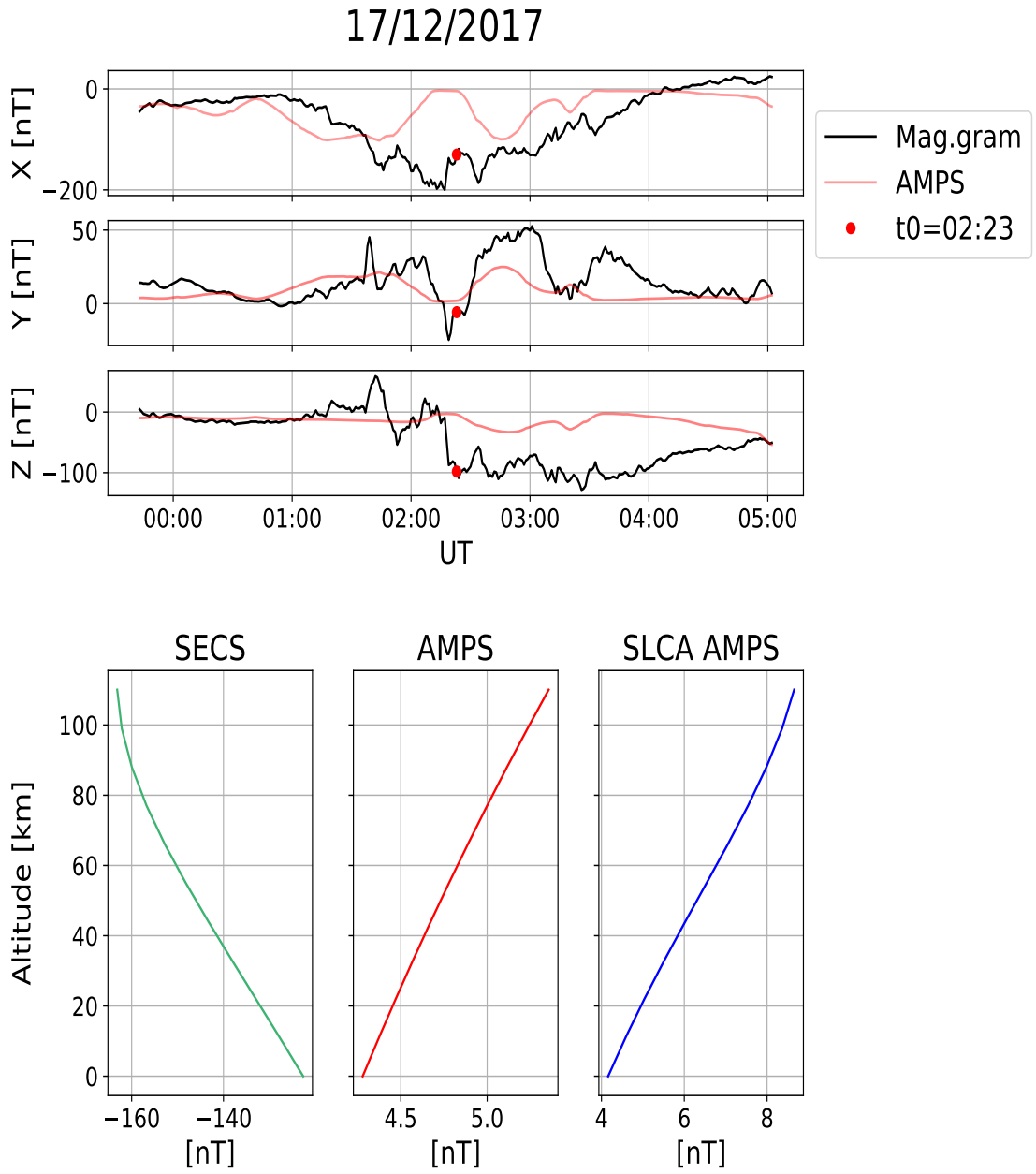

Fig. 5.5.: Total geomagnetic field perturbation height profiles plotted for 02:23 UT on December 17 2017. The full time resolution for that day can be seen in Fig. A.24.

Conclusion

6

Modelled geomagnetic disturbances have been compared with ground magnetometer data from Andenes for ten days with different magnetic activity levels as a mean to assess the model performance from two different models. The Spherical Elementary Currents System (SECS) model and the Average Magnetic field and Polar current System (AMPS) model were advanced models using a large set of measured ground magnetic data and terrestrial-solar wind parameters as inputs, respectively.

A study on how the geomagnetic disturbances changed with altitude were included as well. A third method called the Simple line Current Approximation (SLCA) were added in this study to provide a simple method of calculating the magnetic disturbances in the mesosphere. Originally the modelled geomagnetic disturbances at different altitudes were intended to be compared with preliminary measurements of the total geomagnetic scalar field from the MOM-campaign that took place March 2019. However due to set backs in the preparation of the Sodium-LIDAR at ALOMAR no experiments were performed before the atmosphere became too illuminated by the sun, and there will not be a new campaign before winter 2019/2020. The lack of in situ measurements to verify the model performances were compensated by a comparison of the modelled magnetic field disturbances with rocket magnetometer data studied in Burrows et al. (1971).

In the ground comparison it was concluded that the SECS model is clearly the better out of the two advanced models for modelling time series ground perturbations of the magnetic field, especially in an area with a good coverage of magnetometer stations. Access to data and the global, spatial distribution of the magnetometer network appears to be the most significant limitations of the SECS model. If the relevant research topic demands separation of contributions from geomagnetical induced currents and external current then the SECS model used here is not suitable. A solution is to adapt the model with the method discussed in Pulkkinen et al. (2003b).

The AMPS *get_B_ground*-function have been used for modelling the magnetic perturbations at altitudes from 0 km to 90 km. From the results it has been concluded that the AMPS model is not very suitable to use for time series of geomagnetic ground variations on the night side in the auroral zone. Substorm activity and other magnetotail phenomena are considered to be the major reason

for the poor performance of the AMPS model. Since AMPS is an empirical model that uses solar wind parameter inputs it would not be able to produce disturbances like substorms and geomagnetic impulses, which was already understood before the comparison. However, some results like Fig. A.6, which is considered a low magnetic activity day, shows a poor goodness of fit between the model outputs and the adjusted magnetometer data, which implies that the AMPS model is not suitable for modelling the geomagnetic field variations at altitudes beneath the lower ionosphere at auroral latitudes.

In theory, the method of deriving the magnetic ground components described in section 2.1 should be suitable for solar wind driven disturbances. This seem to be the case in Fig. A.2, but the modelled perturbations amplitudes are still lower than the adjusted measurements. The AMPS model's placement of the equivalent horizontal currents is considered to be the reason for the negative correlation seen in sometimes in $\Delta Z_{AMPS,0}$. The incorrect current placement in AMPS might also be the reason behind the low disturbance amplitudes. The model might perform better when studying magnetic fluctuations in the polar cap region on the dayside, where the fluctuations are directly driven by solar wind conditions. However, magnetic disturbances in the dusk and dawn sector under the auroral zone are often directly driven by the solar wind through the auroral electrojets. Yet, no clear indication that the model performs better for these times are found in the results.

The modelled scalar geomagnetic fields from AMPS, SECS and the SLCA at different altitudes were originally intended to be verified by in situ measurements from the MOM-campaign. However, as stated in the beginning of this section, there were no measurements obtained during the campaign. Thus, it cannot be concluded whether or not any of the models provide an accurate description of the variations in the geomagnetic field at these heights. In section 4 it was seen that the two advanced models produces very different disturbances at 90 km. Even if the SECS model performed better in the ground comparison it is known to not be entirely correct at these altitudes as discussed section 5.2. A preliminary conclusion for the SLCA is that the outputs should only be compared with actual in situ measurements, since there exists a fairly large discrepancy between both AMPS 90 km and SLCA AMPS, as well as between SECS 90 km and SLCA Magnetogram.

Due to lack of in situ measurements results from Burrows et al. (1971) were attempted to be used as a preliminary indication of the model performances. Yet, from the discussion in section 5.2 the method of using historic data from rocket borne magnetometers to verify the model outputs is considered inadequate. This was due to the major influence the ground geomagnetic field orientation had on

the $\Delta B_{h,model}$ height profiles. At least it should not be done in auroral altitudes, where the geomagnetic field fluctuates a lot and is often very disturbed. Both sets of rocket magnetometer data from Burrows et al. (1971) and Cahill et al. (1980) indicates a large gradient in the magnetic height profiles as the rockets proximity to the westward and eastward electrojets decreases. This large gradient cannot be seen in any of the advanced models height profiles. Yet, in Fig. 5.3 and Fig. 5.4 it can be seen in the SLCA AMPS height profile, indicating that in reality the ionospheric current system might be far more complex than a current sheet approximation. This emphasizes the need for a method of measuring the geomagnetic field in the mesosphere.

The main findings are:

1. Of the two advanced models considered the Spherical Elementary Current System model had the best performance, with a perfect fit to the measured ground magnetic field.

2. The AMPS model performed poorly when modelling time series of geomagnetic field variations under the auroral zone. This limitation that was know a priori, but not to what degree, and further investigation at a location more favourable to magnetic disturbances driven by the solar wind is needed before it can be concluded on the accuracy of the model.

3. From the comparison on $\Delta B_{h,model}$ height profiles against rocket magnetometer measurements studied in Burrows et al. (1971) and Cahill et al. (1980), historic rocket measurements of the geomagnetic field variations cannot be used as in situ measurements for the purpose of verifying the model outputs. Thus, no conclusion on the accuracy of the model outputs at altitude $0 < 110$ km can be reached due to lack of in situ measurements at these heights.

4. The description of the ionospheric current system appears too complex to be simply described by a equivalent current sheet system or a simple line current at locations underneath the auroral zone, due to the presence of discrete currents in the E-layer. This means none of the models discussed are suitable to model the magnetic field variations at altitudes close to the current layer.

Future Work

The most important, and obvious, step for this comparison would be to compare the 90 km model outputs with the in situ measurements from the MOM-campaign

at Andenes that will take place autumn/winter 2019/2020. The results from the campaign would allow a more detailed study on the performance of all the three models that have been considered. Hopefully one of them might be good enough to model the geomagnetic field variations in areas where no in situ measurements methods exists.

To be able to properly compare the SECS model with in situ measurements at 90 km the model should be adapted so it can account for geomagnetic induced currents, for instance by the method used in Pulkkinen et al. (2003b). When this is done it might be possible to perform an analysis on the geomagnetic field variations at mesospheric altitudes. Additionally, an analysis investigating to what degree the geomagnetic induced currents contribution to the geomagnetic field decreases with increasing altitude can be done. Subtraction of the quiet level IGRF-value from the measured geomagnetic scalar field at approximately 90 km allows for a immediate comparison with the model outputs when using the method described in section 3.6.

A direct extension of the comparison executed in this thesis would be a statistical approach where the number of days were extended to a full year, or for a more thoroughly comparison, two years. One year could be for a solar minimum comparison and the other year would then be chosen to allow for a solar maximum comparison. This could also include an extension of the simple line current approximation to a current sheet, to see if the output at 90 km provides a better match with any of the two advanced models. A more thoroughly investigation of the model equivalent currents themselves, for both the advanced models, would be favourable. One option is modelling the divergence free currents from both models over a large range of latitudes and longitudes. This could give an indication on whether the underlying theory behind the models are coherent with what is known today on the ionospheric current system.

Taking into account that the AMPS model is believed to be under less than optimal conditions for the type of comparison performed in this thesis we are under the impression that another type of comparison is needed. A dayside comparison of the measured ground magnetic field with the AMPS model outputs is needed, preferably with a magnetometer array that includes polar and mid-latitude stations. This could determine if the AMPS model is limited to certain latitudes. Using a magnetometer array for geomagnetic longitudes $105\pm5°$E would allow the use of polar stations, like NAL, located at geomagnetic latitude 75.25°N

down to mid-latitudes stations, like BRZ, at geomagnetic latitudes 52.30°N, see Fig. 3.1. IMAGE[1] would be a natural data source for this type of study.

[1]The geomagnetic latitudes and longitudes are in reality the corrected geomagnetic latitudes and longitudes taken from `http://space.fmi.fi/image/www/index.php?page=stations` (accessed: May 20, 2019)

Remaining Results

A

In the following appendix the results that were not included in section 4 are presented.

A.1 Results for 0 km

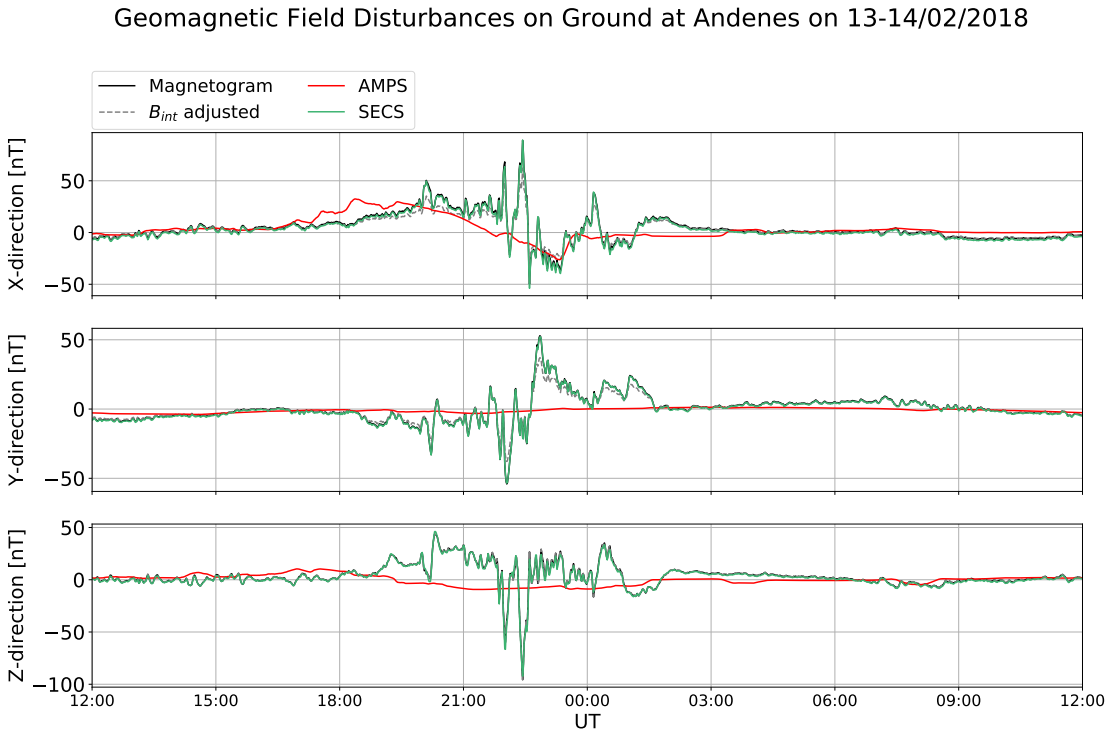

Fig. A.1.: Measured and modelled ground magnetic perturbations at Andenes on February 13-14 2018.

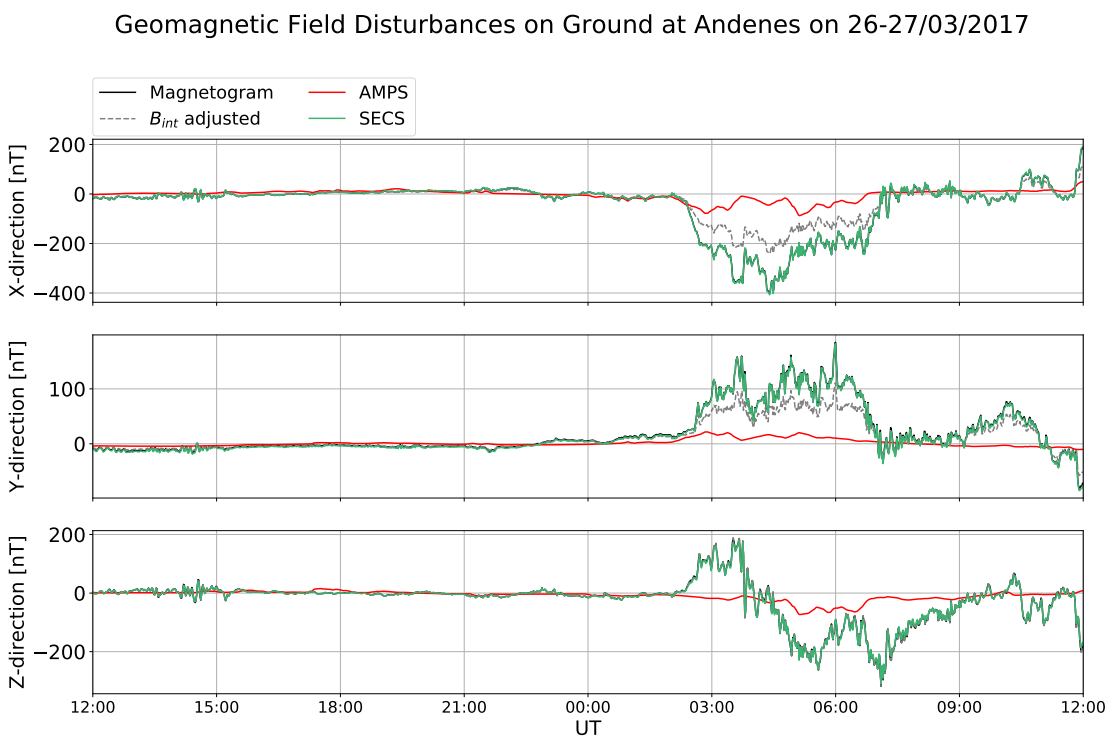

Fig. A.2.: Measured and modelled ground magnetic perturbations at Andenes on March 26-27 2017.

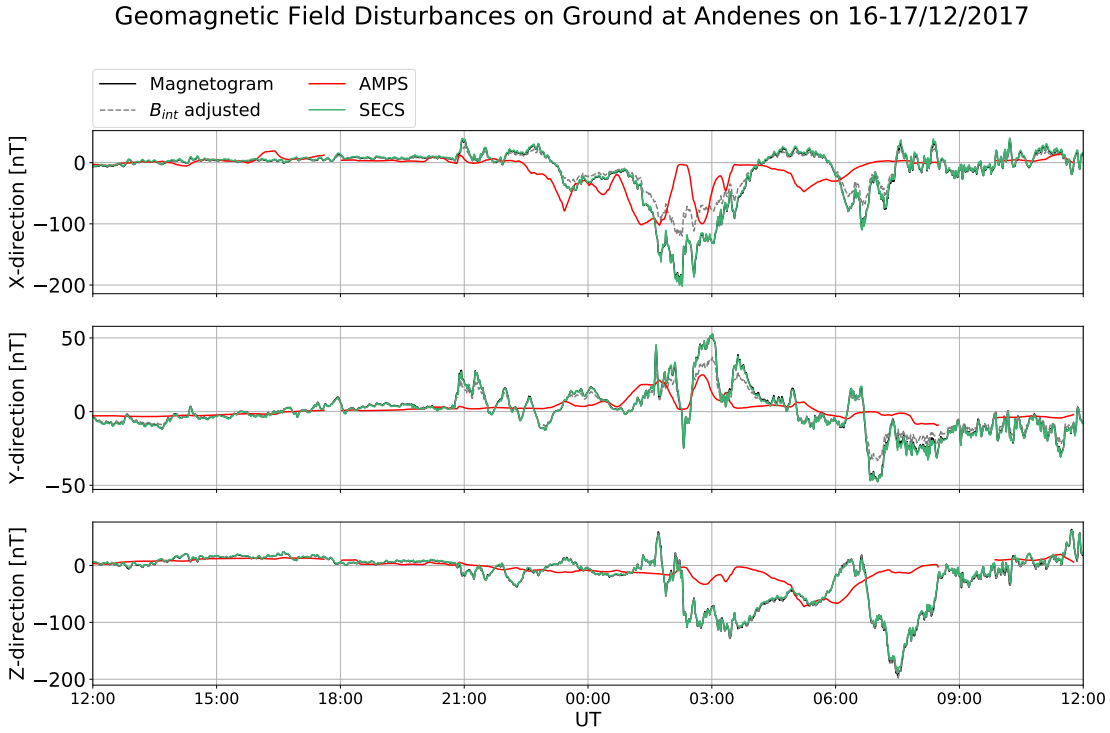

Fig. A.3.: Measured and modelled ground magnetic perturbations at Andenes on December 16-17 2017.

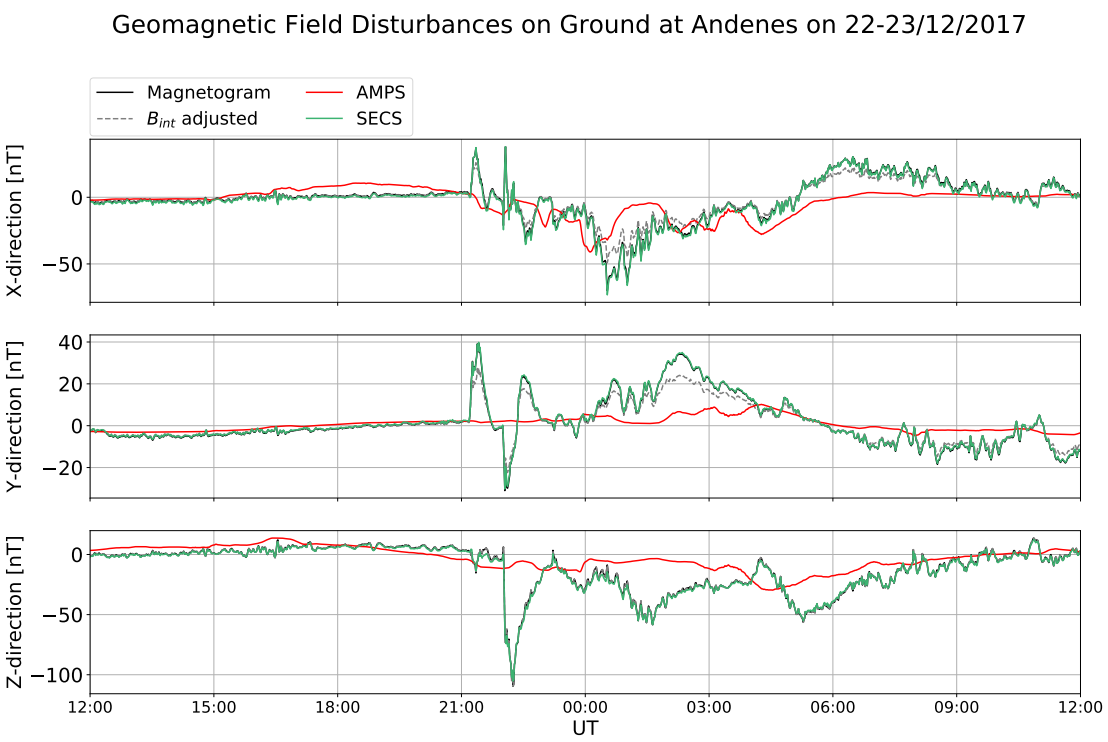

Fig. A.4.: Measured and modelled ground magnetic perturbations at Andenes on December 22-23 2017.

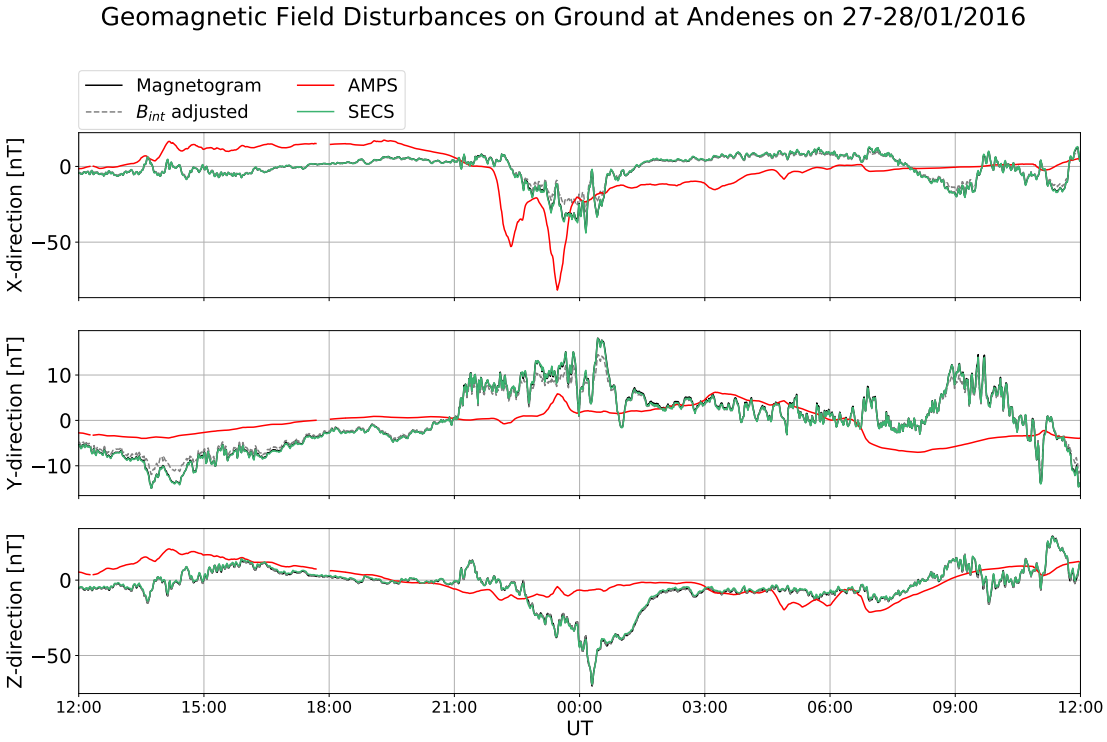

Fig. A.5.: Measured and modelled ground magnetic perturbations at Andenes on January 27-28 2016.

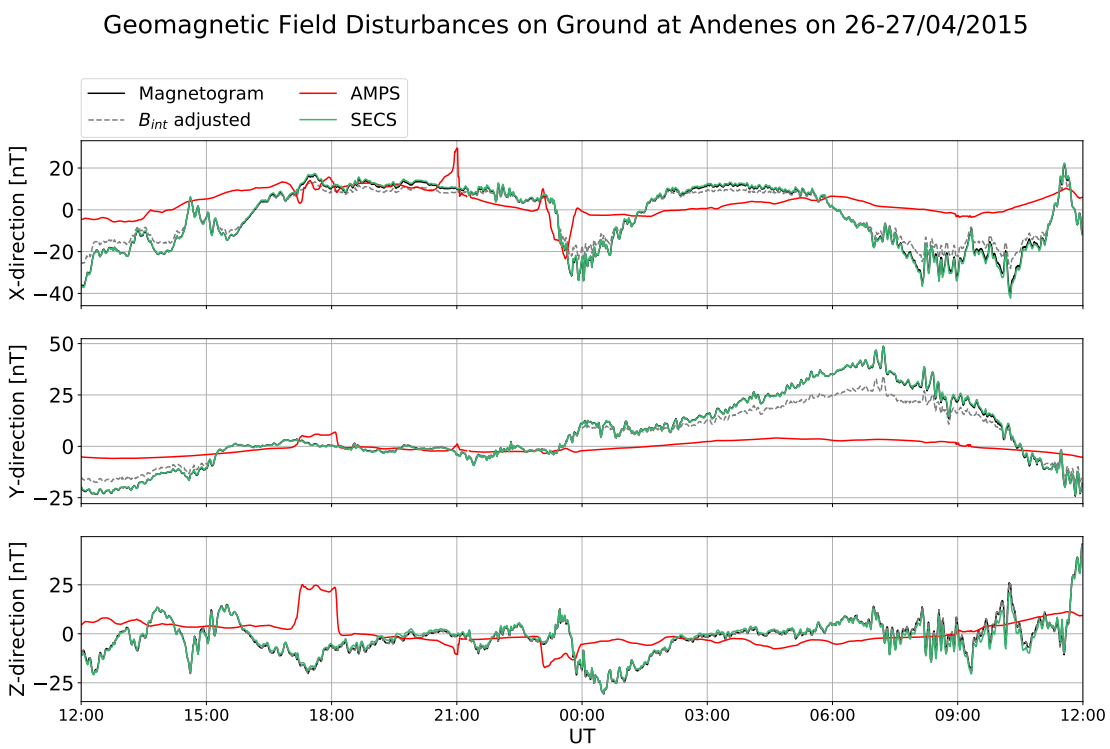

Fig. A.6.: Measured and modelled ground magnetic perturbations at Andenes on April 26-27 2015.

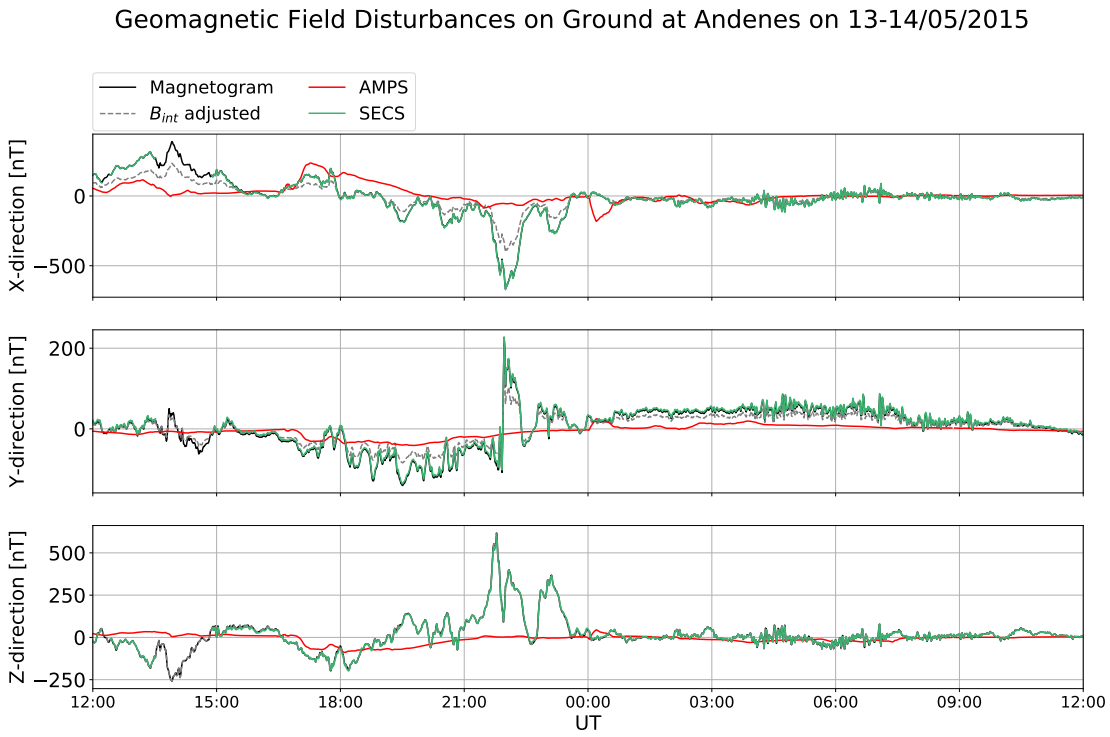

Fig. A.7.: Measured and modelled ground magnetic perturbations at Andenes on May 13-14 2015.

A.2 Results for 90 km

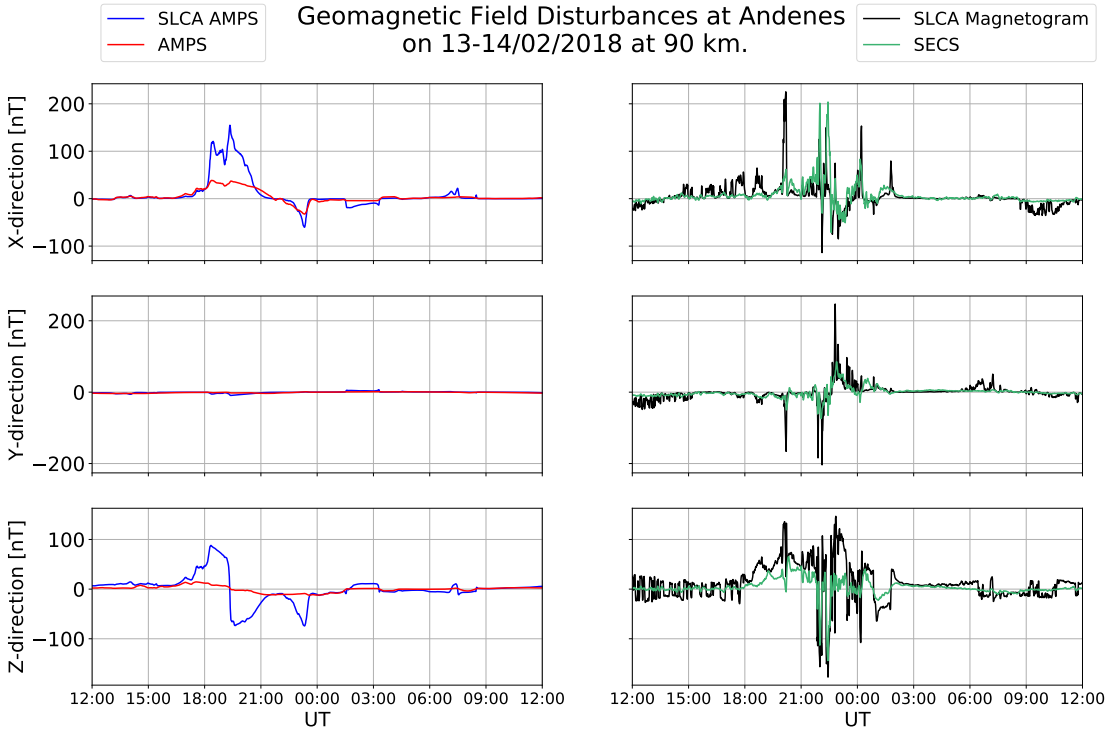

Fig. A.8.: Modelled magnetic field at 90 km altitude over Andenes on February 13-14 2018.

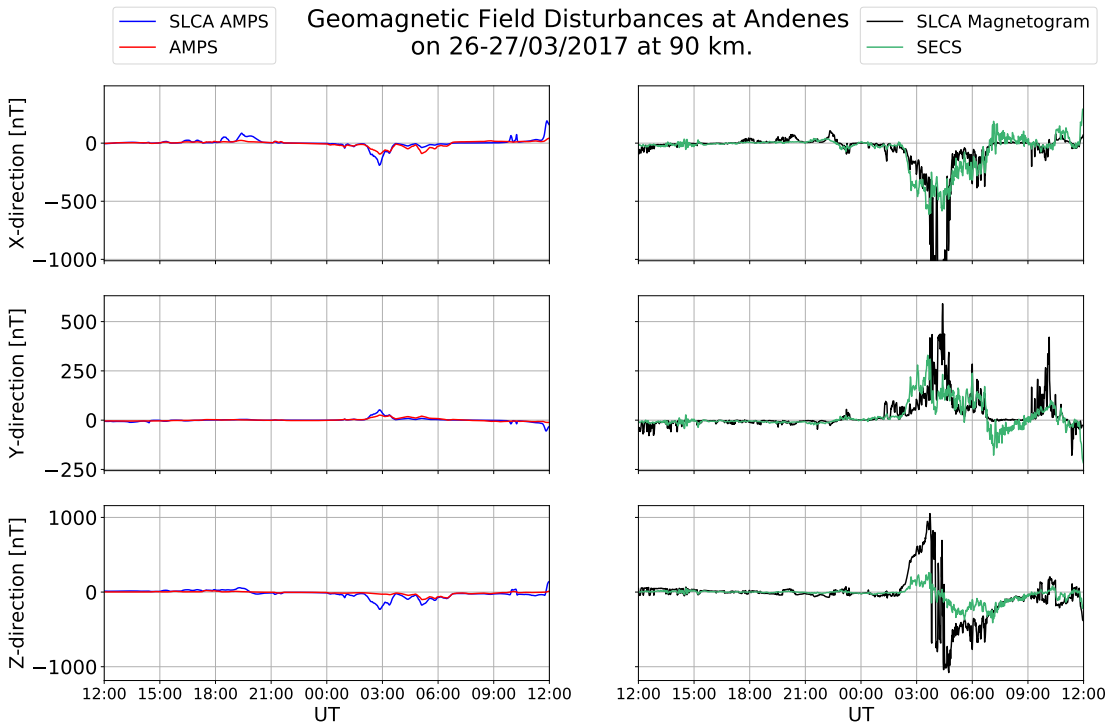

Fig. A.9.: Modelled magnetic field at 90 km altitude over Andenes on March 26-27 2017. The y-limits in this figure has been adjusted.

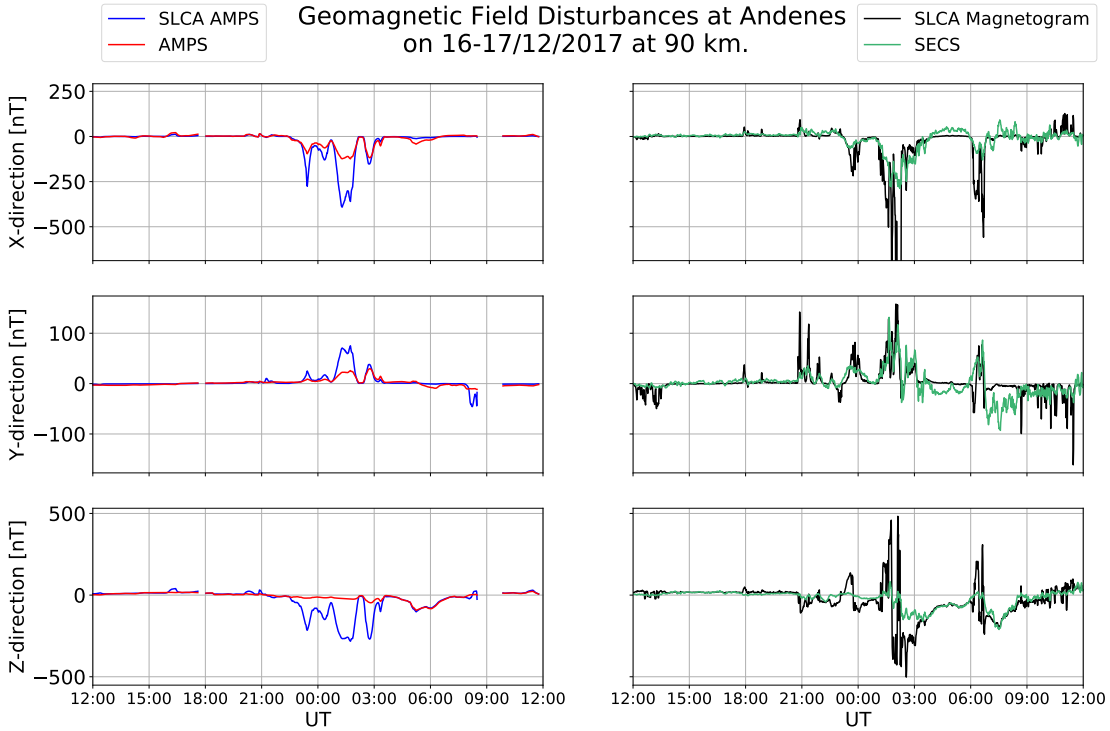

Fig. A.10.: Modelled magnetic field at 90 km altitude over Andenes on December 16-17 2017. The y-limits in this figure has been adjusted.

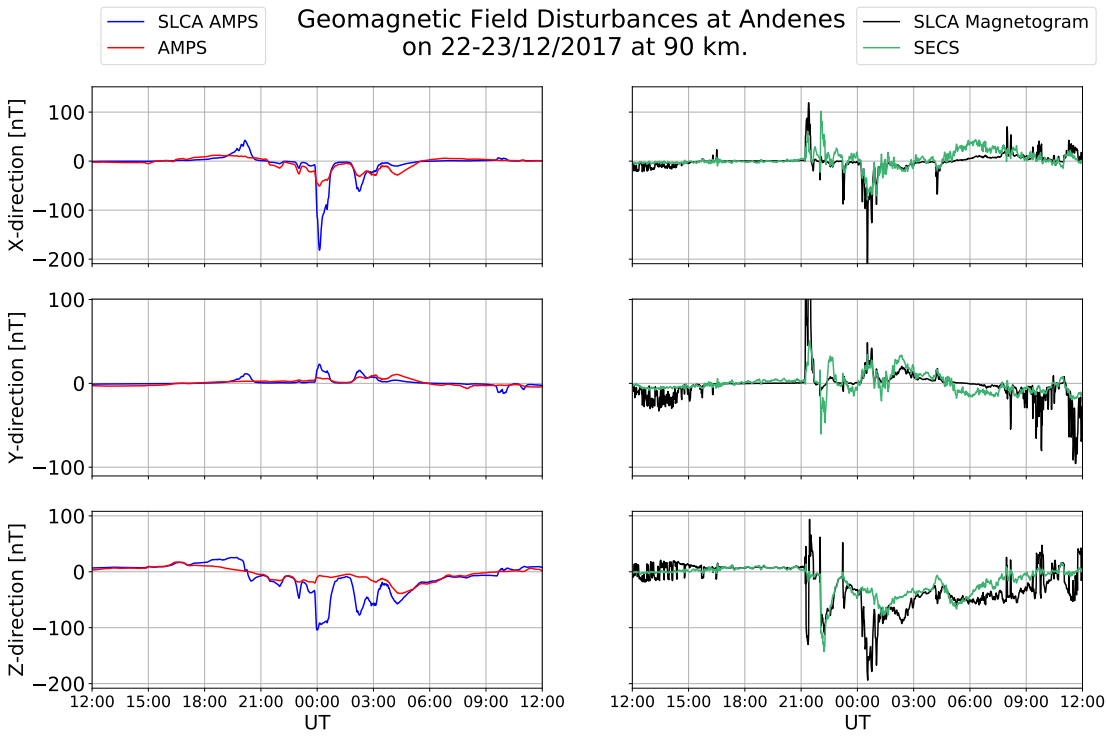

Fig. A.11.: Modelled magnetic field at 90 km altitude over Andenes on December 22-23 2017. The y-limits in this figure has been adjusted.

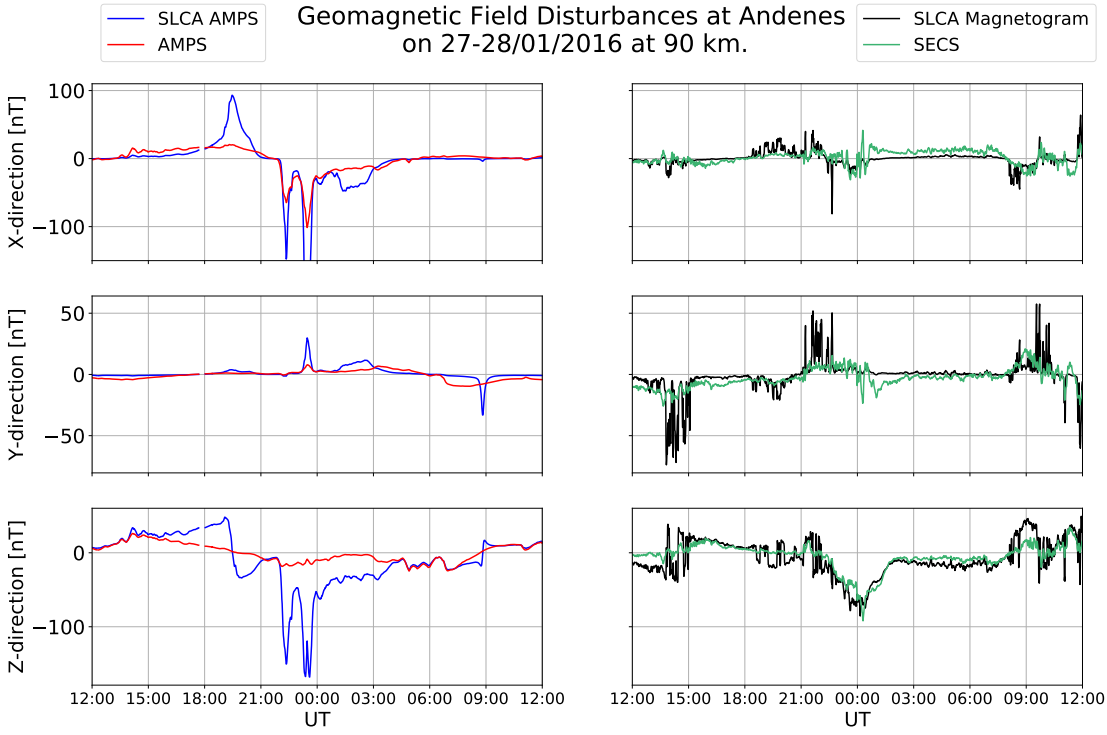

Fig. A.12.: Modelled magnetic field at 90 km altitude over Andenes on January 27-28 2016. The y-limits in this figure has been adjusted.

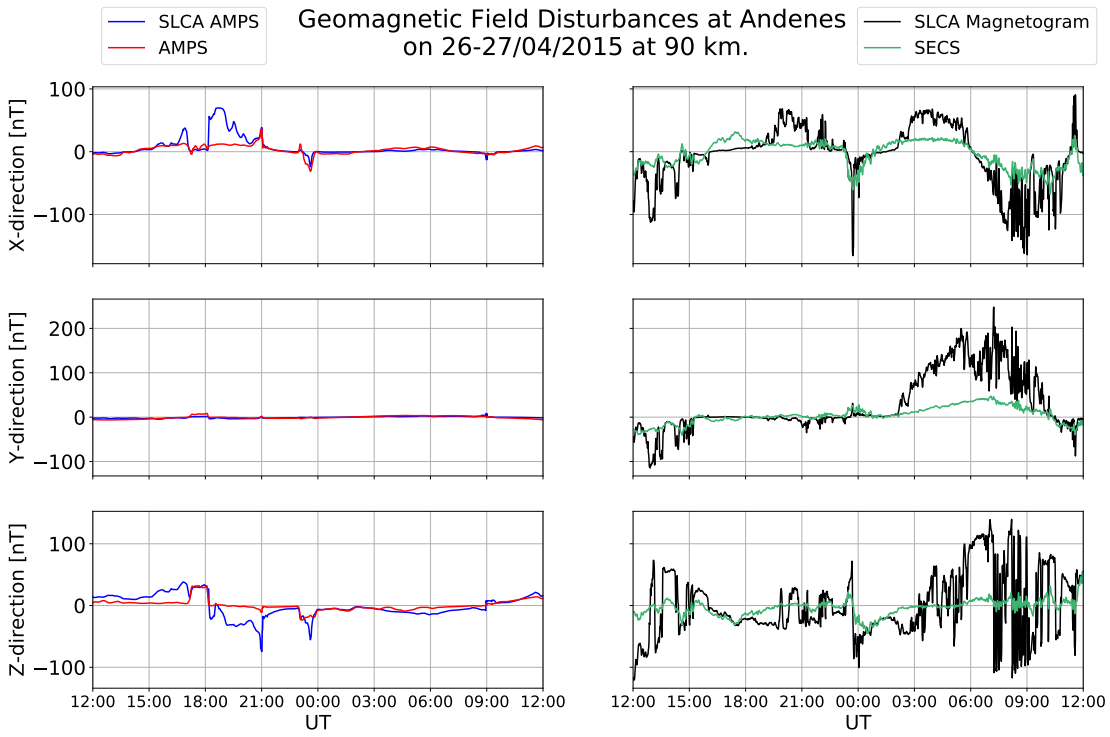

Fig. A.13.: Modelled magnetic field at 90 km altitude over Andenes on April 26-27 2015.

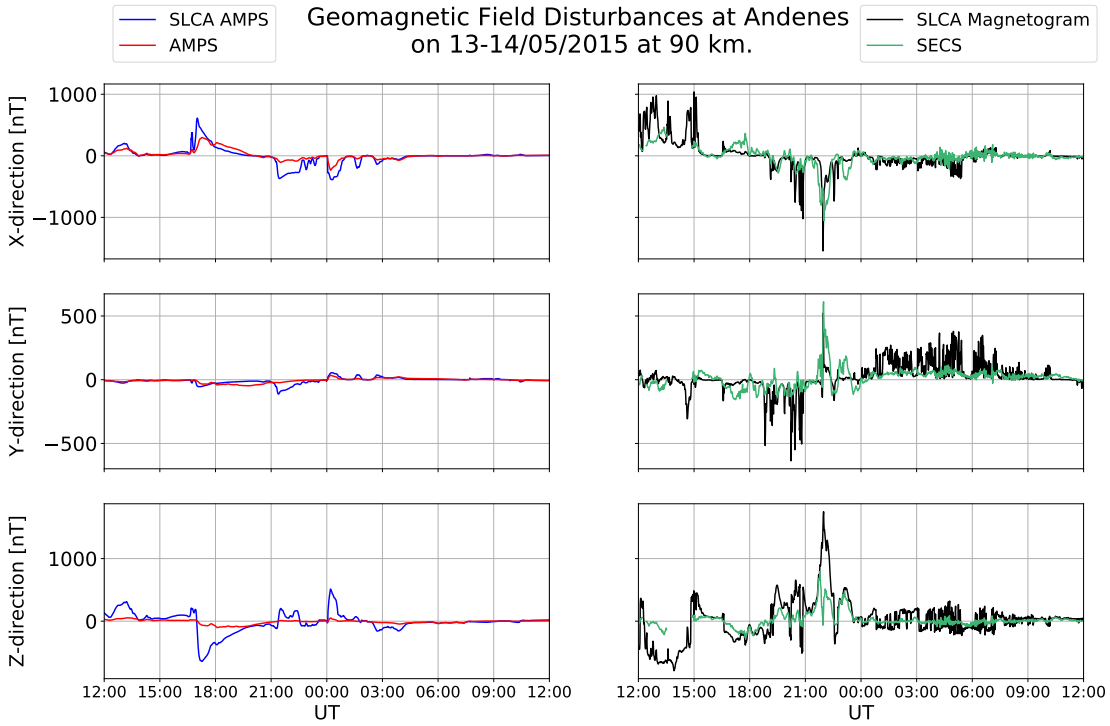

Fig. A.14.: Modelled magnetic field at 90 km altitude over Andenes on May 13-14 2015.

A.3 Results for 0 and 90 km

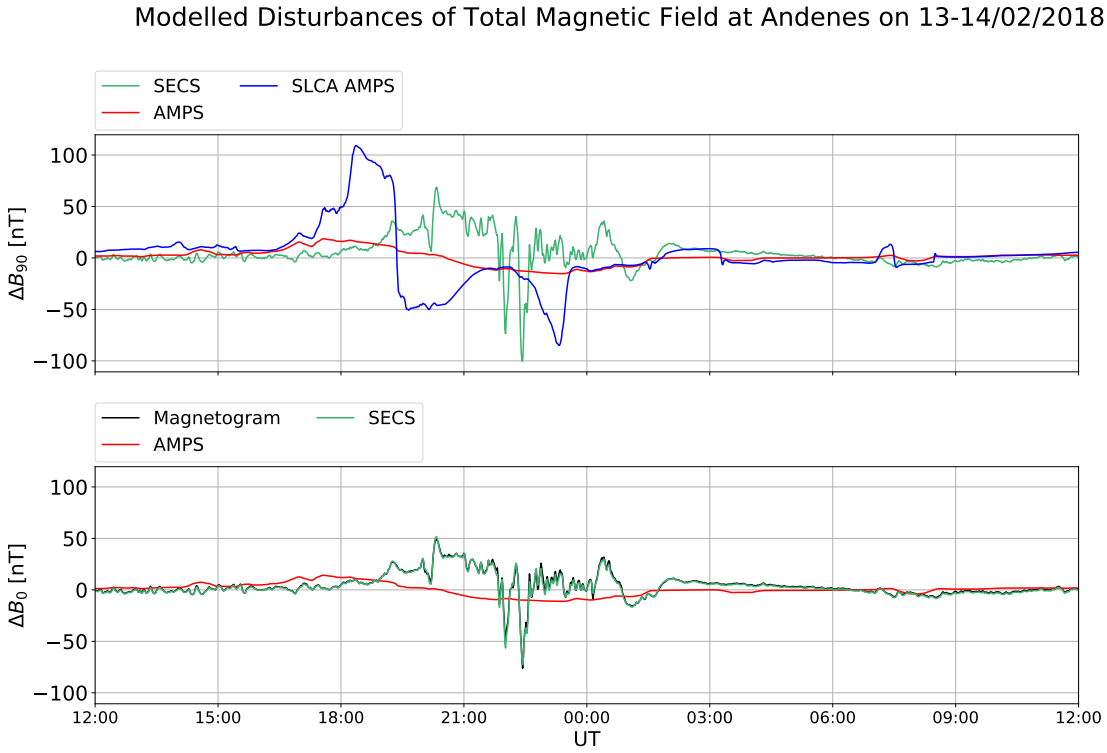

Fig. A.15.: Total magnetic field perturbations for 0 km and 90 km at Andenes on February 13-14 2018.

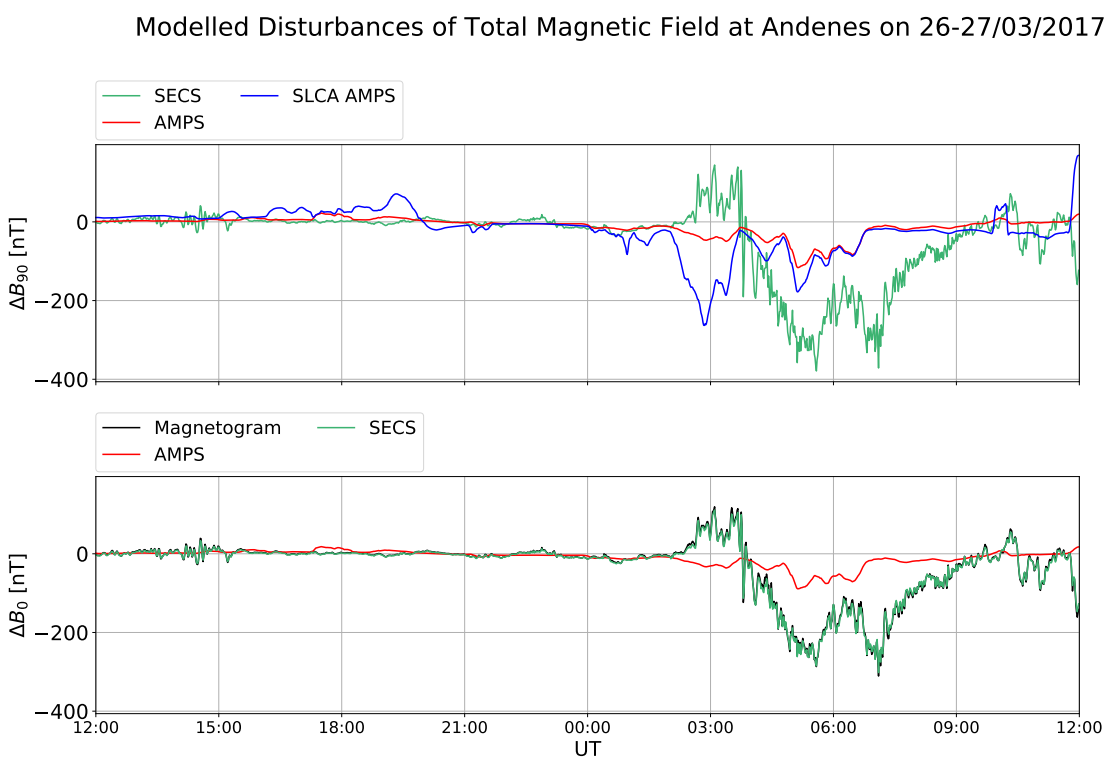

Fig. A.16.: Total magnetic field perturbations for 0 km and 90 km at Andenes on March 26-27 2017.

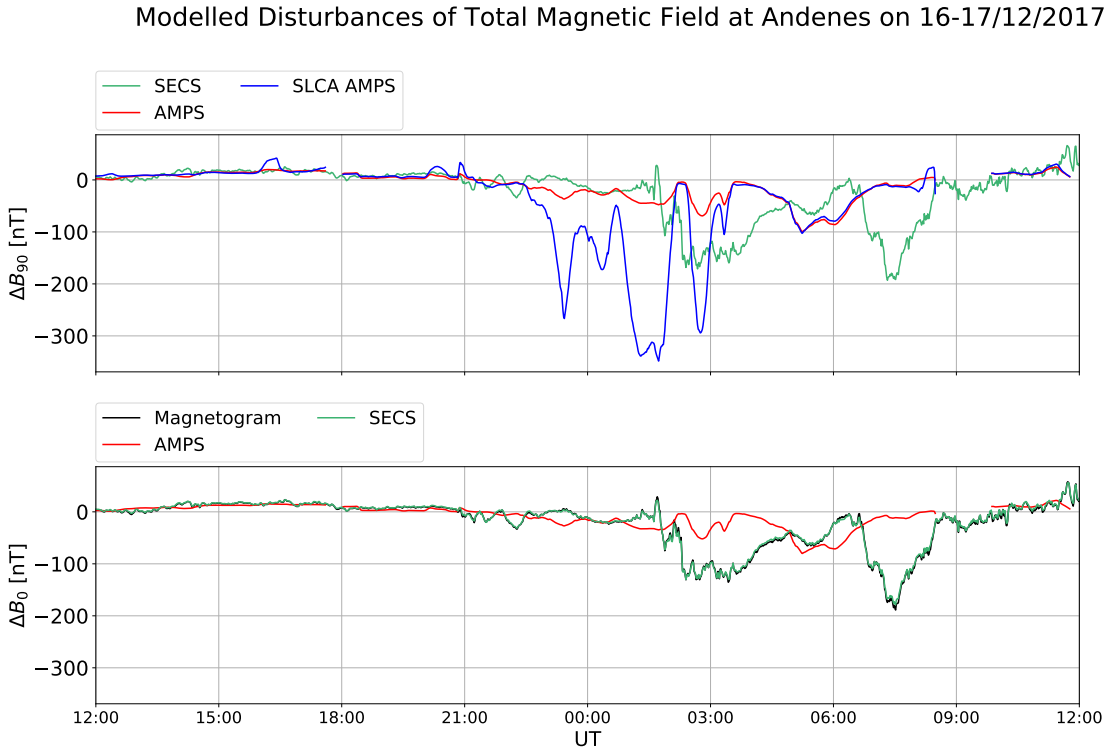

Fig. A.17.: Total magnetic field perturbations for 0 km and 90 km at Andenes on December 16-17 2017.

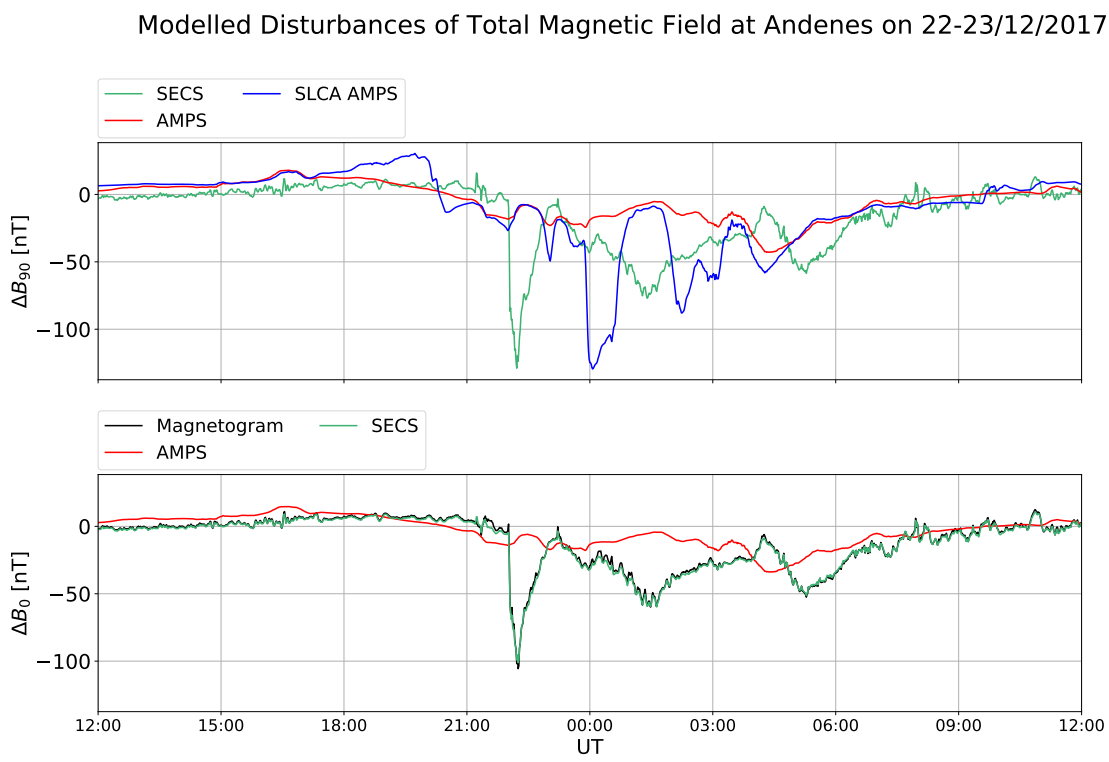

Fig. A.18.: Total magnetic field perturbations for 0 km and 90 km at Andenes December 22-23 2017.

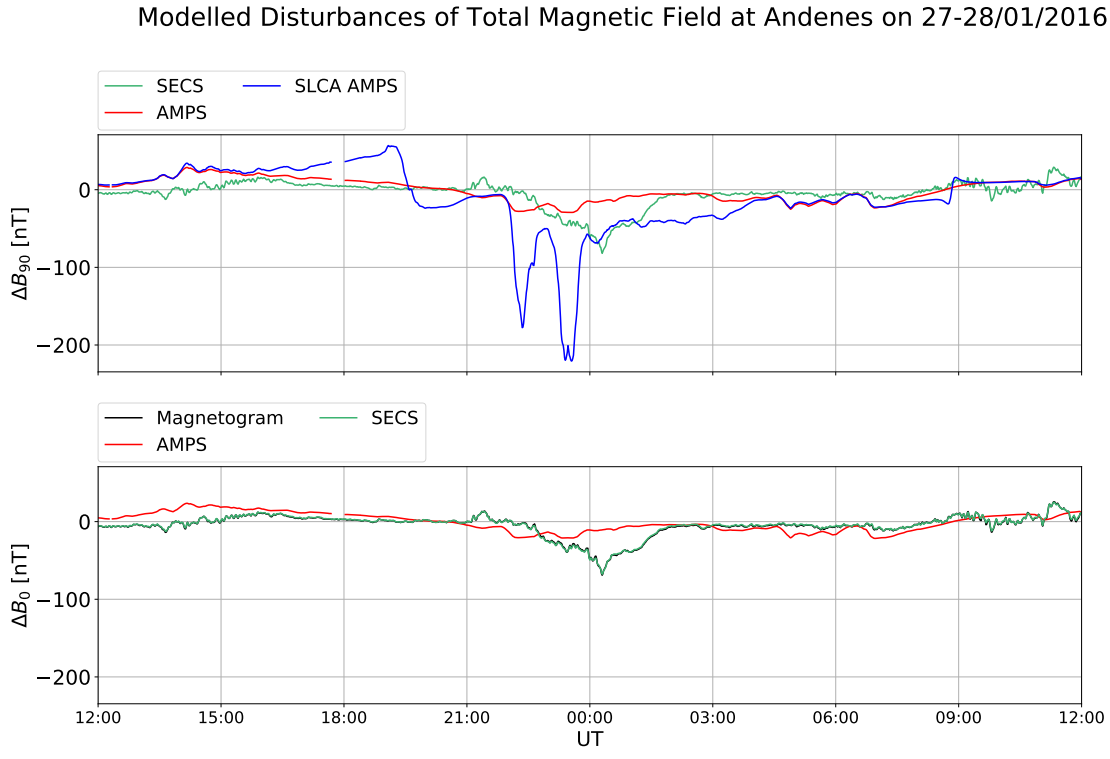

Fig. A.19.: Total magnetic field perturbations for 0 km and 90 km at Andenes on January 27-28 2016.

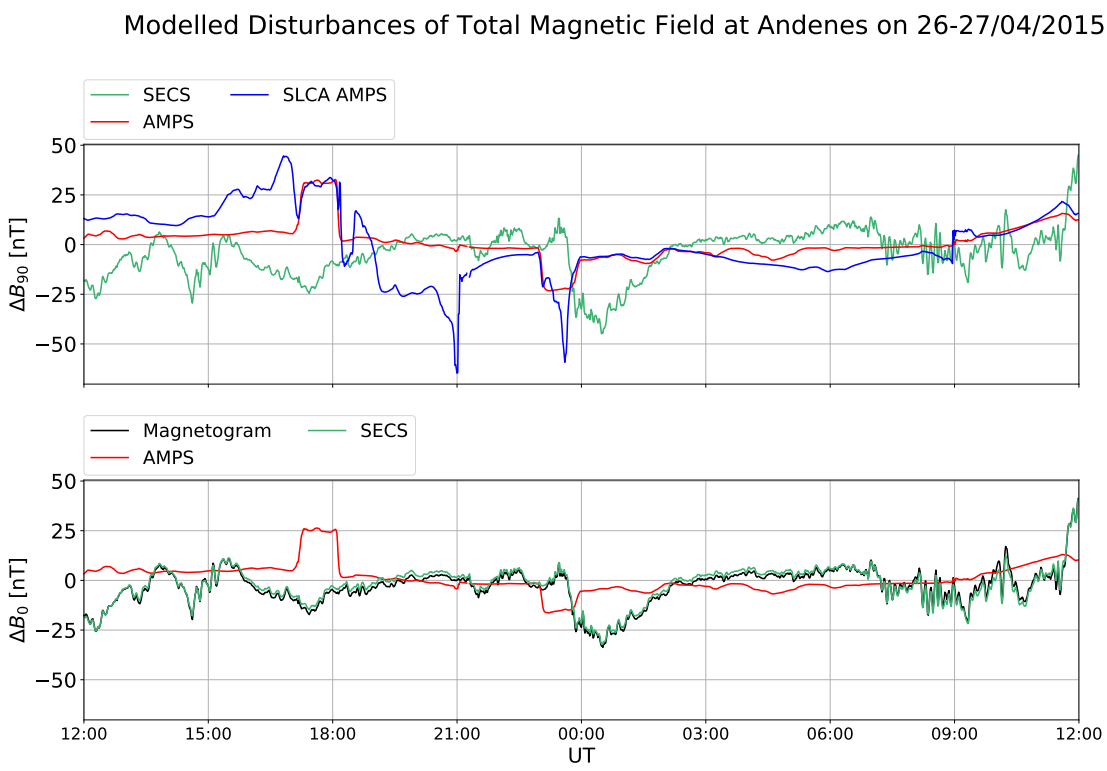

Fig. A.20.: Total magnetic field perturbations for 0 km and 90 km at Andenes on April 26-27 2015.

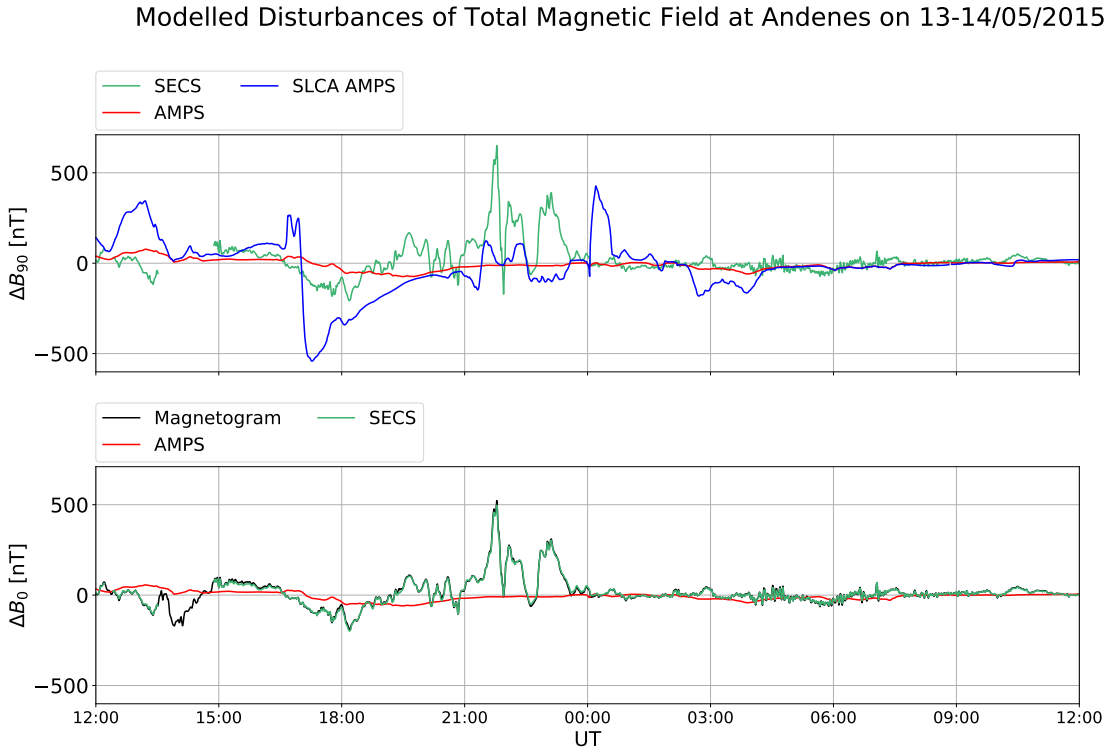

Fig. A.21.: Total magnetic field perturbations for 0 km and 90 km at Andenes on May 13-14 2015.

A.4 Results for Varying Altitudes

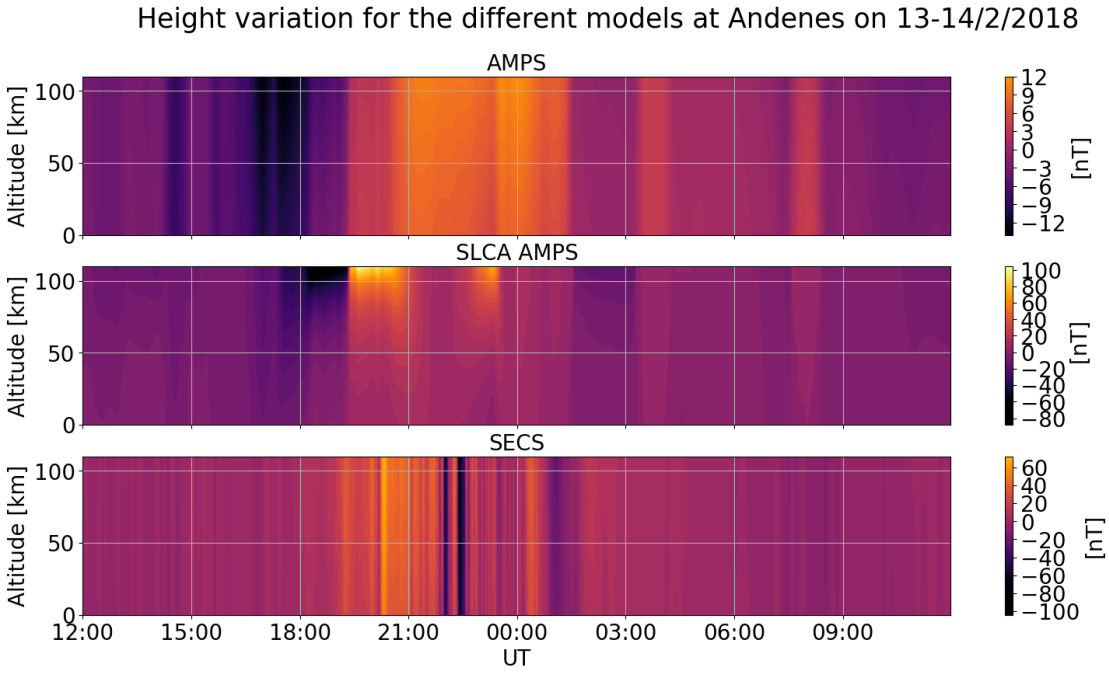

Fig. A.22.: Altitude variation in total magnetic field perturbations from 0 to 90 km using AMPS, SLCA and SECS outputs over Andenes on 13-14 February 2018.

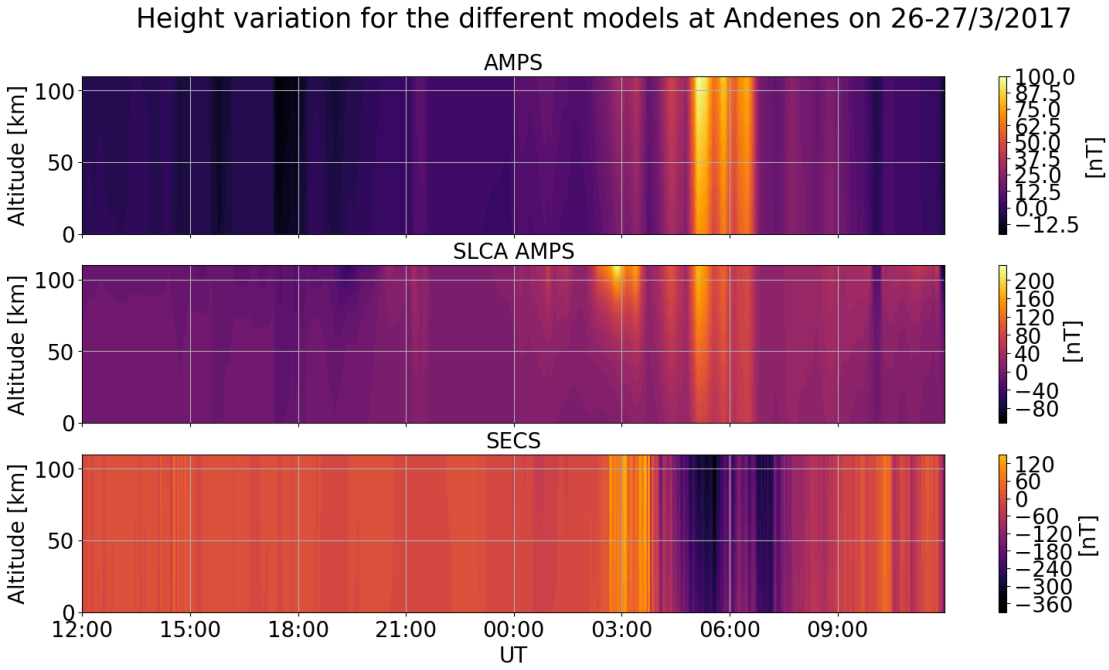

Fig. A.23.: Altitude variation in total magnetic field perturbations from 0 to 90 km using AMPS, SLCA and SECS outputs over Andenes on 26-27 March 2017.

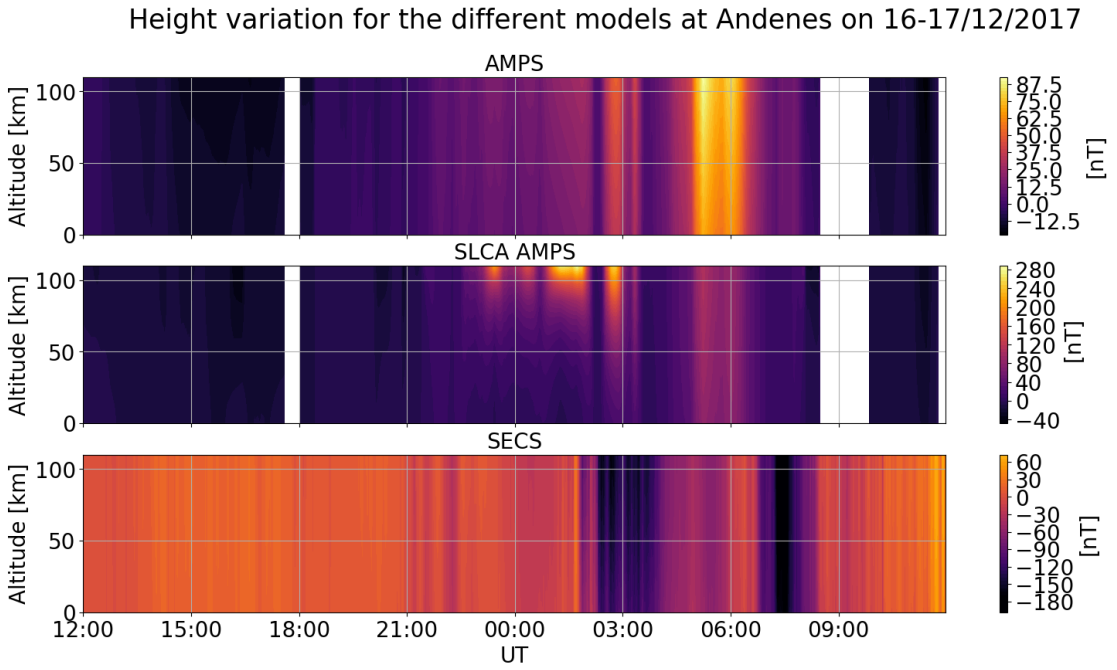

Fig. A.24.: Altitude variation in total magnetic field perturbations from 0 to 90 km using AMPS, SLCA and SECS outputs over Andenes on 16-17 December 2017.

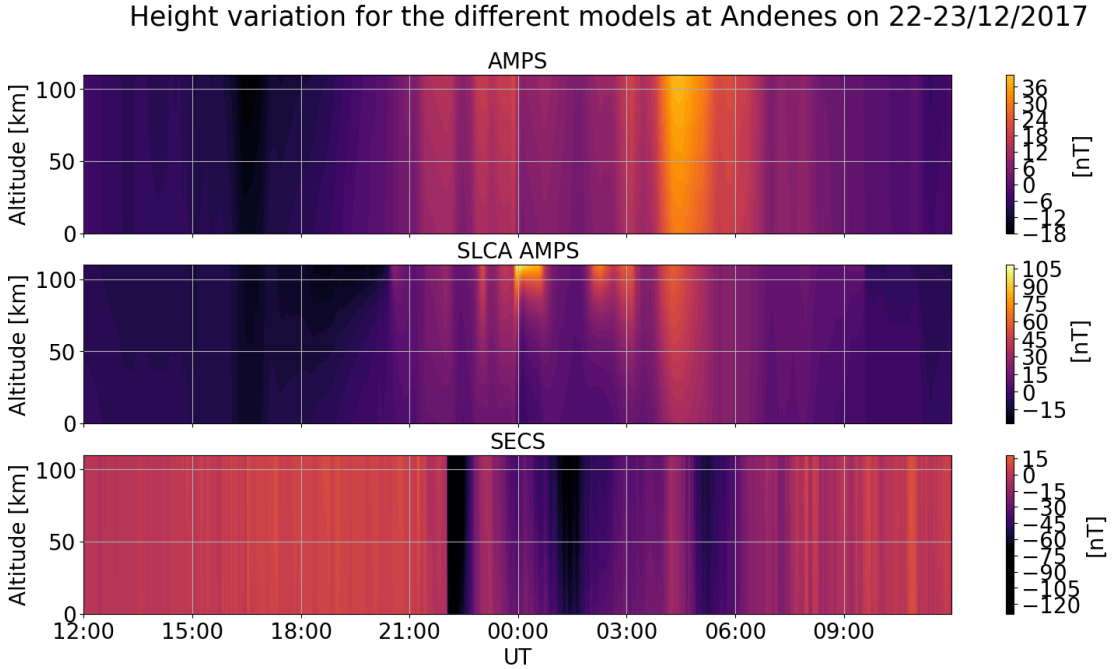

Fig. A.25.: Altitude variation in total magnetic field perturbations from 0 to 90 km using AMPS, SLCA and SECS outputs over Andenes on 22-23 December 2017.

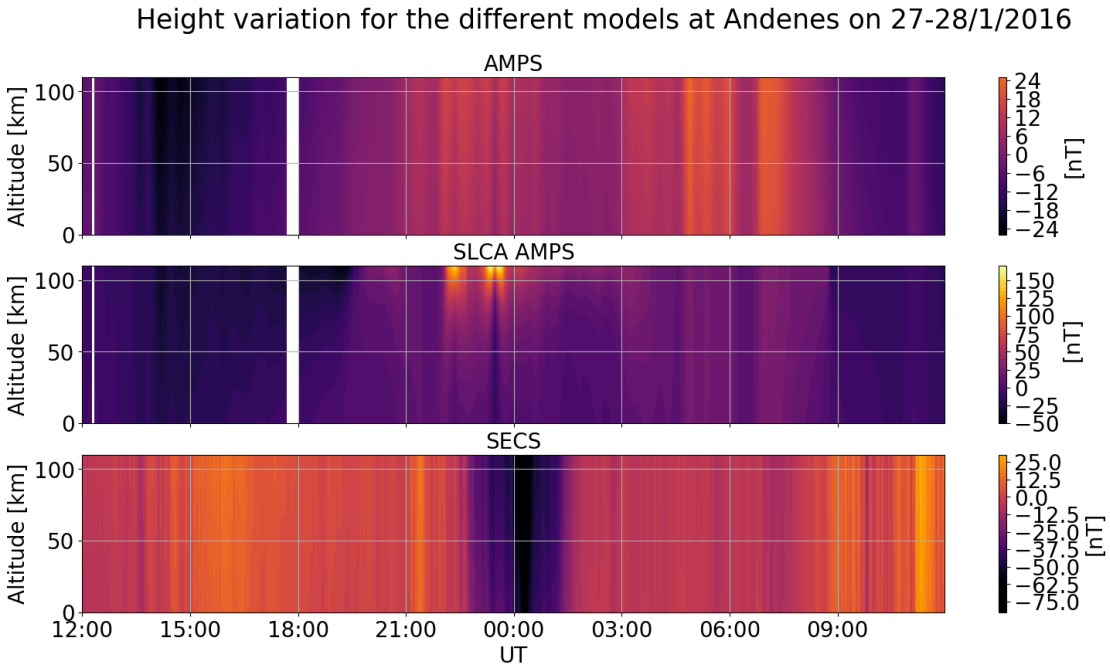

Fig. A.26.: Altitude variation in total magnetic field perturbations from 0 to 90 km using AMPS, SLCA and SECS outputs over Andenes on 27-28 January 2016.

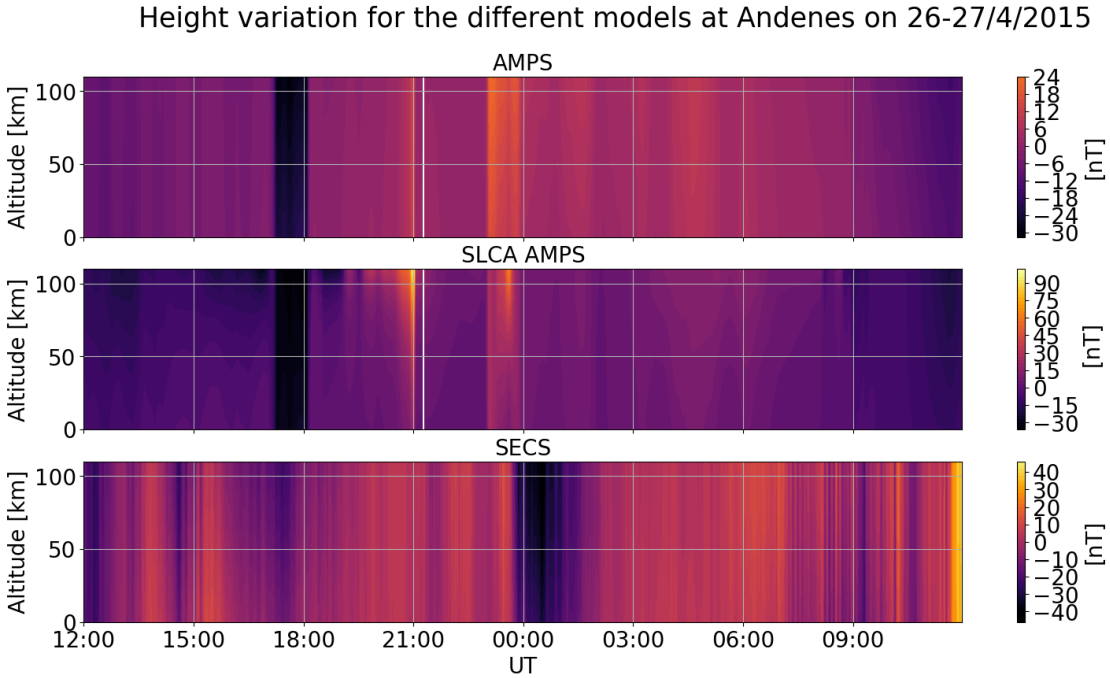

Fig. A.27.: Altitude variation in total magnetic field perturbations from 0 to 90 km using AMPS, SLCA and SECS outputs over Andenes on 26-27 April 2015.

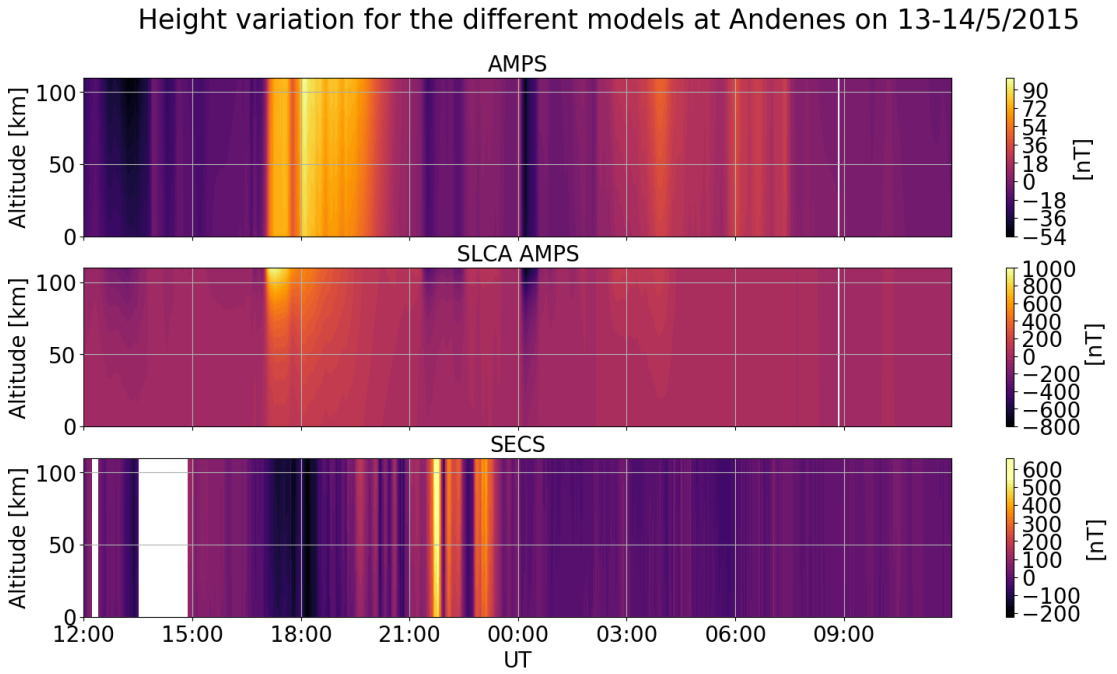

Fig. A.28.: Altitude variation in total magnetic field perturbations from 0 to 90 km using AMPS, SLCA and SECS outputs over Andenes on 13-14 May 2015.

AMPS Model Input

B

The input variables for the AMPS model are presented in this appendix.

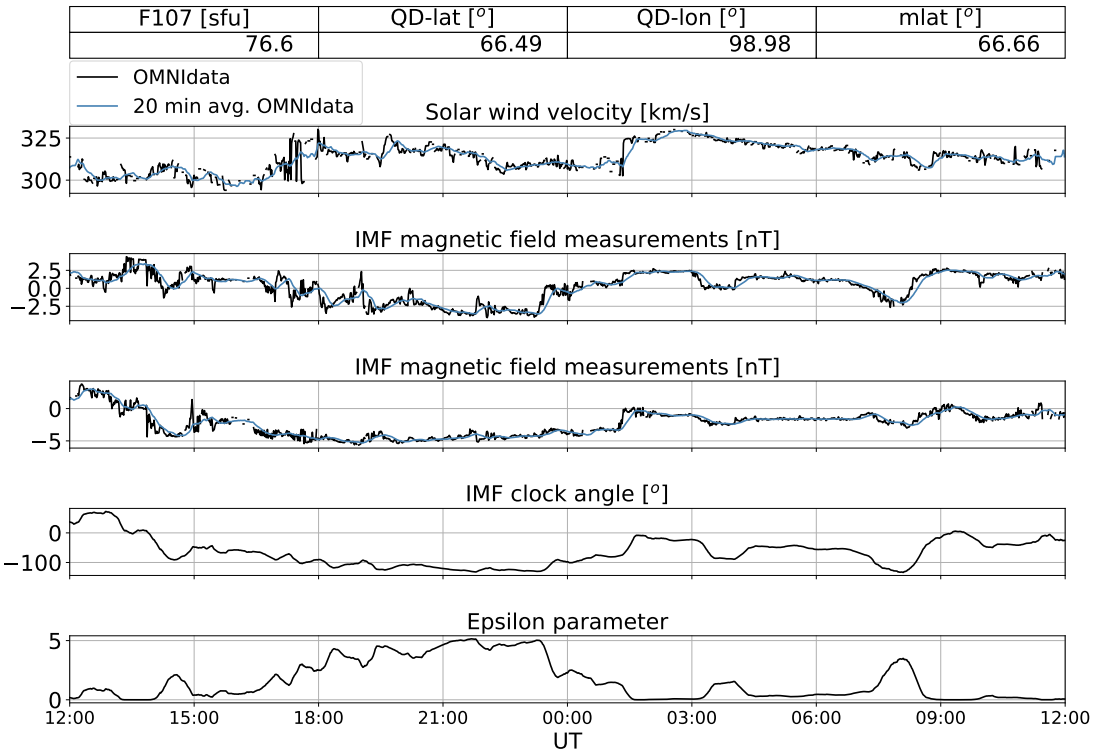

Fig. B.1.: AMPS input data on 13-14 February 2018

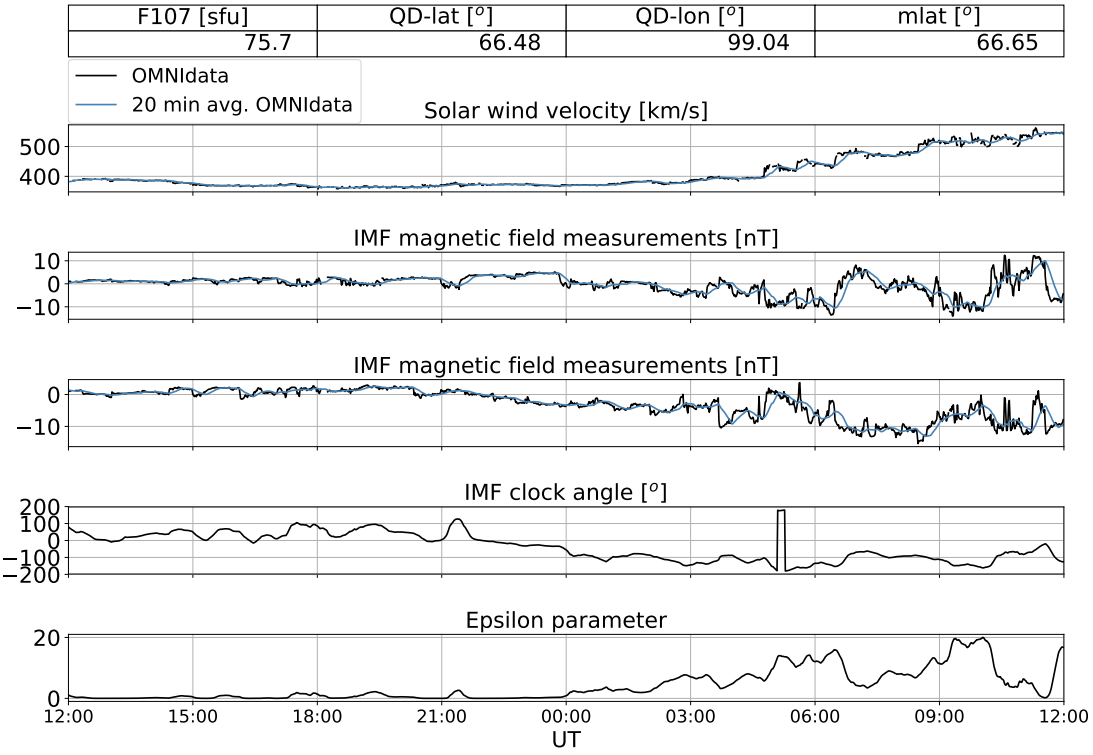

Fig. B.2.: AMPS input data on 26-27 March 2017

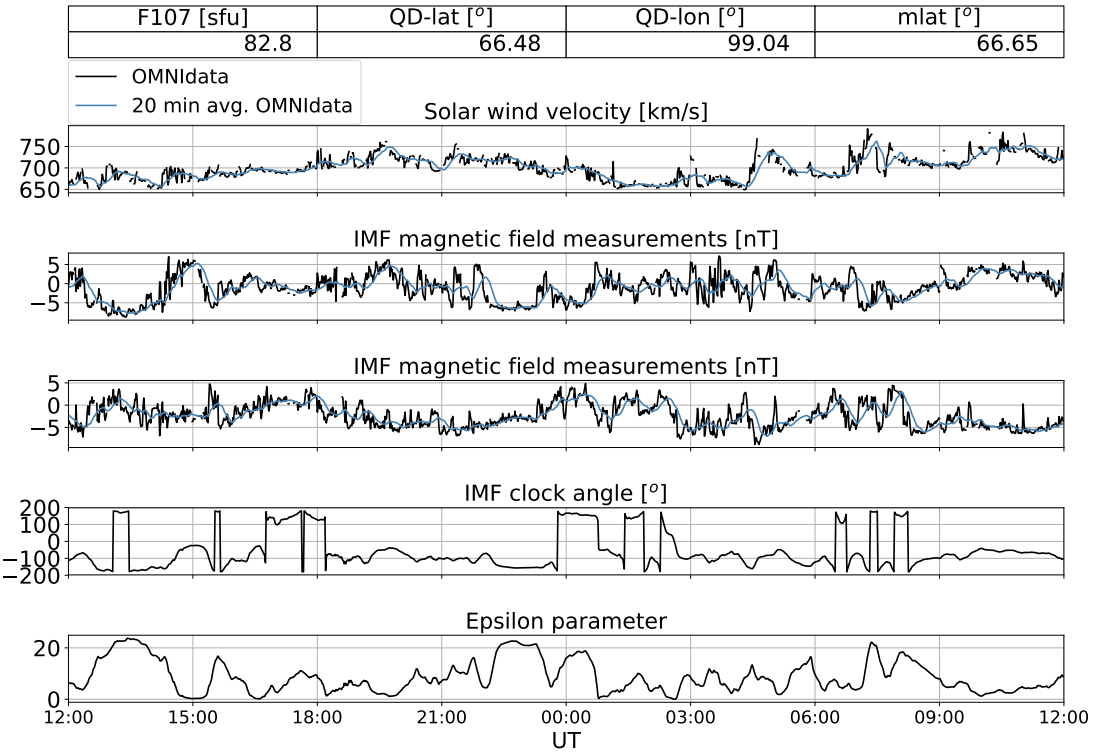

Fig. B.3.: AMPS input data on 22-23 April 2017

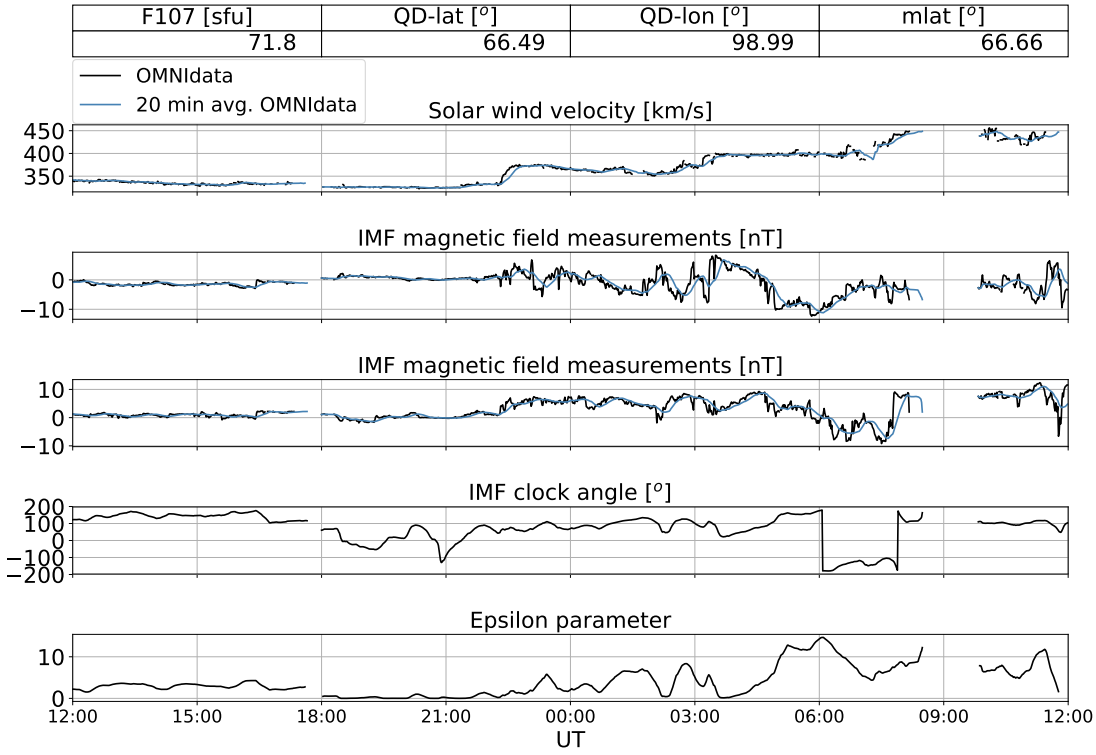

Fig. B.4.: AMPS input data on 16-17 December 2017

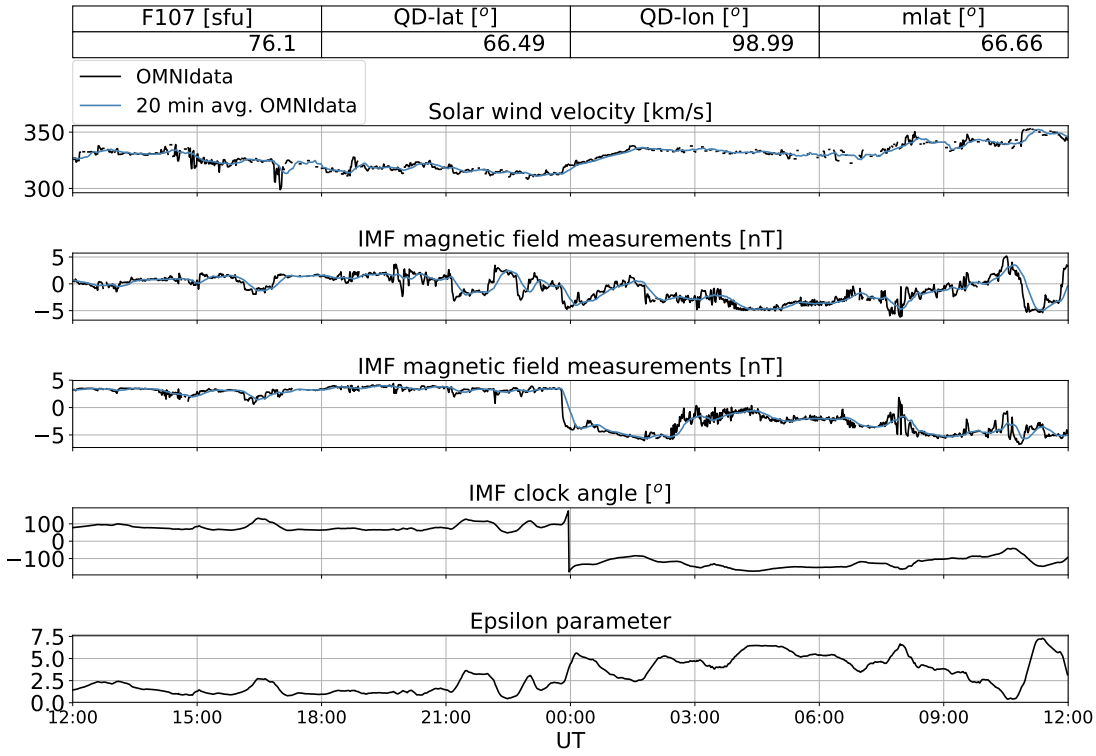

Fig. B.5.: AMPS input data on 22-23 December 2017

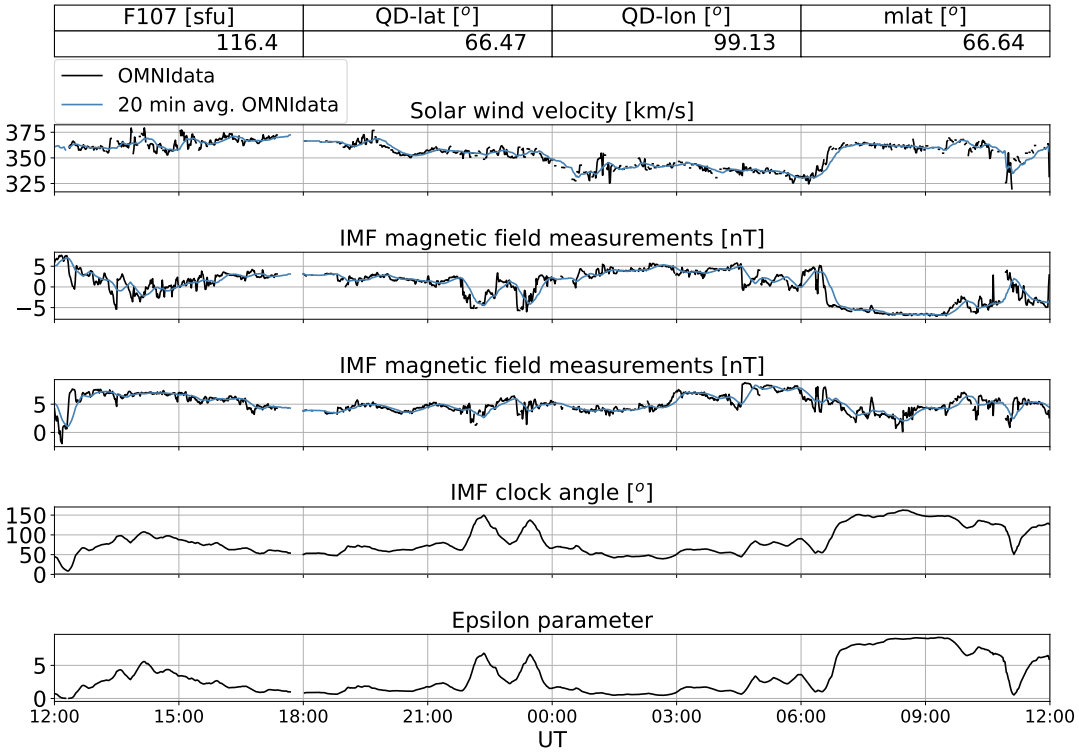

Fig. B.6.: AMPS input data on 27-28 January 2016

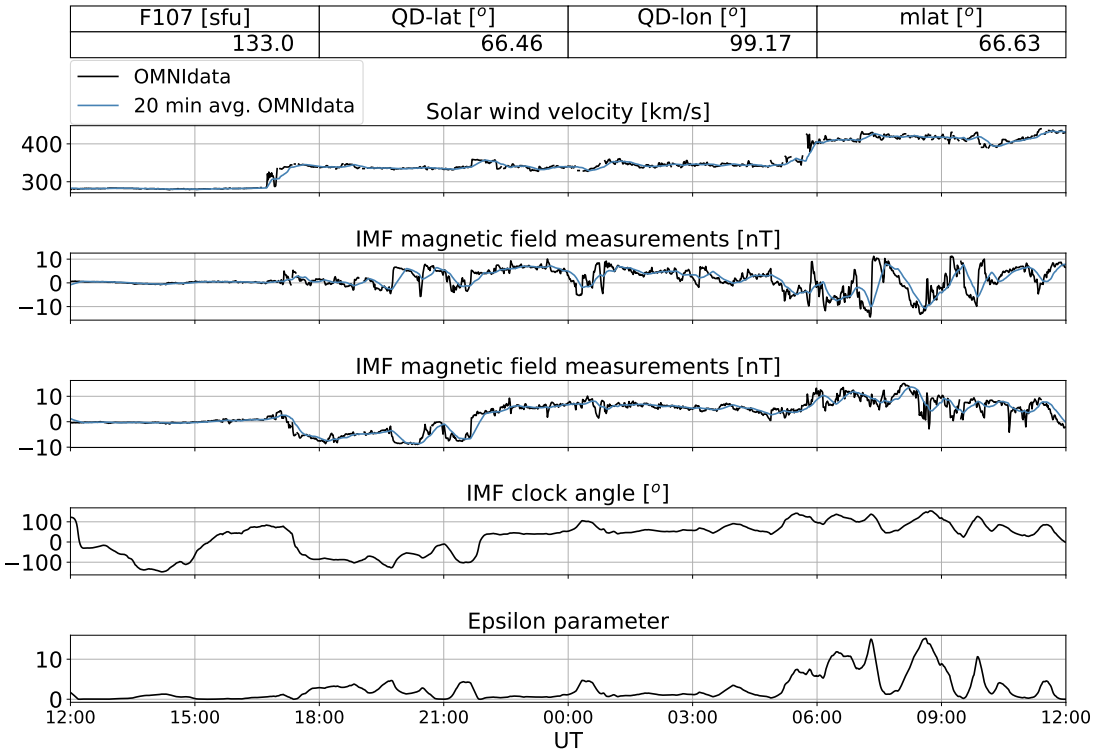

Fig. B.7.: AMPS input data on 21-22 June 2015

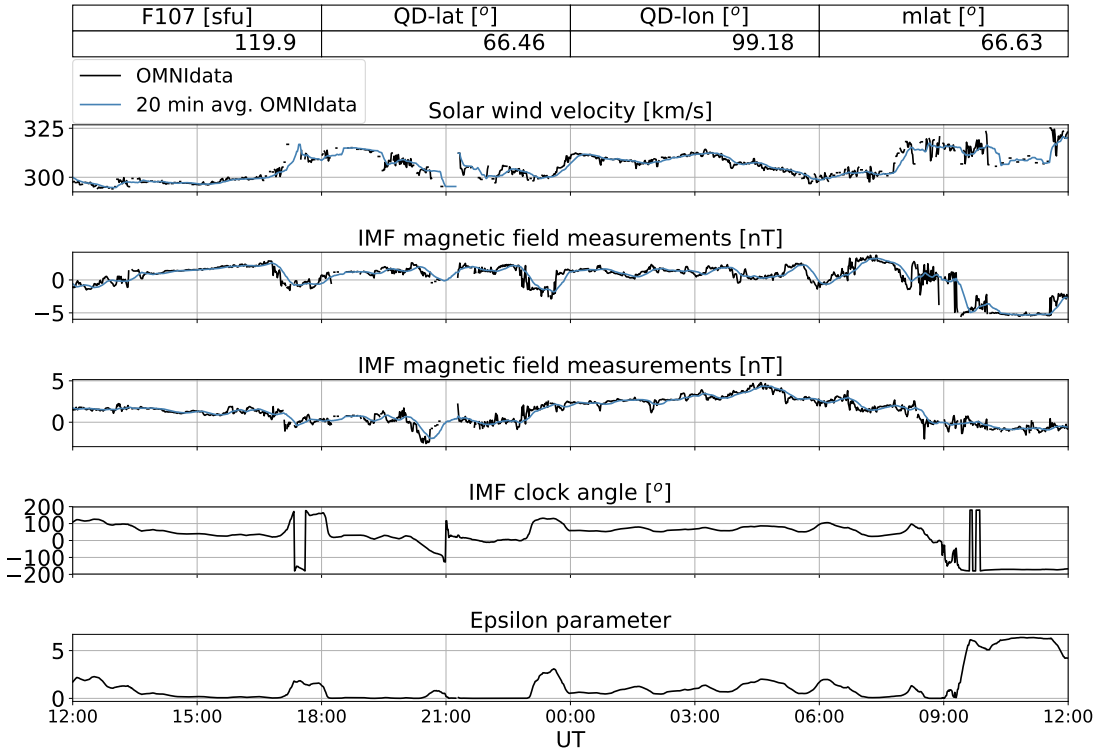

Fig. B.8.: AMPS input data on 26-27 April 2015

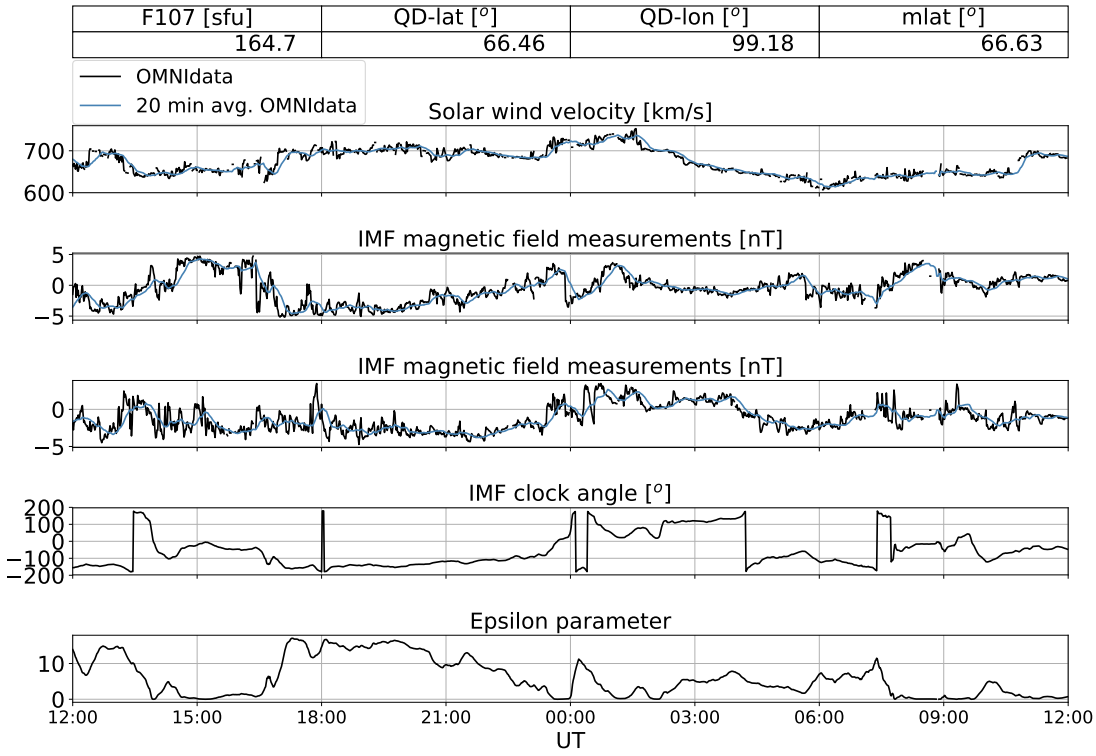

Fig. B.9.: AMPS input data on 13-14 May 2015

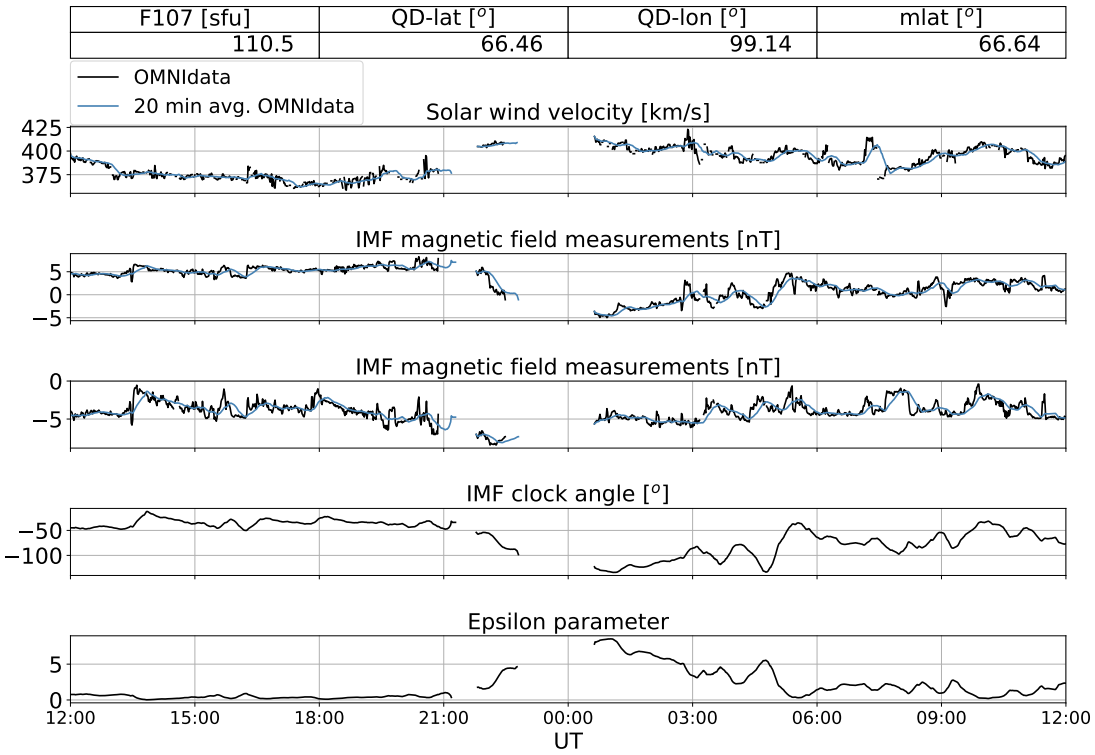

Fig. B.10.: AMPS input data on 20-21 November 2015

Rocket Bibliography

C

Presented in this section is an attempted, complete list of literature related to all the magnetic field measurements in the lower ionosphere taken by rocket magnetometers. During the work on this list it was the rocket data itself that was of interest, and thus this list has been limited to one study per rocket data, even if there were other papers discussing results from the same rocket.

Burrows, K and SH Hall (1965). „Rocket measurements of the geomagnetic field above Woomera, South Australia“. In: *Journal of Geophysical Research* 70.9, pp. 2149–2158.

Burrows, K and TSG Sastry (1976). „Rocket measurements of current distribution in a normal and an intense equatorial electrojet“. In: *Journal of Atmospheric and Terrestrial Physics* 38.3, pp. 307–311.

Burrows, K, JD Stolarik, and JP Heppner (1971). „Rocket measurements of the magnetic fields associated with visual aurorae“. In: *Planetary and Space Science* 19.8, pp. 877–890.

Cahill, Laurence J (1959a). „Detection of an electrical current in the ionosphere above Greenland“. In: *Journal of Geophysical Research* 64.10, pp. 1377–1380.

– (1959b). „Investigation of the equatorial electrojet by rocket magnetometer“. In: *Journal of Geophysical Research* 64.5, pp. 489–503.

Cahill, Laurence J, RL Arnoldy, and William WL Taylor (1980). „Rocket observations at the northern edge of the eastward electrojet“. In: *Journal of Geophysical Research: Space Physics* 85.A7, pp. 3407–3413.

Cloutier, PA and RC Haymes (1968). „Vector measurement of the midlatitude Sq ionospheric current system“. In: *Journal of Geophysical Research* 73.5, pp. 1771–1787.

Davis, T Neil, John D Stolarik, and James P Heppner (1965). „Rocket measurements of Sq currents at midlatitude“. In: *Journal of Geophysical Research* 70.23, pp. 5883–5894.

Davis, T Neil, K Burrows, and John D Stolarik (1967). „A latitude survey of the equatorial electrojet with rocket-borne magnetometers“. In: *Journal of Geophysical research* 72.7, pp. 1845–1861.

Hutchinson, R and B Shuman (1961). „Rocket measurements of the magnetic field above New Mexico“. In: *Journal of Geophysical Research* 66.9, pp. 2687–2693.

Kaeppler, Stephen Roland (2013). „A rocket-borne investigation of auroral electrodynamics within the auroral-ionosphere“. PhD thesis. University of Iowa.

Maple, E, WA Bowen, and SF Singer (1950). „Measurement of the Earth's magnetic field at high altitudes at White Sands, New Mexico“. In: *Journal of Geophysical Research* 55.2, pp. 115–126.

Maynard, NC and Laurence James Cahill (1965). „Measurement of the equatorial electrojet over India“. In: *Journal of Geophysical Research* 70.23, pp. 5923–5936.

Maynard, Nelson C (1967). „Measurements of ionospheric currents off the coast of Peru“. In: *Journal of Geophysical Research* 72.7, pp. 1863–1875.

Meredith, LH, LR Davis, JP Heppner, and OE Berg (1961). „Rocket auroral investigations“. In: *Ann. Intern. Geophys. Yr.* 12.Pt 2.

Park, RJ and Po A Cloutier (1971). „Rocket-based measurement of Birkeland currents related to an auroral arc and electrojet“. In: *Journal of Geophysical Research* 76.31, pp. 7714–7733.

Potter, Wentworth E (1970). „Rocket measurements of auroral electric and magnetic fields“. In: *Journal of Geophysical Research* 75.28, pp. 5415–5431.

Sesiano, J and PA Cloutier (1976). „Measurements of field-aligned currents in a multiple auroral arc system“. In: *Journal of Geophysical Research* 81.1, pp. 116–122.

Singer, S Fred, E Maple, and WA Bowen Jr (1951). „Evidence for ionosphere currents from rocket experiments near the geomagnetic equator“. In: *Journal of Geophysical Research* 56.2, pp. 265–281.

References

Akasofu, S-I (2013). „The relationship between the magnetosphere and magnetospheric/auroral substorms“. In: *Annales Geophysicae*. Vol. 31. 3. Copernicus GmbH, p. 387.

Amm, O and A Viljanen (1999). „Ionospheric disturbance magnetic field continuation from the ground to the ionosphere using spherical elementary current systems“. In: *Earth, Planets and Space* 51.6, pp. 431–440.

Amm, Olaf (1997). „Ionospheric elementary current systems in spherical coordinates and their application“. In: *Journal of geomagnetism and geoelectricity* 49.7, pp. 947–955.

Aspaas, Per Pippin and Truls Lynne Hansen (2012). „The role of the Societas Meteorologica Palatina (1781–1792) in the history of auroral research“. In: *Acta Borealia* 29.2, pp. 157–176.

Baumjohann, Wolfgang (1982). „Ionospheric and field-aligned current systems in the auroral zone: A concise review“. In: *Advances in Space Research* 2.10, pp. 55–62.

Brekke, Asgeir (2012). *Physics of the upper polar atmosphere*. Springer Science & Business Media.

Bustos, Felipe Pedreros, Domenico Bonaccini Calia, Dmitry Budker, et al. (2018). „Remote sensing of geomagnetic fields and atomic collisions in the mesosphere“. In: *Nature communications* 9.1, p. 3981.

Celsius, A (1740). „Bemerkungen über der Magnetnadel: Stündliche Veränderungen in ihrer Abweichung“. In: *Svensk. Vet. Handl* 8.296.

Cowley, SWH (2000). „Magnetosphere-ionosphere interactions: A tutorial review“. In: *Magnetospheric Current Systems, Geophys. Monogr. Ser* 118, pp. 91–106.

Edvardsen, Inge, Truls L Hansen, Morten Gjertsen, Harry Wilson, et al. (2013). „Improving the accuracy of directional wellbore surveying in the Norwegian Sea“. In: *SPE Drilling & Completion* 28.02, pp. 158–167.

Eleman, Folke (1969). *The Aeromagnetic Survey of Denmark, Finland, Norway, Sweden 1965: Contribution to the World Magnetic Survey*. Svenska Reprod.

Friis-Christensen, Eigil, H Lühr, and Gauthier Hulot (2006). „Swarm: A constellation to study the Earth's magnetic field“. In: *Earth, planets and space* 58.4, pp. 351–358.

Fukushima, Naoshi (1971). „Electric current systems for polar substorms and their magnetic effect below and above the ionosphere“. In: *Radio Science* 6.2, pp. 269–275.

Gilbert, William (1958). *De magnete*. Courier Corporation.

Haines, GV (1985). „Spherical cap harmonic analysis“. In: *Journal of Geophysical Research: Solid Earth* 90.B3, pp. 2583–2591.

Haines, GV and JM Torta (1994). „Determination of equivalent current sources from spherical cap harmonic models of geomagnetic field variations“. In: *Geophysical Journal International* 118.3, pp. 499–514.

Hiorter, Olav Peter (1747). „Von der magnetnadel verschiedenen bewegungen“. In: *Svensk. Vet. Acad. Handl* 27.

Hrvoic, Ivan and Lawrence R Newitt (2011). „Instruments and methodologies for measurement of the Earth's magnetic field“. In: *Geomagnetic Observations and Models*. Springer, pp. 105–126.

International Monitor for Auroral Geomagnetic Effects (2019). *IMAGE stations*. Accessed on 2019-03-20. URL: `http://space.fmi.fi/image/www/index.php?page=maps`.

Kamide, Y and A Brekke (1975). „Auroral electrojet current density deduced from the Chatanika radar and from the Alaska meridian chain of magnetic observatories“. In: *Journal of Geophysical Research* 80.4, pp. 587–594.

Kane, Thomas J, Paul D Hillman, Craig A Denman, et al. (2018). „Laser remote magnetometry using mesospheric sodium“. In: *Journal of Geophysical Research: Space Physics* 123.8, pp. 6171–6188.

Laundal, Karl M, Christopher C Finlay, and Nils Olsen (2016). „Sunlight effects on the 3D polar current system determined from low Earth orbit measurements“. In: *Earth, Planets and Space* 68.1, p. 142.

Laundal, Karl Magnus and JW Gjerloev (2014). „What is the appropriate coordinate system for magnetometer data when analyzing ionospheric currents?“ In: *Journal of Geophysical Research: Space Physics* 119.10, pp. 8637–8647.

Laundal, Karl Magnus and Jone Peter Reistad (2018). *The average magnetic field and polar current system model (AMPS)-Description of Algorithm*. SWARM DISC: swarm Data, Innovation, and Science Cluster SW-DD-BCSS-GS-0001. University of Bergen.

Laundal, KM, CC Finlay, N Olsen, and JP Reistad (2018). „Solar wind and seasonal influence on ionospheric currents from Swarm and CHAMP measurements“. In: *Journal of Geophysical Research: Space Physics*.

Le, G, JA Slavin, and RJ Strangeway (2010). „Space Technology 5 observations of the imbalance of regions 1 and 2 field-aligned currents and its implication to the cross-polar cap Pedersen currents“. In: *Journal of Geophysical Research: Space Physics* 115.A7.

Lohmann, Kenneth J, Catherine MF Lohmann, and Nathan F Putman (2007). „Magnetic maps in animals: nature's GPS“. In: *Journal of Experimental Biology* 210.21, pp. 3697–3705.

Lytskjold, Bjørn E (1991). „Magnetic surveys in Svalbard 1985-1987“. In: Meddelelser nr. 114. Norsk Polarinstitutt.

Newell, PT, T Sotirelis, K Liou, C-I Meng, and FJ Rich (2007). „A nearly universal solar wind-magnetosphere coupling function inferred from 10 magnetospheric state variables“. In: *Journal of Geophysical Research: Space Physics* 112.A1.

Omniweb (2018). *OMNIWeb: High Resolution OMNI*. Accessed on 2018-12-11. URL: https://omniweb.gsfc.nasa.gov/form/omni_min.html.

Pirjola, Risto (2000). „Geomagnetically induced currents during magnetic storms“. In: *IEEE Transactions on Plasma Science* 28.6, pp. 1867–1873.

Pulkkinen, Antti, Olaf Amm, and Ari Viljanen (2003a). „Ionospheric equivalent current distributions determined with the method of spherical elementary current systems“. In: *Journal of Geophysical Research: Space Physics* 108.A2.

Pulkkinen, Antti, Olaf Amm, Ari Viljanen, BEAR Working Group, et al. (2003b). „Separation of the geomagnetic variation field on the ground into external and internal parts using the spherical elementary current system method“. In: *Earth, planets and space* 55.3, pp. 117–129.

Reigber, Ch, H Lühr, and P Schwintzer (2002). „CHAMP mission status“. In: *Advances in Space Research* 30.2, pp. 129–134.

Richmond, A (1995). „Ionospheric Electrodynamics Using Magnetic Apex Coordinates“. In: *Journal of geomagnetism and geoelectricity* 47.

Rikitake, T (1968). „Geomagnetism and earthquake prediction“. In: *Tectonophysics* 6.1, pp. 59–68.

Rostoker, G, SI Akasofu, W Baumjohann, Yohsuke Kamide, and RL McPherron (1988). „The roles of direct input of energy from the solar wind and unloading of stored magnetotail energy in driving magnetospheric substorms“. In: *Space science reviews* 46.1-2, pp. 93–111.

Russell, Christopher T, Janet G Luhmann, and Robert J Strangeway (2016). *Space Physics: An Introduction*. Cambridge University Press.

Sato, Mariko, Yohsuke Kamide, Asgeir Brekke, Satonori Nozawa, et al. (1994). „The altitude profile of ionospheric currents and conductivities deduced from EISCAT observations“. In:

Serrano, Alessandra (2017). „Laser diagnostics of the mesospheric magnetic field. Understanding remote laser magnetometry in northern Norway“. MA thesis. UiT Norges arktiske universitet.

Space Weather Canada (2018). *Daily flux values*. Accessed on 2018-12-11. URL: http://www.spaceweather.gc.ca/solarflux/sx-5-flux-en.php.

Tanskanen, EI, A Viljanen, TI Pulkkinen, et al. (2001). „At substorm onset, 40% of AL comes from underground“. In: *Journal of Geophysical Research: Space Physics* 106.A7, pp. 13119–13134.

Thébault, Erwan, Christopher C Finlay, Ciarán D Beggan, et al. (2015). „International geomagnetic reference field: the 12th generation“. In: *Earth, Planets and Space* 67.1, p. 79.

Tromsø Geophysical Observatory (2018). *Geomagnetic Data from TGO*. Accessed on 2018-12-11. URL: http://flux.phys.uit.no/geomag.html.

Weigel, RS, D Vassiliadis, and AJ Klimas (2002). „Coupling of the solar wind to temporal fluctuations in ground magnetic fields“. In: *Geophysical Research Letters* 29.19, pp. 21–1.

Weygand, James M, Olaf Amm, A Viljanen, et al. (2011). „Application and validation of the spherical elementary currents systems technique for deriving ionospheric equivalent currents with the North American and Greenland ground magnetometer arrays“. In: *Journal of Geophysical Research: Space Physics* 116.A3.

Colophon

This thesis was typeset with LaTeX 2_ε. It uses the *Clean Thesis* style developed by Ricardo Langner. The design of the *Clean Thesis* style is inspired by user guide documents from Apple Inc.

Download the *Clean Thesis* style at `http://cleanthesis.der-ric.de/`.